WAVES, TURBULENCE, AND CIRCULATION IN THE ALTAMAHA RIVER ESTUARY, GEORGIA

by

KI RYONG KANG

(Under the direction of Daniela Di Iorio)

ABSTRACT

Physical processes such as sea surface waves, turbulence, and residual circulation were studied in an estuarine environment using several observational data sets and modeling experiments in the Altamaha River Estuary, GA. The wave energy within the estuary becomes periodic in time showing wave energy during flood to high water phase of the tide and very little wave energy during ebb to low water. This periodic modulation is a direct result of enhanced depth and current-induced wave breaking that occurs at the ebb-shoaling region surrounding the Altamaha River mouth. Modeling results showed that depth-induced wave breaking is more important during the low water phase of the tide than current-induced wave breaking during the ebb phase of the tide. In this shallow environment these wave-current interactions lead to an increased bottom roughness, resulting in an enhanced bottom friction coefficient.

An increase of river discharge changed the estuarine turbulence flow and density characteristics into a more ebb-dominated and stratified system. The Reynolds stress and turbulent kinetic energy (TKE) were increased due to increased river discharge. The spectral energy density of turbulent flow was deformed by surface waves and better satisfied the -5/3 slope for isotropic trublence when the wave-induced motions were removed. Buoyancy flux increased in magnitude with increased longitudinal density gradient and showed a weak energy source during flood tide and a relatively strong energy sink during ebb. A balance between production and dissipation of energy was not obtained, implying that turbulent transport of TKE is a consideration. Numerical modeling results revealed a complex depth dependence on turbulence intensity that varied with the tidal cycle and with the level of stratification.

The mean flow is dominated by the semidiurnal lunar tidal component (M2) and the tidal phase showed fairly constant values in the center of the channel with strong variations in the shoaling regions. When the M2 component was removed, weak landward residual flows appeared on both slack waters, which may be a result of weak turbulent mixing and greater stratification, and strong seaward residual flow occurred during flood and ebb tides that may be attributed to strong turbulence levels.

Index words: estuary, surface waves, energy propagation, wave breaking, ebb shoaling, boundary layer, turbulence, turbulent kinetic energy, Reynolds stress, shear production, dissipation rate, buoyancy flux, tide, residual flow, semidiurnal component, volume transport, circulation, Altamaha River Estuary

Waves, Turbulence, and Circulation in the Altamaha River Estuary, Georgia

by

Ki Ryong Kang

M.Sc., Pusan National University, Korea, 1992

B.Sc., Pusan National University, Korea, 1989

A Dissertation Submitted to the Graduate Faculty

of The University of Georgia in Partial Fulfillment

of the

Requirements for the Degree

Doctor of Philosophy

Athens, Georgia

2005

© 2005
Ki Ryong Kang
All Rights Reserved

Waves, Turbulence, and Circulation in the Altamaha River Estuary, Georgia

by

Ki Ryong Kang

Approved:

Major Professor: Daniela Di Iorio

Committee: Merryl Alber
David E. Stooksbury
Jackson O. Blanton
Adrian Burd

Electronic Version Approved:

Maureen Grasso
Dean of the Graduate School
The University of Georgia
August 2005

Dedication

To my son Charles Minsauk Kang and daughter Elena Saujin Kang and wife NamHi Cho.

To my parents Pan-Hee Kang, Duck-Im Joo and parents-in-law Moon-Gu Cho and Mal-yo Choi.

ACKNOWLEDGMENTS

First, I would like to thank my advisor Dr. Daniela Di Iorio who has been and continues to be an excellent mentor, teacher and colleague. Without her guidance and encouragement it would not have been possible for me to complete my Ph.D. degree. And thanks to her husband Donald Newman for always welcoming our family, and sons Evan and Marco for playing with my son. I thank Dr. Jackson O. Blanton for his constructive comments, and giving the thesis a greater depth in physical oceanography. I would like to thank Dr. Merryl Alber for helping me gain a wider view of estuarine studies from an ecological perspective and for her very helpful critique of the thesis. I also thank Dr. David Stooksbury for helpful comments and advice since the coastal meteorology class in 2000. I thank Dr. Adrian Burd for showing me that turbulence is a very important factor in the plankton world and giving me comments related to that subject. I also thank him for very constructive criticisms on the presentation of results in the thesis. I would like to thank Dr. Tim Hollibaugh for including me in the diverse and multi-disciplinary Georgia Coastal Ecosystems Long Term Ecological Research (GCE-LTER) project supported by NSF (OCE9982133). Support to my advisor was also provided by the University of Georgia Research Foundation, Faculty Research Grant program which allowed us to upgrade instruments and develop bottom mount frames.

Special thanks have to go to Dr. Mary Ann Moran for her support in our graduate school life. I also thank Dr. SangRyong Lee in Korea for advice about the tidal current data processing and helping me to understand estuarine physics. I thank Dr. Jane M. Smith in the U.S. Army Engineer Research and Development Center for providing the source code of the STWAVE and giving me a lot of help in running the wave model. I thank also Dr. Hans Burchard for his help in running the turbulence model (GOTM). Thanks are due to Ed Sheppard and Matthew Erickson for helping me during the LTER cruise periods and travel between Athens and Savannah. I thank Julie Amft, as a physical oceanographer, for helping me with CTD data collection and numerous explanations for its processing. I thank the crew of the R/V Bluefin and Savannah (Captain Raymond Sweatte, Michael Richter, Raymond Thomas, Todd Recicar, Bryan Lincoln) for their help in deploying and recovering all the oceanographic instrumentation during many LTER research cruises, and also giving me the chance to learn seamanship including tieing knots and fishing techniques.

I am grateful to my friend and colleague Alan Barton and his friend Christine Smith, for their help in the lab especially when I started using the acoustic instruments. Thank you to Dai Mar Tamarack who showed a lot interest in oriental culture, and for making it fun in the lab. I thank Paul Mckay, Katherine Doyle and Lisa Pfau for numerous conversations in the lab. I also thank Erin Biers for her help in completing the required shore-based field experience and for her editorial comments of the Introduction. Thanks JinMu Choi, Changjin Lee and YoonHo Jin for your company when we played tennis and talking at five-points. Thanks Clayton Louden, who works at Jittery Joe's coffee shop, and many others there for their happy greetings and conversations.

Invaluable encouragement from my parents, parents-in-law and my brothers and sisters made me stronger as they supported my time here and time away from family in Korea. Finally, I must say thank you to my beautiful wife (NamHi), my brave son (Minsauk) and angelic daughter (Saujin) for their daily support, encouragement, and endurance in this long and sometimes lonely journey.

Table of Contents

List of Figures

List of Tables

Chapter 1

INTRODUCTION AND LITERATURE REVIEW

1.1 Background

All physical, biological and chemical phenomena in estuaries are the result of complex processes occurring simultaneously and changing continuously with time. The estuary itself, located where a river meets the sea, is a zone where freshwater is mixed with oceanic water. This could also include bays, gulfs and inlets as long as seawater is diluted with freshwater from land runoff (Dyer, 1997; Pritchard, 1967). The major physical components affecting estuaries are tidal forcing, bottom friction, wind, buoyancy input levels, and waves. These processes result in water mass mixing, sediment erosion and deposition, material transport, and pollutant dispersion. When hydrodynamic changes take place that are relatively faster than biological and geochemical changes, the physical factors become the dominant controlling processes in estuaries (Officer, 1980).

Surface waves, which are the up and down movements of the sea surface, superficially look like a very simple fluid motion; however, considering their impact on coastal and offshore structures, bottom sediment transport, estuarine circulation and momentum exchange between the atmosphere and ocean, they are important enough to be qualified as a controlling mechanism for estuarine systems. The waves generated offshore by winds propagate to the coastal environment where they are more strongly affected by bottom topography, currents and sea level changes.

Many researchers have studied several kinds of effects caused by surface waves in shallow water environments. Bender and Wong (1993) showed that wave-current interactions (wave and tidally driven flow) play a role in the bottom friction change and in the volume flux decrease of the bottom boundary layer. Gonzalez (1984) described how currents change the wave height distribution at the Columbia River entrance, showing that wave heights decrease during flood (following current) and increase dramatically during the ebb tide (opposing current). According to this explanation, an opposing current retards the advance of a wave and a following current enhances the advance of the wave.

Wave breaking, which happens as waves approach shallow water and increase in steepness, is an interesting process of energy transformation. When waves break, the momentum of the wave motion is transferred to the water column, which has implications for longshore currents at the coastal boundary, sediment transport processes and turbulent energy dissipation (Seymour, 1989; Horikawa, 1978). Many people have studied the mechanism of wave breaking through observations (Suhayda and Pettigrew, 1977; Battjes and Janssen, 1978; Thornton, 1979; Guza and Thornton, 1980; Thornton and Guza, 1982, 1983; Hir et al., 2000) and have identified bathymetric features, ebb shoaling and currents, as the primary mechanism for breaking events. Where the area is shallow, less than 10 meters, and has a dominant tidal flow, such as the sites extending this study, wave energy can be deformed by both the currents and bottom topography as waves propagate inshore from the continental shelf to the estuary.

The wave bottom boundary layer is a result of interactions between the wave orbital motions and the seafloor. It affects wave energetics because of high dissipation rates, and also affects sediment erosion and deposition (Trowbridge and Madsen, 1984a,b; Mathisen and Madsen, 1996a,b; Styles and Glenn, 2002b). Wave energy is attenuated with depth, and the energy dissipation rate is maximum close to the bottom. The dissipation rate is a function of wave height, frequency spectra, local water depth, bottom roughness (including sand ripples) and mean current conditions (Grant and Madsen, 1979). Small-scale flow variations, including turbulence developed within the current boundary layer near the seabed, can also be influenced by surface waves. Understanding the interaction between waves and the seafloor is critical for explaining beach erosion, bottom morphology, surface wave energy budgets and bottom friction experienced by mean currents.

Turbulence, which is irregular, random, highly dissipative, continuous, and three-dimensional, is necessary for mixing mass, momentum, salt, heat and other water properties, particularly in the coastal or estuarine environment (Tennekes and Lumley, 1999; Salmon, 1998). Turbulence affects gas flux across the air-sea interface, and transmission of heat in and out of the ocean reservoir, thus governing climate. However, it has been difficult to directly measure the three-dimensional properties of turbulent flow in the field because its length scales range from the dissipative microscale to the energy containing scales of a few meters all intermittent with time. Some of the first measurements of oceanic turbulence were conducted in the late 1950s using hot-film anemometers and other sensors towed in coastal tidal channels (Grant et al., 1962; Lueck et al., 2002). By the late 1960s vertical free-fall profilers were developed and numerous studies of turbulence in estuaries and coastal seas have been carried out since then (Peters, 1997, 1999; Peters and Bokhorst, 2000, 2001; Simpson et al., 2002; Moum et al., 2002). Researchers have tried to observe turbulence-related parameters such as the turbulent kinetic energy (TKE), Reynolds stress, and production and dissipation rates in estuarine and coastal environments. During the 1990s it became possible to measure these processes with newly developed high frequency acoustic processing and deployment techniques (see Lueck et al., 1997; Trowbridge et al., 1999; Lu and Lueck, 1999a,b; Rippeth et al., 2001; Stacey, 1999; Stacey et al., 1999; Shaw et al., 2001; Gargett, 1988, 1999).

Turbulent motion in shallow coastal environments is driven primarily by such factors as bed drag characteristics, velocity shear, density gradients and wave breaking. In shallow areas, as mentioned previously, the surface wave energy can reach the bottom creating a thin wave boundary layer ($<$ 30 cm) and can affect the current boundary layer which varies from 1-10 m in thickness by altering the friction velocity (Styles and Glenn, 2002a; Trowbridge and Madsen, 1984a,b). In fact it is hard to completely separate the turbulent and wave components from field data, because of the non-linearity of this flow interaction. If, however, we assume that waves and turbulence are linearly combined, then it is possible to use linear filtration methods to remove the wave-driven flow from turbulence spectra. This method was derived by Bendat and Piersol (1971) and is a spectral separation method that uses the coherence spectra between pressure and velocity measured at depth.

The ratio between the vertical gradient of stratification and velocity shear gives an index of turbulent flow activity in the estuary system. A strong vertical density gradient resists the momentum exchange by turbulence; but strong velocity shear tends to create strong vertical overturns and hence high turbulence levels (Dyer, 1997). When a vertical density gradient exists, greater shear is required to overcome the stabilizing effects of stratification and hence keep the momentum exchanging between layers. Miles (1961, 1963) and Miles and Howard (1964) studied the formation and growth of instabilities in a stratified fluid and suggested a criteria for stability: *"The sufficient condition for an inviscid, continuously stratified flow to be stable is when the ratio between vertical density stability and velocity shear is greater than* 1/4*"*. Except for some special cases such as jet-like velocity profiles, this criteria can be very useful to define when active mixing is taking place. When this ratio, which is defined as the Richardson number, is less than 1/4, the velocity shear is strong enough to raise (or lower) water masses vertically through the water column, thus doing work against gravity, and initiating mixing processes between layers.

The cycle of turbulence is closely tied to the cycle of stratification in the estuary as vertical density gradients are likely to inhibit turbulent mixing (Peters, 1997, 1999). The straining of the horizontal density field by the tidal currents results in variability of density stratification over tidal time scales (Simpson, 1997; Simpson et al., 1990). This is termed strained induced periodic stratification. Based on many studies (see for example Lu and Lueck, 1999a,b; Rippeth et al., 2001, 2003; Gregg et al., 1985; Peters, 1997, 1999) it is suggested that estuarine turbulence is highly variable at tidal and spring-neap time scales due to the complex interaction between stratification and shear production. The level of mixing in the water column at temporal scales varying from tidal to spring/neap is then expected to cause flood-ebb asymmetries in the flow, creating residual flows that also vary at the tidal and spring/neap time scales.

The residual flow that defines estuarine circulation determines the net movement of water, biological and sediment transport, and will contribute to the dispersion of water properties. The circulation is driven mainly by barotropic and baroclinic mechanisms as will be discussed further in the next section. Barotropic flow is produced by pressure gradients such as tide or river discharge, while baroclinic flow is created by the spatial density gradient (Pritchard, 1952, 1956). In general, both contribute to generating the residual circulation in the estuary where the net effect is flow down-estuary at the surface and flow up-estuary at the bottom. Stacey et al. (2001) outline that in a stratified water column more shear develops to counteract reduced mixing and hence flood/ebb asymmetries will exist in the profile of velocity shear leading to asymmetries in flood and ebb flow. On ebb, greater flow is at the surface creating a down-estuary residual flow near the surface; on flood the SIPS process creates destabilizing stratification which mixes higher momentum water downward intensifying the bottom currents and leading to up-estuary net flow. Ianniello (1977, 1979) and Li and O'Donnel (1997) showed that barotropic mechanisms can produce significant flood/ebb asymmetries in net transport.

Recently, the role of turbulence on the variation in estuarine circulation has been studied. Nunes-Vaz et al. (1989) tested the role of turbulence in estuarine mass transport and the possibility of tidal time variations of the residual flow. According to their results, baroclinic-driven flow is maximized during slack water because of a minimum in friction velocity and hence turbulence. Based on this explanation, the residual flow in an estuarine system could have a period half that of the semidiurnal tidal period. Stacey et al. (2001) found that the residual flow in a partially stratified estuary can be created as periodic pulses having tidal time scales, resulting from the interaction of shear, stratification, mixing, and asymmetric barotropic forcing.

1.2 Georgia Coastal Environment

The Georgia coastal region is comprised of several barrier islands with many estuarine channels and rivers between them, providing a complicated coastal boundary (see Figure 1.1a). The continental shelf is broad and shallow with a gently sloping bottom ($<$ 40 m depth out 50 nautical miles). Based on oceanographic climatology which regulates the degree of physical processes such as circulation and exchange, the South Atlantic Bight (SAB) is divided

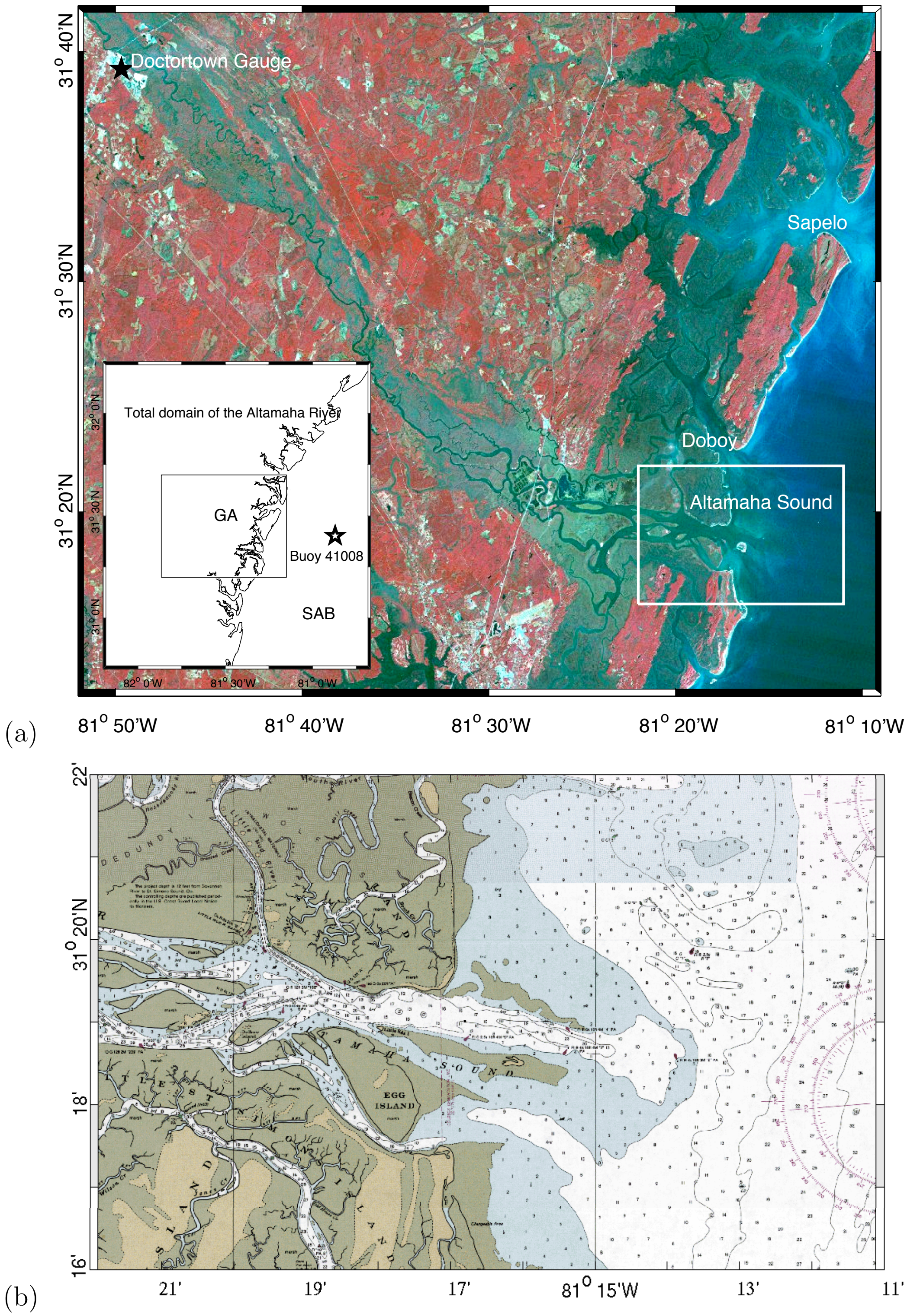

Figure 1.1: The Altamaha River and the GCE-LTER domain: (a) An infrared satellite image showing the Altamaha River from the gauging station Doctortown GA to the coastal ocean, (b) hydrographic chart with bathymetry contours showing Altamaha Sound.

into three depth zones: an inner shelf zone (0-20 m isobaths) which is strongly influenced by river runoff and atmospheric forcing, a mid shelf zone (20-40 m isobaths) which shows mixed responses to wind, Gulf Stream and density forcing, and an outer shelf (40-60 m isobaths) which shows the combined effects of transient Gulf Stream events of 2-14 days in time scale and some wind forcing (Atkinson et al., 1983). Since the inner shelf area is shallow and has a low bottom slope, a low near-shore altitude, and extensive intertidal salt marshes, the Georgia coastal flow can quickly respond to changes in atmospheric forcing (i.e. wind, solar heating, storm surge), tidal forcing (water level, currents), buoyancy forcing (horizontal and vertical salinity gradients), and surface wave forcing.

Salt marshes and estuaries have long been recognized as areas that should be conserved because they are highly productive and provide shelter for marine life. With this in mind, an integrated and systematic study of the river, marsh, estuary and coastal system in Georgia has been developed through funding by the National Science Foundation Long Term Ecological Research (LTER) program. The Georgia Coastal Ecosystems (GCE-LTER http://gce-lter.marsci.uga.edu/lter) project initiated in 2000 builds on the successes of the Georgia River Land Margin Ecosystems Research (GARLMER) project during 1994-1999 (http://lmer.marsci.uga.edu/). These research projects have developed a comprehensive data base for observing and analyzing southeastern estuarine systems. The main goal of this multidisciplinary and interdisciplinary research is to monitor the effects of variable terrestrial, oceanic, and atmospheric inputs on ecosystem function at the Georgia land-ocean margin (Hollibaugh, 1999). The Altamaha, Doboy, and Sapelo watersheds cover the domain of the GCE-LTER project and can be seen in the infrared image of Figure 1.1a.

The physical processes in the Georgia coast are very complex and variable, which is the result of interactions between oceanographic and atmospheric variables such as ocean currents, the density gradient, river discharge, sea level change, bottom friction, wind stress, and sea surface waves (Schwing et al., 1985a). Currents play an important role in water movement and mixing, nutrient fluxes and larval fish transport. Along the Georgia coast, even though there are many kinds of currents (for example, wind and baroclinic-driven currents), tidal currents are dominant with a strong semidiurnal variation associated with the lunar cycle (M2 constituent = 12.42 h period). Semidiurnal currents and sea level are highly correlated, with tidal amplitudes increasing toward shore and tidal propagation moving southward along the shelf (Chen et al., 1999). When tides propagate into the coastal area from the open ocean, the tidal current turns clockwise and the co-range lines are parallel to the depth contour lines (Redfield, 1958; Dame et al., 2000).

Figure 1.2 is a schematic diagram showing physical processes in the Altamaha River estuary during the ebb and flood tidal phases with x eastward, y northward and z upward. During the ebb tide, there are two seaward barotropic pressure gradient forces: tidal wave and river-gauge height difference - quantified by,

$$\frac{-1}{\rho_o}\frac{\partial P_{bt}}{\partial x} = \frac{2\pi U_T}{T_{M2}}\cos(\frac{2\pi t}{T_{M2}}) + g\frac{\Delta H}{\Delta x}, \tag{1.1}$$

where ρ_o is the mean density, T_{M2} is the period of the M2 tidal constituent, U_T is the maximum tidal current speed and $\Delta H/\Delta x$ is the sea surface slope caused by the difference in river gauge heights. The baroclinic pressure gradient force can be approximated as,

$$\frac{-1}{\rho_o}\frac{\partial P_{bc}}{\partial x} = \frac{g}{\rho_o}\frac{\partial \rho}{\partial x}(z-h), \tag{1.2}$$

where $z = 0$ at the seabed. These equations are derived assuming a pressure measurement $p = -\rho g(z-h)$ and a tidal wave having velocity $u = U_T \sin(\omega t)$. A positive horizontal density gradient (along the channel) exists because of fresh water input from upstream. This produces a baroclinic force that linearly decreases as distance from the bottom is increased. Combining all these forces, one baroclinic and two barotropic forces, together with bottom friction, produces a sheared vertical velocity profile with maximum seaward flow at the surface and zero at the bottom. In a similar way, the sheared velocity profile then becomes landward due to the landward tide-driven barotropic forcing during the flood tide.

The vertical shear causes turbulent overturns and an exchange of momentum whose amount is expressed by the Reynolds stress $-\overline{u'w'}$. The turbulent kinetic energy is produced

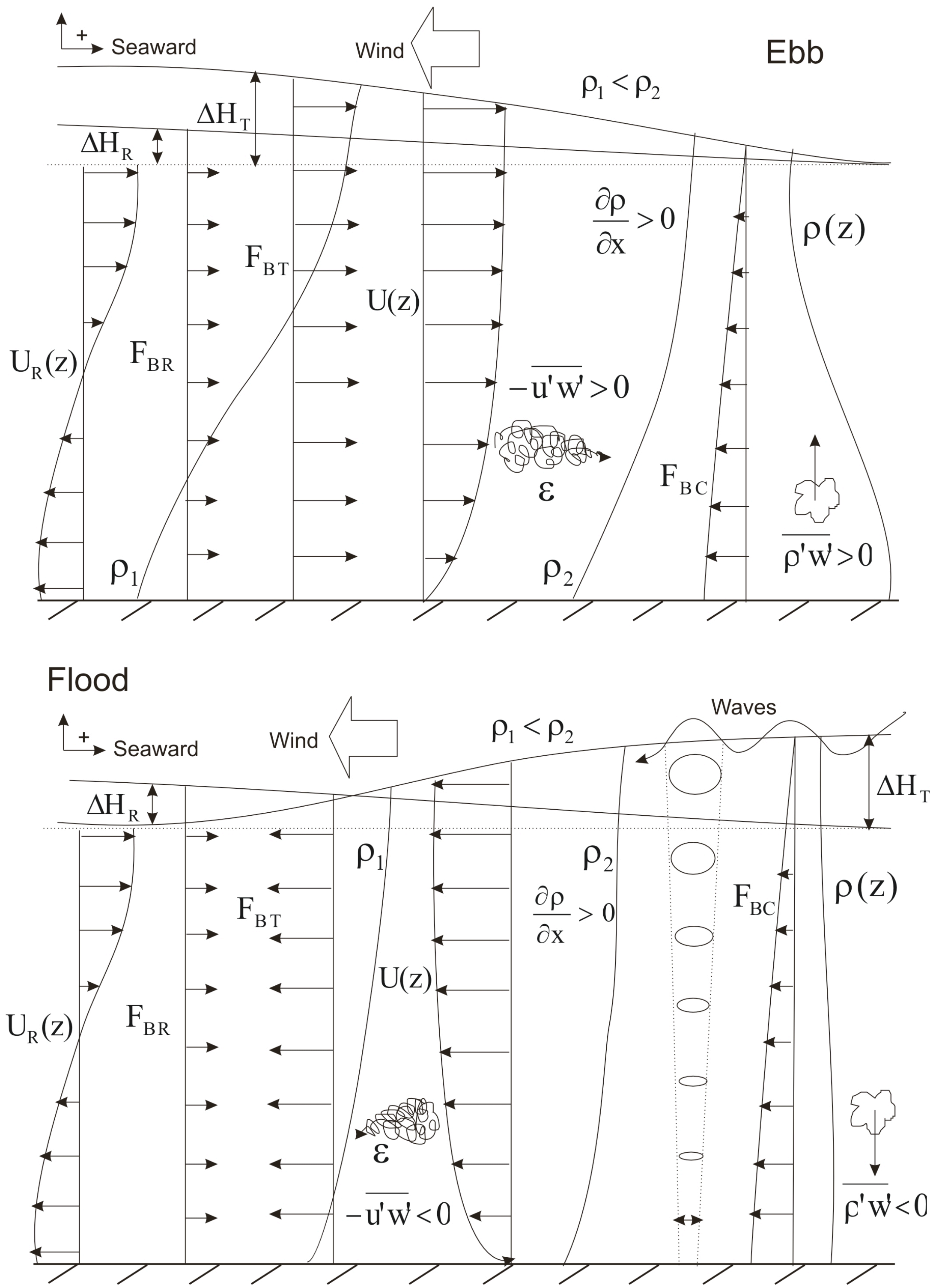

Figure 1.2: A schematic diagram showing the physical processes in the Altamaha River estuary during the ebbing (top) and flooding (bottom) tide.

by the mean shear interacting with the Reynold's stress at the large scales ($P = -\overline{u'w'}\partial U/\partial z$) and is continuously cascaded down to smaller and smaller scales until eventually it is dissipated into heat at the molecular scale (ϵ). Wave motions during the flooding tide have oscillatory motions that overlap the turbulent scales in the Altamaha Sound region as will be discussed in Chapter 2. As a result, waves can affect the measurement of turbulent parameters either by increased kinetic energy at wave frequencies or by increased bottom friction felt by the mean current resulting in possible increases in the friction velocity.

The tidal straining of the horizontal density gradient produces a stable density structure toward the end of the ebb tide because less dense water flows out faster over more dense oceanic water. In this case the stabilizing effects of the vertical stratification creates a buoyancy flux that is an energy sink ($g/\rho_o\overline{\rho'w'} > 0$) because water masses are working against gravity. However, for the flood tide the tidal straining of the horizontal density gradient induces instabilities because more dense water flows in above less dense water, which causes convective overturns and eventually produces vertically homogeneous or weakly stratified conditions. In this case, the buoyancy flux becomes an energy source ($g/\rho_o\overline{\rho'w'} < 0$) because the water motions are working with gravity. This cycle of stratification is termed strained induced periodic stratification (SIPS) described by Simpson et al. (1990).

The spring and neap cycle (14-day period) variation exists in the sea level and current variations along the Georgia coast. During the spring tide, when the tidal forcing is increased, the tidal amplitude and excursion are also increased which means that much of the salt marshes become submerged at high water and exposed at low water. Because of the increased seawater input into the estuary due to strong currents, more active mixing and a vertically homogeneous layer (when river discharge is low) can be expected within the estuary. Strong velocity shears exist within the bottom boundary layer which creates stronger turbulence, potentially increasing the suspended sediment load. During the neap tide, the tidal activity weakens, allowing other forces to be seen in the flow data. For example, baroclinic-driven flow can become a significant parameter contributing to estuarine circulation under neap tide. Subtidal currents generally occur due to wind stress and, when combined with frictional forces, create a complicated current structure in shallow waters (Schwing et al., 1983, 1985b). When the current is combined with wind stress, it produces a clockwise flow relative to the wind, and when currents are combined with bottom stress it produces a counterclockwise flow.

When the tidal forcing is removed by either tidal averaging or harmonic analysis, for example, then the river-driven barotropic and density gradient-driven baroclinic forces create the typical estuarine residual flow: seaward at the surface and landward at depth. Wind can alter the net circulation by either suppressing the net outflow or enhancing it depending on the wind direction. In addition, Stacey et al. (2001) showed that turbulence levels and horizontal density gradients can alter the residual flow over the tidal cycle. If the baroclinic momentum balance is simplified as,

$$\frac{\partial U_{bc}}{\partial t} = \frac{g}{\rho_o}\frac{\partial \rho}{\partial x}(z-h) + \frac{\partial}{\partial z}\left(\nu \frac{\partial U_{bc}}{\partial z}\right), \tag{1.3}$$

where the first term on the right is the baroclinic pressure gradient and the second term is the turbulence with an eddy viscosity parameterization $\overline{u'w'} = \nu \partial U_{bc}/\partial z$, then by scaling arguments Stacey et al. (2001) showed that the steady state velocity is dependent on the horizontal density gradient and the turbulence level (identified by the friction velocity u_*),

$$U_{bc} \sim \frac{\frac{g}{\rho_o}\frac{\partial \rho}{\partial x}h^2}{u_*}. \tag{1.4}$$

So, during slack water where u_* is minimal the baroclinic flow is greatest and during strong ebb and flood flows the friction velocity is greatest and the baroclinic flow is small.

Salinity changes along the Georgia coast and estuaries are determined by factors such as tide, river discharge, precipitation, and water exchange between the continental shelf and the inner shelf (Atkinson et al., 1978; Blanton, 1981; Atkinson et al., 1983). Inside the estuary, the salinity variation shows a strong semidiurnal pattern . However, the tidally averaged salinity is correlated with the annual river-discharge, causing a large range of salinity change(Atkinson et al., 1983; Blanton and Atkinson, 1983). Within Altamaha Sound, (see

Figure 1.1b), the salinity ranges from 15 to 32 psu during low river discharge and from 0 to 25 psu during large river discharge events as will be shown in the experiments discussed here. The lowest salinity along the coast are usually observed in April and May during or after the spring river discharge events. Salinity in late summer and early fall will also decrease depending on the intensity of tropical storm events. The fall is also more prone to Nor'easters which can have an effect on the coastal salinity as the northeasterly winds promote onshore transport (Atkinson et al., 1983). Coastal salinities are maximal during the summer.

One important impact of fresh water input on estuaries is the change in the salinity regime. Presently, this is a challenging issue to scientists and managers who work in estuarine or coastal environments. According to the study of Dame et al. (2000), salinity is not only a good indicator of estuarine circulation but also an important controller of biological productivity, faunal distribution and habitat structure. Three Georgia estuaries, the Altamaha, Satilla and Ogeechee Rivers, have the highest variability of salinity among the estuaries in North and South Carolina, Georgia and Florida. Based on the fact that nutrients affects primary productivity in the coastal area, salinity can directly or indirectly be related to the fishery stocks living along the Georgia coast.

Two types of rivers contribute freshwater to the Georgia coast: the piedmont originating rivers and the coastal plain rivers (Dame et al., 2000). Piedmont estuaries originate from the hilly area of the piedmont and carry suspended clay sediment particles. The piedmont estuaries in Georgia include the Savannah, the Altamaha and the Ogeechee Rivers and provide significant freshwater input to the coastal ocean. Coastal plain rivers are bounded entirely within the coastal plain, have limited drainage, and have high concentrations of humic and tannic acids. These rivers are also called black water rivers. In Georgia, the St. Mary's and Satilla Rivers fall into this category. The median river discharge is lower for the coastal plain rivers (the St. Marys and the Satillais rivers are 15 and 34 m^3/s, respectively) than for the piedmont rivers (the Savannah, Altamaha and Ogeechee rivers are 272, 250, and 61 m^3/s, respectively) (Alber and Sheldon, 1999).

River discharge shows strong seasonal and annual changes. According to time series of monthly median discharge for 30 years (1968-1997) (Alber and Sheldon, 1999) , all Georgia rivers show maximum discharge during February and March, and minimum values in the autumn. This variation can also be seen in the twenty-year mean of coastal runoff from South Carolina to the Georgia coastline to the continental shelf (Blanton and Atkinson, 1983). According to their calculation, coastal runoff reaches a low of 1000 m^3/s in autumn and a maximum of 4000 m^3/s during March. Blanton and Atkinson (1983) studied also the annual change of salinity to the maximum river discharge which occurred 1 month before the lowest salinity. This provided evidence for the inverse correlation between salinity and river discharge. Since the freshwater discharge is affected by the amount of precipitation, the longer-term variation (i.e. inter-annual, decadal or longer) of climatological parameters is connected to long-term changes of salinity in the estuary. According to additional studies (Roplelewski and Halpert, 1986; Gutzler, 2004), the Georgia coast is also influenced by El Niño-Southern Oscillation (ENSO). So, an increase or decrease of precipitation on a climatological scale is connected to salinity change, and eventually it affects the estuarine environment.

Water temperature also shows an annual variation. Air temperatures are maximal in the summer season, and coastal water temperatures become highest in August and September (Atkinson et al., 1983). During the summer, the entire shelf area is covered with water having temperatures exceeding 28℃. As the year progresses, surface waters start to cool and when the Mariners' Fall winds in October cease (Weber and Blanton, 1980), northeasterly winds, combined with surface cooling, then causes rapid mixing leading to a shelf-wide water temperature decrease. Because of these processes, water temperatures drop to 16℃ in December and 14℃ in January. In February the inner coast area is between 12℃ and 14℃ and in April, water temperature starts to increase again as the results of increased solar heating.

The climatological wind forcing along the Georgia coast was described by Weber and Blanton (1980) using marine weather observations from 1945 to 1973. According to their analysis, five seasonal wind patterns are described. Winter (November to February) winds are characterized by northwest to northeasterly winds, with speeds greatest in the northern part of the coast and decreasing in the southern part as winter progresses. Spring season (March to May) is a transitional period where winds shift to southwesterly and southeasterly winds. Summer (June and July) winds are southeasterly and Ekman transport offshore can promote cross-shelf transport of estuarine waters. Fall (August) is another transitional time and Mariners' Fall (September and October) gives the strongest northeasterly winds. During this period, coastward Ekman transport is expected, affecting the nearshore surface salinity value.

1.3 Motivation and Objectives

Estuaries are complex systems in terms of their size, shape, tidal and other forcing mechanisms, salinity classifications and biogeochemistry. In view of this complexity, multidisciplinary efforts are needed in order to understand the systems. However, it is a challenge to observe estuarine physics in detail because the water is so shallow and poses many constraints on instrumentation deployments. As new observational methods have developed it is increasingly possible to extend the study of estuarine physics. For example, turbulence measurements in shallow estuaries became possible after the development of high frequency acoustic Doppler technology.

Turbulence plays an essential role in the estuarine environment. It also affects the activity of planktonic organisms. From a biological oceanographic viewpoint, turbulence has been considered to be a key factor regulating ecological dynamics in coastal and estuarine systems. As turbulence exists from the smallest scales to the largest it plays a key factor in moving nutrients upward into the water column from below and also affects the encounter rate between prey and predator by bringing organisms together or dispersing them apart (Osborn, 1996; Rothschild and Osborn, 1988; Seuront et al., 2001; Kelley et al., 1998). Seuront et al. (2001) comments that turbulence can increase the rate of predator-prey encounters up to a factor of 60 with greater effects on slow moving or non-swimming organisms. Rothschild and Osborn (1988) suggested that turbulence plays an important role in planktonic food webs, patch formation, nutrient exchange, and dissipation. Osborn (1996) studied the effects of turbulent diffusion on copepods and found that predators can use turbulent flow and diffusion as a feeding current. So, based on these previous study results, it is clear that turbulence needs to be studied in detail and in a variety of systems because many physical processes contribute to its development, persistence and dissipation and the larger scale flows are then affected by it. Also, numerical circulation models rely on parameterizing the turbulent processes in order to predict salinity and water quality regime and transport properties.

In order to understand turbulent flow characteristics in estuaries, several questions need to be answered. First, how do the Reynolds stresses and turbulent kinetic energy change with the tidal period? Is the tidal current-induced velocity shear the most important source of turbulent kinetic energy in the estuary? Second, are the turbulent kinetic energy (TKE) production and dissipation rates balanced? Generally, we assume that the TKE production and dissipation around the bottom boundary layer is balanced under steady state, so then to what degree is this satisfied? Thirdly, how does the turbulent flow change with increasing river discharge? Fresh water is the main source of the vertical and longitudinal density gradient in an estuary, so answering this question provides useful background for interpreting estuarine circulation pattern.

Studying turbulence and wave effects together is necessary in order to separate their effects. Surface waves typically produce velocity variances that are larger than those related to the turbulent flow. They have overlapping spatial scales so they are a factor to consider for turbulence studies (Lambrakos, 1982; Grant and Madsen, 1979). To study the effects of waves in this shallow study area it was necessary to answer several questions: (1) How do the wave characteristics change from the inner shelf to inside the estuary? (2) Which factor is dominant in affecting wave energy propagation: tidal flow or bottom topography? and finally 3) What are the implications of the wave field on the larger scale flow?

The final factor considered here involves estuarine circulation and net transport. Traditionally, moored current measurements at specific locations are used to examine the time variability of the circulation by using tidally averaged data or principle component analysis. However, these methods do not show spatial variations of the current field. Towed acoustic Doppler current profilers (ADCPs) provide an excellent opportunity to view the two-dimensional flow over tidal time periods. As ship-time is an expensive resource the measurements were limited to 13 hours. One drawback of this roving method is that the location of each track is not exactly at the same place as previous tracks, but rather depends on the precision of the ship GPS, wind and current flows. With these limitations, the dominant tidal components were fit to the data and the residual flow computed. The question was: What are the temporal and spatial variations of the residual flow?

1.4 An Overview of the Dissertation

This dissertation describes the characteristics of several physical processes such as waves, the cycle of turbulence, and estuarine circulation in the Altamaha River estuary using several observational data sets and numerical modeling approaches. This study focuses on the tidal and spring/neap temporal variability of physical forcing from tides, river discharge, density gradients, and waves. Each chapter is independent and organized in a manuscript format with submissions to appropriate journals. They are linked by one common theme and that is the characteristics of turbulence and its effect on estuarine flows. The contents of the dissertation are organized as follows:

Chapter 2 focuses on wave propagation and the effects of changing topography, sea level and currents on the wave characteristics. Specifically, it shows how wave energy is transformed as it propagates over a region spanning the mid-shelf of the South Atlantic Bight to the Altamaha River Estuary using state of the art instrumentation and a freely available phase-averaged spectral wave model. As directional wave spectra are not available along the Georgia coast we make use of the acoustic Doppler current field together with a pressure sensor to measure the directional wave properties incident along the Georgia coast and compare to measurements within the estuary. Simulations of wave energy deformation during wave propagation are also presented to determine whether ebb shoaling or currents dominate the wave properties in this area. Given the wave field within the estuary we then extend the observations to a discussion of its effect on the current boundary layer.

In chapter 3, the turbulent flow characteristics (i.e. Reynolds stresses, turbulent kinetic energy (TKE), shear production and dissipation rates of TKE, buoyancy flux, and water column stability as a function of the tidal period) are presented from observations and compared to modeled parameters using a simple 1-dimensional numerical turbulence model. In obtaining some of the observed turbulence parameters it was necessary to first eliminate the effects of waves on the high frequency-sampled velocity data in order to extract the pure turbulent motion. Comparison of turbulent flow characteristics between low and high river-discharge cases are then presented to show how vertical and horizontal density gradients affect turbulent mixing and the balance of the TKE budget. The turbulent model was then used to examine its feasibility and limitation, and to predict these characteristics over the full water column.

Chapter 4 describes the residual flow and net transport of water from 13-hours of roving ADCP data. This chapter introduces the processing method of towed ADCP data and simply estimates residual flow by subtracting the dominant tidal constituent from depth-averaged current data. The comparison between total and residual volume transport is given in order to see the temporal variation over a tidal time scale. The 2-dimensional distribution of the residual flow is then analyzed for spatial variations.

Chapter 5 contains the overall conclusion of the dissertation with a section recommending future areas of study that involve instrumentation deployments and data not previously obtained. It is hoped that these experiments will give further insight on the cycle of turbulence and circulation in an energetic estuary with highly variable stratification and horizontal gradients.

Chapter 2

DEPTH- AND CURRENT-INDUCED EFFECTS ON WAVE PROPAGATION INTO THE ALTAMAHA RIVER ESTUARY, GEORGIA[1]

[1]Ki Ryong Kang, Daniela Di Iorio, Submitted for publication in *Estuarine, Coastal and Shelf Science,* 12/2004

Abstract

A study of sea surface wave propagation and its energy deformation was carried out using field observations and numerical experiments over a region spanning the midshelf of the South Atlantic Bight to the Altamaha River Estuary, GA. Wave heights on the shelf region correlate with the wind observations and directional observations show that most of the wave energy is incident from the easterly direction. After interacting with the shoaling region of the Altamaha River, the wave energy within the estuary becomes periodic in time showing wave energy during flood to high water phase of the tide and very little wave energy during ebb to low water. This periodic modulation inside the estuary is a direct result of enhanced depth and current-induced wave breaking that occurs at the ebb shoaling region surrounding the Altamaha River mouth at longitude -81.23. Modelling results with STWAVE showed that depth-induced wave breaking is more important during the low water phase of the tide than current-induced wave breaking during the ebb phase of the tide. During the flood to high water phase of the tide, wave energy propagates into the estuary. Measurements of the significant wave height within the estuary showed a maximum wave height difference of 0.4 m between the slack high water (SHW) and slack low water (SLW). In this shallow environment these wave-current interactions lead to an apparent bottom roughness that is increased from typical hydraulic roughness values, leading to an enhanced bottom friction coefficient.

Keywords: wave energy propagation, wave breaking, ebb shoaling, boundary layer, Altamaha River Estuary

2.1 Introduction

Of all the various types of fluid wave motion that occur in nature, surface water waves are not only the most easily observed but of great scientific importance because of their impact on coastal and offshore structures, their role in sediment transport and coastal morphology, their effect on estuarine circulation and their overall effect on the energy and momentum exchange between the atmosphere and ocean. Both observations and models of the wave field are required for a variety of these applications and verifications including coastal engineering and near-shore dynamics, beach erosion, waste dispersal and pollution studies (Wiberg and Smith, 1982; Grant and Madsen, 1979; Mellor, 2002).

Surface waves interacting with the seafloor can create turbulent boundary layers that make significant contributions to wave energetics, dissipation rates, and fluid-sediment interactions (Trowbridge and Madsen, 1984a,b; Mathisen and Madsen, 1996a,b; Styles and Glenn, 2002b). Wave energy dissipation rates in the bottom boundary layer are a function of important environmental parameters, such as wave heights, wave frequencies, local water depth, bottom roughness (including sand ripples), and mean current conditions (Grant and Madsen, 1979). Small-scale boundary layer processes at the sea bed in shallow water are strongly influenced by wave motions. The wave-induced water particle motions are a key factor to understanding several issues such as beach shape change, bottom morphology, water clarity, and bottom friction experienced by mean currents.

The South Atlantic Bight strongly influences the meteorology of the eastern seaboard (Atkinson et al., 1983). The paths of winter cyclones, also known as extratropical cyclones or Northeasters, that impact the U.S. east coast, cross the region. Also, many tropical storms and hurricanes pass through this area in summer and fall. As these systems and their resulting waves come close to the eastern seaboard their impact on the coastal shore become critically important because of wave-induced or longshore currents. Present studies of storm events rely on coverage provided by ocean buoys through the National Oceanic and Atmospheric

Administration (NOAA) National Data Buoy Center (NDBC) and other regional coastal stations, however directional information is often lacking.

The Georgia coastal region is comprised of many barrier islands with many estuarine channels and rivers between them. The Altamaha River estuary which is bounded by Sapelo Island above and Sea Island below is a typical coastal plain estuary, which has extensive salt marshes, low islands (see Figure 2.1), and a monthly median discharge of 250 m^3/s with peak flow during early spring (Alber and Sheldon, 1999). The estuarine flow is driven by fresh water discharge, tidal-,and to a lesser extent wind- and wave-induced flow. The tidal range can be as much as 1.5 to 3.0 meters with correspondingly strong currents (1m/s) (DiIorio and Kang, 2003). The Altamaha River is the main source of freshwater ouput to the coastal ocean in the South Atlantic Bight. The depth and width of the main channel connecting the Altamaha River to the coastal ocean are approximately 7 m and about 1 km respectively. The coastal morphology is very complicated and a particular feature in the bottom topography is a bar surrounding the mouth of the estuary.

Surface waves generated by offshore winds propagate to the coastal environment where they are more strongly affected by topography, current and sea level changes. In this shallow water environment the wave field can have an affect on the bottom drag and hence the circulation and mixing processes. The theoretical studies of Bender and Wong (1993) showed that wave-current interactions with a tidally forced estuarine circulation play a role in increasing the bottom friction felt by the tidal current and in decreasing the water transport in the bottom boundary layer. Gonzalez (1984) showed from a case study of wave-current interaction at the Columbia River entrance that the offshore wave energy can propagate toward the river entrance interacting with the current, and that the wave height decreases during flood (following the current) and increases dramatically during ebb (opposing the current). The opposing current retards the advance of a wave and a following current enhances the advance of a wave. Under the opposing current case, the wave energy transport can be completely

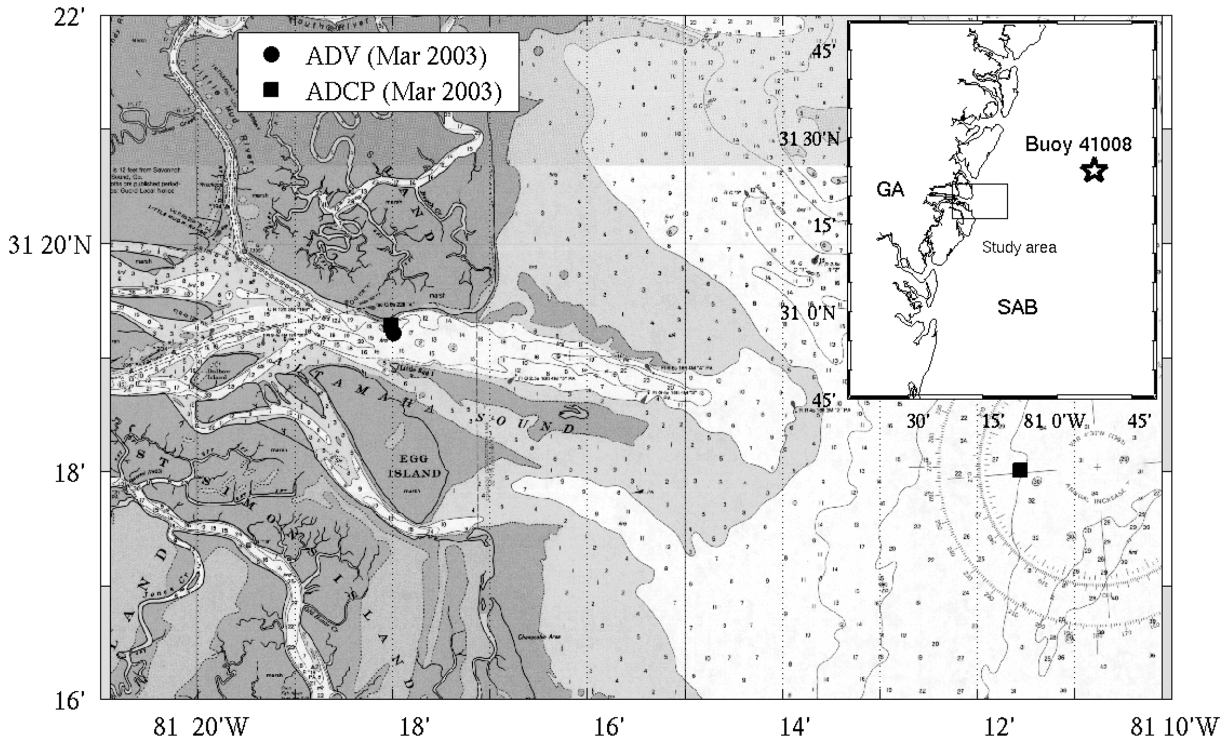

Figure 2.1: Georgia coastal study area showing deployed instrumentation on a hydrographic chart of the Altamaha River Sound.

blocked when the upstream component of the wave group velocity is exactly matched by an equal current velocity.

As waves approach shallow water, their wavelength gradually decreases and their wave heights increase, which increases their steepness. The theoretical and observational study of wave breaking processes has been carried out by many researchers (see for example Suhayda and Pettigrew, 1977; Battjes and Janssen, 1978; Thornton, 1979; Guza and Thornton, 1980; Thornton and Guza, 1982, 1983; Hir et al., 2000). When waves break at a certain depth there is wave energy transformation, a release of wave energy to the water column which has implications for sediment transport processes, and there is turbulent energy dissipation (Seymour, 1989; Horikawa, 1978). In our shallow water domain, we expect wave energy transformations to be periodic with the tidal flow as waves propagate from the mid shelf to the estuarine environment and interact with the current and sea level height.

The main questions to be addressed in this study are: 1) How do the wave field characteristics change between the inner shelf and the estuary? 2) Which factor dominates wave propagation in this area - tidally modulated sea level changes or current flow? and finally 3) What are the influences of the wave field on the larger scale flow? In order to answer these questions we first describe in section 2 the experimental setup. Section 3 describes the observational results obtained on the mid shelf, inner shelf and within the estuary. In section 4, we introduce the STWAVE model, provide model simulation results in comparison to observational results, and carry out mechanistic studies focused specifically on tidally induced sea level changes and current flow. Section 5 summarizes the findings with regard to wave-current-bathymetric interactions and discusses implications for circulation/turbulent processes.

2.2 Observational Setup

A field observation, for studying the characteristics of wave propagation into the Altamaha River Estuary, was carried out over a neap/spring tidal cycle from March 25 to April 2,

2003. The observations were designed specifically to quantify changes in wave characteristics on the mid-shelf, inner shelf and within the estuary itself and to compare to model results. Figure 2.1 shows a hydrographic chart of the study area in relation to the Georgia coast and locations of deployed instrumentation.

Midshelf wave and wind properties were obtained from the NOAA National Data Buoy Center station 41008, 32 km offshore of Sapelo Island GA. The data buoy measures most wave parameters including wave heights, periods and wave energy spectrum every hour based on 20 min of data sampled at 2.56 Hz. It does not, however, provide directional wave statistics. Hourly averaged meteorological data including wind speed and direction at approximately 5 m above the sea surface were also obtained from this station.

On the inner shelf, a 600 kHz RD Instruments acoustic Doppler current profiler (ADCP) with the waves array firmware and software package, was deployed at 10 m depth. Current velocity profiles were sampled every 6 min with 0.5 m bin spacing. Directional wave data were sampled for 20 min every hour at a sampling rate of 2 Hz giving a maximum frequency of 1 Hz for wave characteristics. Manufacturers software based on algorithms developed by Terray et al. (1997) provided directional wave energy spectra $S(f, \theta)$.

Within the estuary a 1200 kHz ADCP was deployed at 9 m depth for monitoring the current through Altamaha Sound. The current was sampled every 6 min with 0.25 m bin spacing. A SonTek acoustic Doppler velocimeter (ADV) was moored approximately in the middle of the channel in 8 m depth to observe the bottom boundary layer turbulent flow characteristics and the wave properties at 1.4 meters above bottom (mab). The ADV was programmed to sample three bursts every 30 min with the first burst, designed for turbulence studies, consisting of 5.7 min sampling at a frequency of 25 Hz followed by a second burst, for wave studies, consisting of 17.5 min sampling at 4 Hz, and for mean currents, consisting of 5.8 min sampling at 0.1 Hz. These measurements within the estuary were taken during a time of maximum freshwater discharge for 2003. The transport of 1800 m^3 s^{-1} occurred during the spring month of Mar/Apr (see Figure 2.2).

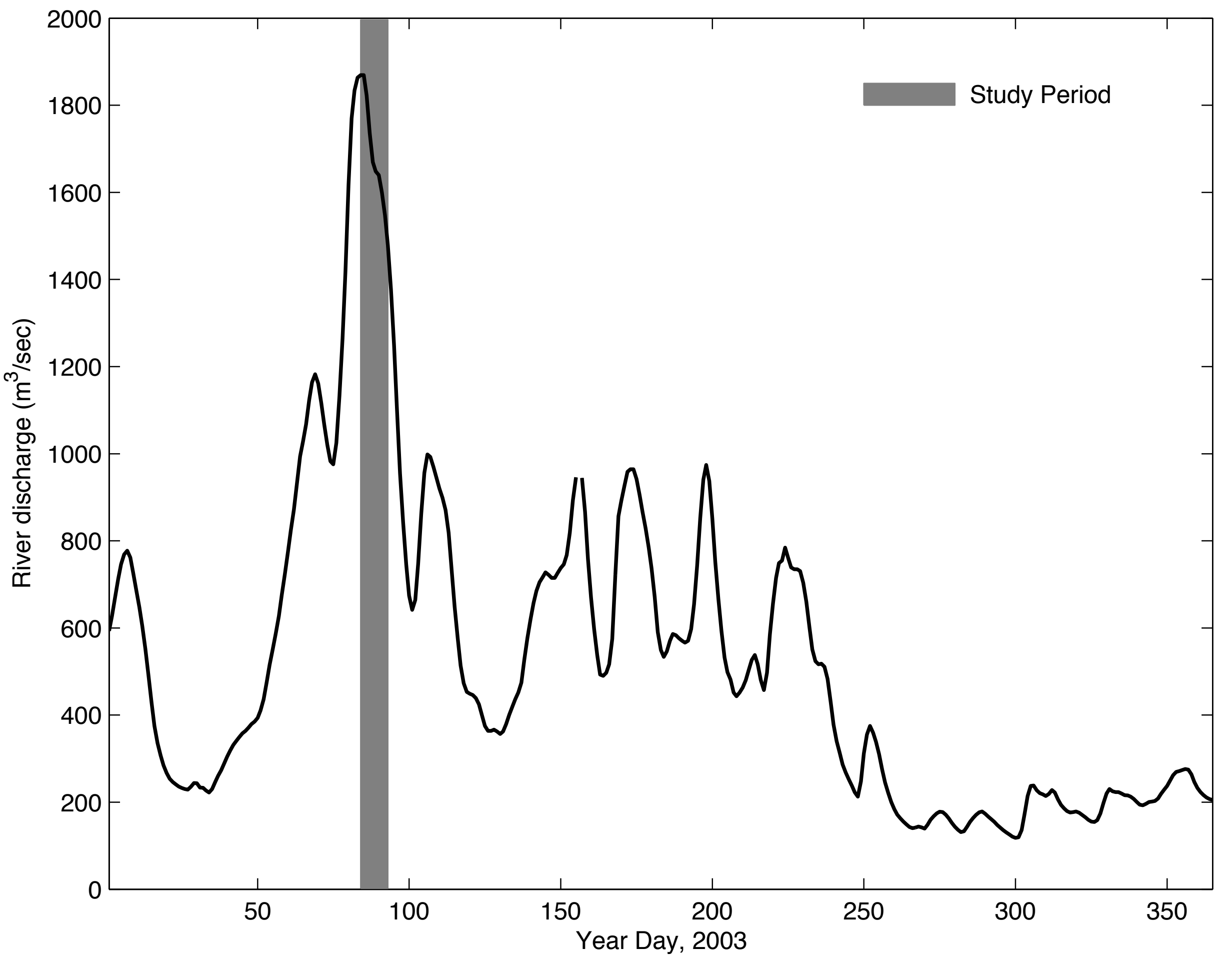

Figure 2.2: Altamaha River discharge in 2003 with highlighted zone corresponding to the experimental period.

2.3 Observational Results

A summary of the wind speed and direction together with surface wave energy on the midshelf (at 20 m depth), the inner shelf (at 10 m depth) and within the estuary (at 8 m depth) over the experimental duration is shown in Figure 2.3. These data are presented to show how the wave energy as a function of frequency changes with temporal and spatial characteristics as the waves approach and propagate into the estuary. The energy density as a fuction of direction is also shown for the inner shelf 10 m measurement. Winds were typically from the northerly direction with short period southerly wind bursts. Maximum speeds observed were in the range between 10-15 m s^{-1} from the northerly direction. The surface wave energy for the mid shelf (obtained directly from the NOAA NDBC station 41008 historical data archives) is plotted as a function of wave frequency and time, and corresponds well to the wind events at that location: the onset of strong winds causes increased wave energy that persists for a few days.

The inner shelf wave energy spectral properties ($S(f) = \int_0^{2\pi} S(f,\theta)d\theta$ measured with the ADCP follow closely the midshelf results, but with some attenuation. The wind-generated waves in the coastal domain have very similar frequency and temporal characteristics even though there is some decrease in energy levels. The inner shelf spectral modulation with frequency that is most evident around Year day 89 is a direct result of the dispersion relation $\omega = \mathbf{U} \cdot \mathbf{k} + \sqrt{gk \tanh kh}$ for waves riding on a current (ω is the radian frequency, U is the mean tidal flow, k is the radian wave number, g is gravity and h is the mean depth). When the current is flooding (i.e. waves propagating in the same direction as the current toward the shore) the frequency is increased and when the tide is ebbing (i.e. waves propagating against a current flowing seaward) the frequency is decreased. The wave energy density directional properties obtained from the directional wave spectrum is calculated by $D(\theta) = \int_0^{\infty} S(f,\theta)df$, and show that the swell dominated waves are predominantly incident from the East (100^{o}T) with some waves coming from the northerly and southerly direction during the storm events on Year days 90 and 92, respectively. These directional wave statistics will be used for

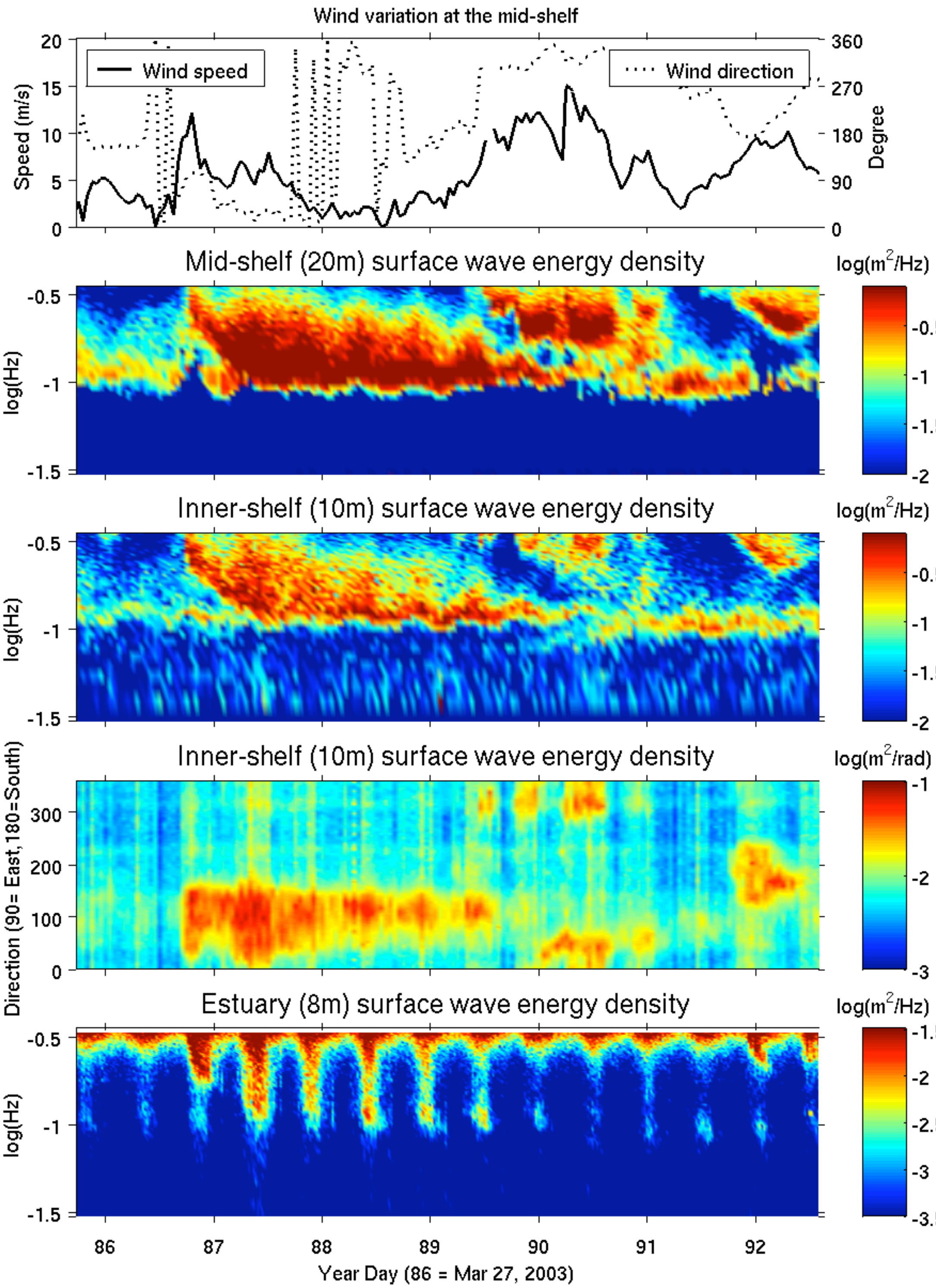

Figure 2.3: Atmospheric wind variability and surface wave energy spectrum taken on the midshelf from the NOAA NDBC; the directional surface wave characteristics measured on the inner shelf; The surface wave energy measured within the estuary.

modeling the wave properties toward the coastal region and into the estuary in order to understand where wave breaking is most enhanced as a result of water depth over the ebb shoal and/or a result of current flow.

From the ADV pressure sensor within the estuary we estimate the surface wave energy spectrum using linear shallow water wave theory (Bowden, 1983). The pressure data measured at 1.4 mab was used to estimate the wave energy spectrum with Welch's periodogram method (Press et al., 1992). Each 17.5 min burst of data (4200 samples) was divided into seven segments having 1024 data points with 50% overlap. In order to obtain a smoothed spectrum a Hanning window with a periodic and positive filter, was applied to each segment and the seven spectra were averaged to obtain a single power spectral density at 512 frequency values. After compensating for depth attenuation effects the spectra were cut off at a frequency of 0.33 Hz because of noise levels and because at higher frequencies (hence large wave numbers) the spectra are exponentially amplified. For this frequency range, wave periods greater than 3 seconds are included. The wave energy results in Figure 2.3 show a clear temporal cycle within the estuary. The wave height energy is significantly reduced compared to the inner and mid- shelf and is greatest during the flood to slack high water phase of the tide compared to the ebb to slack low water phase of the tide (as will be shown).

Figure 2.4 shows the tidal elevation, significant wave heights and the current speed characteristics at various stations. Tidal excursions within the estuary typically range from 1.5 - 3 m over the neap/spring cycle. Neap tide occurred on Year day 83 three days before our measurement program and Spring tide occurred on day 91 with heights of 2.2 m. The significant wave height defined as, $H_s = 4\sqrt{\int_0^\infty S(f)df}$ is calculated based on the wave spectra $S(f)$ shown in Figure 2.3. The offshore significant wave heights approach values of 2 m with strong correlation with the wind events shown in Figure 2.3. As the waves propagate toward the shore the significant wave heights are attenuated, presumably due to energy dissipation by bottom friction across the broad, shallow continental slope, to maximum values of 1.5

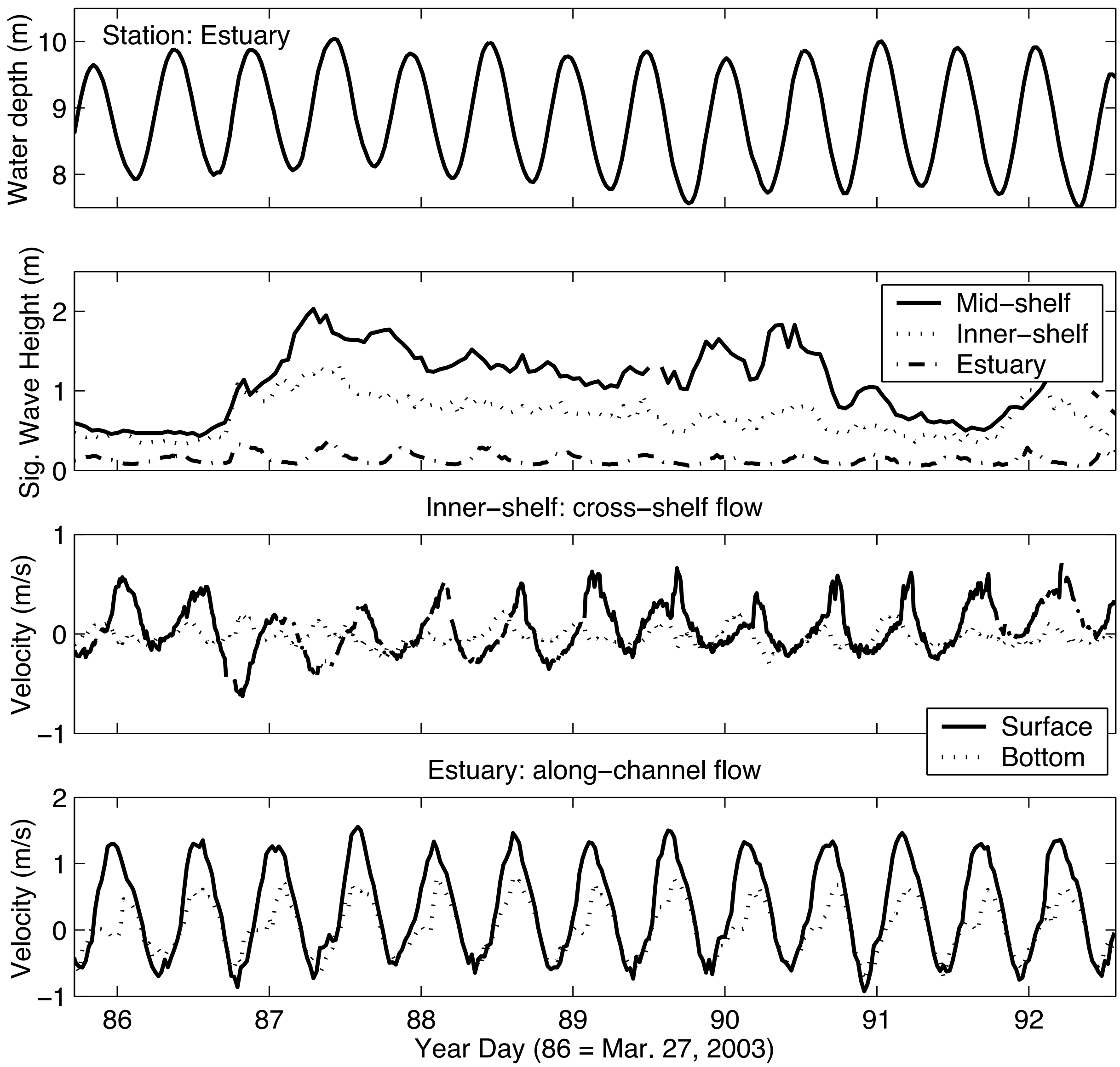

Figure 2.4: The tidal variability observed within the estuary; the significant wave heights for the midshelf, inner shelf and estuarine stations; the surface (2 m depth) and bottom (2 m above bottom) current on the inner shelf and in the estuary. Positive current is seaward and negative is landward flow.

m at the inner shelf station. Further wave height attenuation and temporal filtering to a semi-diurnal periodic cycle is then observed within the estuary. Maximum significant wave heights calculated were typically 0.25 m (and compare favorably to model results, as will be discussed) and predominantly occurs approximately 1 hour before the maximum sea level height (see Figure 2.5); slack water occurs shortly after the maximum sea level height. Similar wave height magnitudes and time delays were obtained during an observational study conducted in 2001 when the river discharge was significantly reduced to approximately 200 m^3/s.

The surface and bottom currents on the inner shelf and within the estuary are also shown in Figure 2.4. The current speed is resolved into components across the shelf at the inner shelf station (the dominant direction for the tidal ellipses) and along the tidal channel at the estuarine station. The tidal currents in this region are dominated by the principal lunar semidiurnal M2 cycle. During this time of high river discharge the flow within the estuarine channel was strongly ebb-dominant giving sheared flow and a prolonged ebb current. The tidally and depth averaged flow out of the estuary was 15 cm/s. On the inner shelf the flow was much slower but also sheared due to near zero flows near the bottom. During the flooding tide and continuing toward slack (negative flow for a coordinate system where positive is towards the East and North), the significant wave heights increased to a maximum just before slack high water (see Figure 2.5). During the ebbing tide and continuing until slack low water the significant wave heights were minimal. This suggests that mechanisms other than wave-current interactions decrease wave energy as waves propagate into the estuary. To find out what is the dominant mechanism for this observed flood-ebb asymmetry we explored the effects of wave shoaling (wave-bathymetry interactions) and wave-current interactions using a steady-state spectral numerical wave model developed by Smith et al. (2001).

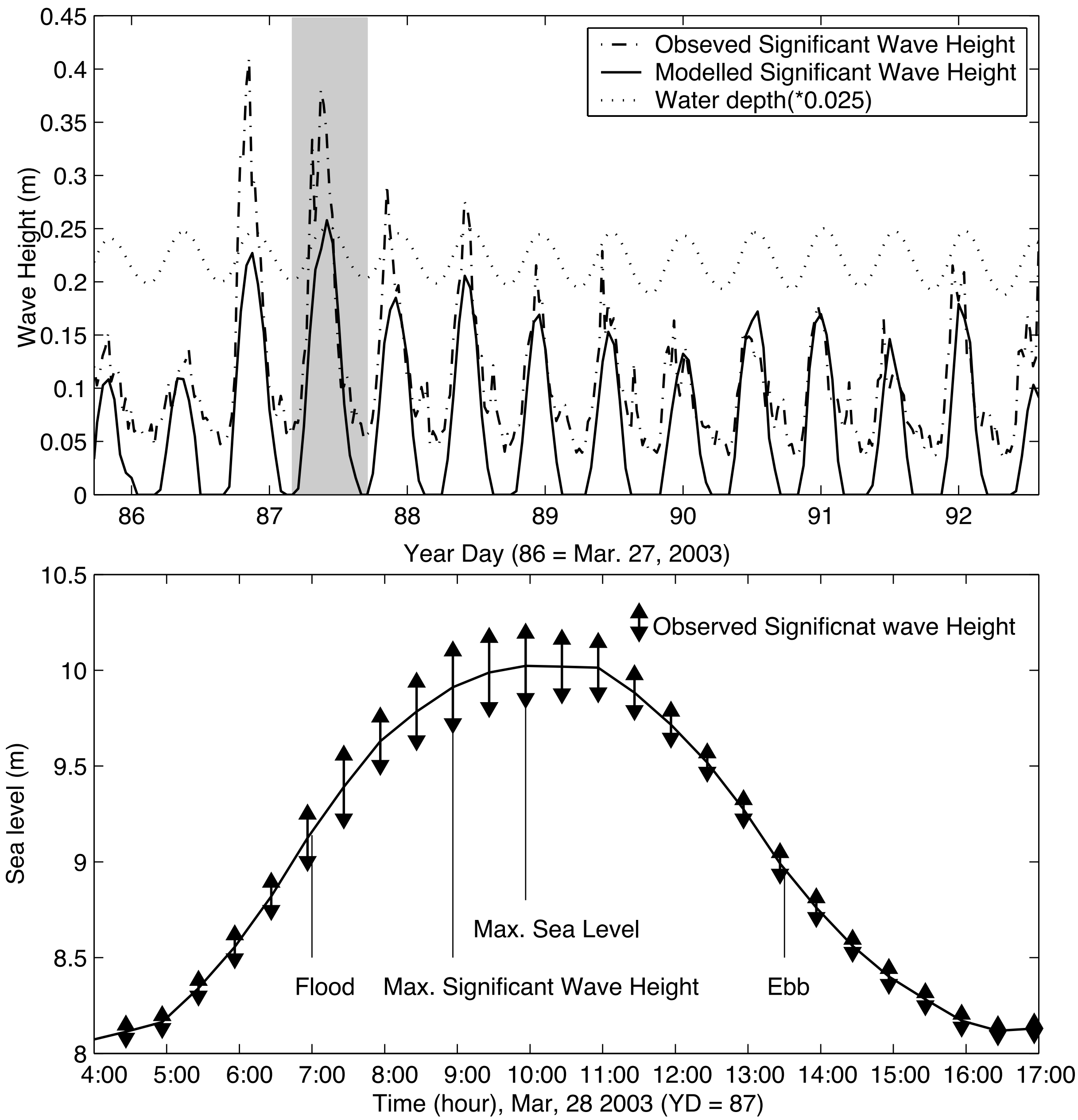

Figure 2.5: The measured and modeled significant wave heights within the estuary compared to the tidal height variation; The observed significant wave heights superimposed on the tidal height over one tidal cycle. The time of maximum flood, maximum wave height and maximum sea level are also identified showing a time delay between events.

2.4 Numerical Simulation

Nearshore wave propagation is mainly influenced by bottom topography (including shoaling due to sedimentation), currents (including tide-, wind- and wave-driven currents), and sea level changes (Massel, 1996). Based on our observations, we explored the possible influence of wave-current-bathymetric interactions on wave propagation into the Altamaha River estuary. In this section, we briefly introduce the spectral wave model used in this study together with model results. The main focus of this section is to determine if the wave model is capable of capturing the wave characteristics within the estuary as observed and to identify the primary physical processes responsible for those characteristics.

2.4.1 The Numerical Model

The numerical model used in this study is the STeady-state spectral WAVE (STWAVE version 4.0) model developed by Smith (1999) and co-workers (Smith et al., 2001; Smith and Smith, 2002; Smith and Resio, 2004). It is a phase-averaged steady state spectral model based on the conservation of wave energy. STWAVE simulates depth-induced wave refraction and shoaling, current-induced refraction and shoaling, depth- and steepness-induced wave breaking, diffraction, wave growth because of wind input and wave-wave interaction, and white capping that redistributes and dissipates energy in a growing wave field. Some assumptions and limitations in the model include: only landward-moving wave energy, negligible wave reflections, mild bottom slope, linear refraction and shoaling, and negligible bottom friction. With these assumptions, the wave action, the dispersion relationship, wave celerity and group wave celerity can be solved under the assumption of linear wave theory. This model has been applied to coastal and estuarine environments and showed good agreement with observed wave data (Gailani et al., 2003; Cialone and Thompson, 2003; Militello and Kraus, 2001; Smith and Smith, 2001; Smith and Gravens, 2002; Nygaard and Eik, 2004).

Input to the model can include an incident directional spectrum at the seaward boundary (assumed to be spatially homogeneous along the boundary), local wind speed and direction (assumed to be uniform over the model domain), and a spatially varying current (assumed to be uniform with depth) over the model domain. The main input model parameters used in this study are the bottom bathymetry, the directional wave spectrum as measured by the inner shelf ADCP, a uniformly distributed and time varying current field based on point measurements in the estuary and on the inner shelf, and the wind stress obtained from the offshore buoy. Output from STWAVE includes wave parameters such as the zero-moment wave height (H_{m_0}) or the significant wave height ($H_s = 4\sqrt{H_{m_0}}$), wave period and wave breaking index associated with depth- and steepness-induced wave breaking (using the breaking relationship $H_{m_{0\max}} = 0.1L \tanh kh$, where L is the wavelength, k is the wave number, and h is the depth) over the entire model domain and directional spectra from selected points (Smith, 1999). The model will also output the depth- and current-induced wave refraction, wind-wave growth, and wave-wave interaction which is directly related to wave energy redistribution and dissipation in the wave field (see Smith et al., 2001, for more details).

Figure 2.6a shows the bottom bathymetry and topographic features relative to mean sea level within the model domain. The model grid is formulated with the same resolution as the bathymetric grid with 100 by 140 cells corresponding to approximately 80 m of latitude and longitude respectively. The x-axis is oriented toward the East and the y-axis is oriented toward the North. The directional wave spectrum from the ADCP moored on the inner shelf (identified as the eastern white diamond in Figure 2.6a) is used as the wave forcing on the boundary. The frequency range for the model input is from 0.0078 to 0.5 Hz, and the directional increment is 5 degrees. We only consider those waves propagating into the model domain from the ocean as significant. That is, wave energy not directed into the grid is neglected which means only those waves having incident angles ranging from 5 to 175^o from Noth are considered. A sample of the measured directional wave spectrum that represents a time of high significant wave height (Year Day 87.3) is shown in Figure 2.6b.

We forced the model with the directional wave observations obtained on the inner shelf and we ran it from Mar 26 (15:00) to April 2 (14:00), 2003 with a temporal resolution of

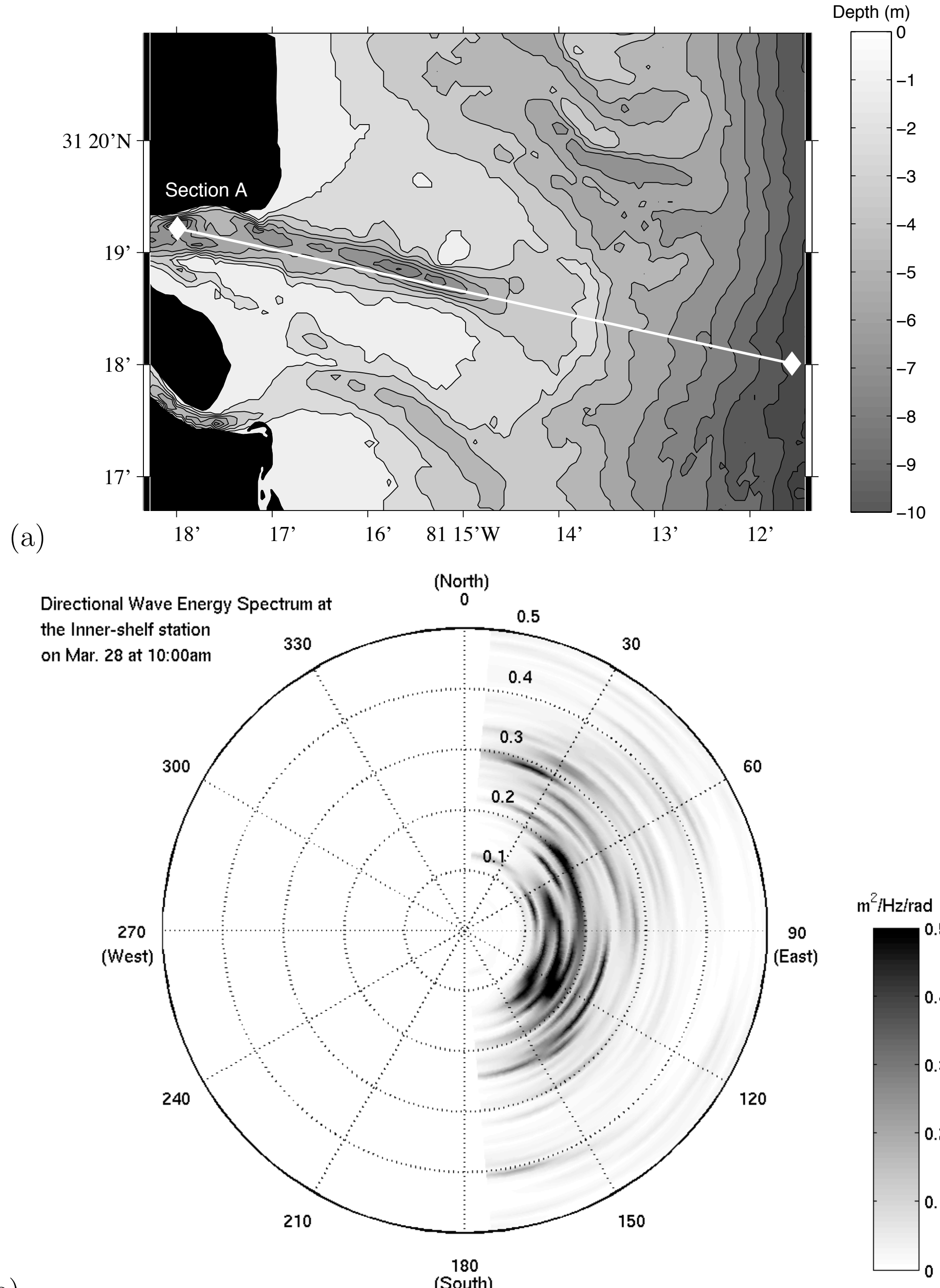

Figure 2.6: (a) Bottom bathymetry relative to mean sea level obtained from the NOAA National Geophysical Data Center. White diamonds represent the mooring locations for instruments on the inner shelf and within the estuary. Wave model output will be focused over the whole domain and along the transect identified as Section A which connects the deployment sights. (b) Sample directional wave spectrum incident on the coastal boundary. The radial axis is the frequency value in Hz

1 hour. First we analyzed the temporal variability in the wave field along section A shown in Figure 2.6 using the directional wave characteristics, spatial mean current, wind and sea level height all varying as a function of time. We calculated a mean of all depth-averaged current data obtained from each mooring location (one on the inner shelf and one in the estuary). This mean is then uniformly distributed onto the model domain. Spatial variations in the current field caused by buoyancy, wind and topographic steering were neglected. Ideally a more accurate representation of the two dimensional (horizontal) current field can be obtained from two dimensional or three dimensional circulation models which are then coupled to the wave model. The tidal height relative to mean sea level was applied uniformly to the bathymetric data at hourly intervals. Despite these limitations in data input, the model captured the observed temporal characteristics within the estuary as will be shown below.

Then we examined the spatial characteristics of the wave field over the whole domain and along section A for different times in the tidal cycle (slack low water, flood, slack high water, and ebb) assuming a constant directional wave forcing shown in Figure 2.6b, a homogeneous velocity field throughout the domain during flood and ebb, and zero wind effects so that wave development within the estuary was ignored. This mechanistic study was setup to determine which effect (tidal height or current) is dominant in determining the wave characteristics in the estuary.

2.4.2 Model Results

Figure 2.7 shows the temporal variability of the significant wave height as a function of longitude along section A, which connects the inner shelf to the estuary. The significant wave height at the East boundary is essentially those observed in Figure 2.4 since the model is forced with these observations at the boundary. As the waves propagate westward toward the estuary the significant wave heights start to increase after longitude -81.22 and undergo breaking at longitude -81.23 as shown by the wave breaking index (either 1 or 0) along section

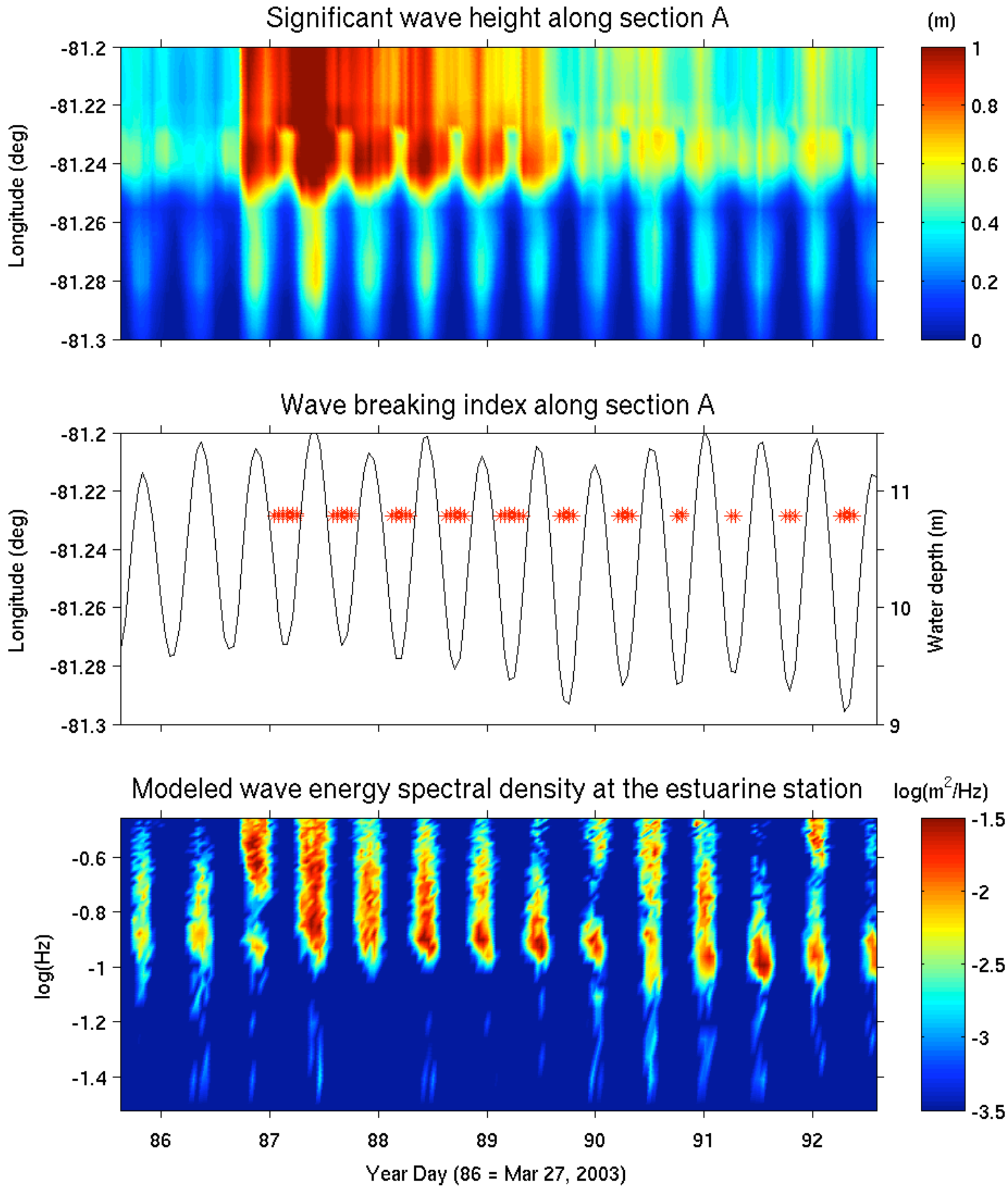

Figure 2.7: Time series measurement of the model-computed significant wave height and wave breaking index as a function of longitude along Section A; The modeled wave spectral density within the estuary.

A. This enhanced breaking occurs during maximum ebb to slack low water and persists into the start of the flood tide and occurs at the shallow sill that exists at the Altamaha River mouth at longitude -81.23 (refer to Figure 2.6). On Year day 86.1 the incident wave energy on the boundary was small and so no wave breaking occurred along section A, although significant wave height reduction exists because of deeper waters within the estuary. As a result of wave breaking and attenuation surrounding the low water phase of the tide, the wave heights within the estuary become periodic with the M2 tidal cycle. This periodicity starts at longitude -81.24 and becomes more narrowly distributed on the high water phase of the tide as the eastward estuarine boundary is approached.

The modeled wave energy spectral density within the estuary is also shown in Figure 2.7, plotted over the same frequency range as our observations. Comparison to the observed spectral density in Figure 2.3 shows that the simulation gives a reasonable prediction of the wave frequency and temporal characteristics. The significant wave height calculated by integrating the spectrum over the frequency band shown is compared with the measured significant wave heights in Figure 2.5 and very good visual agreement is obtained except during the highest wave heights observed just before and just after Year day 87. One reason for this discrepancy may be because higher frequency energy in the model is not included in the significant wave height calculation as the frequency cut off was 0.33 Hz. We thus conclude that the model is capable of capturing the main processes that affect wave propagation into the estuary.

The ebb shoal region surrounding the Altamaha River mouth appears to play an important role in governing wave propagation from the inner shelf to the estuary. The shoal induces depth-limited breaking (and as we will see dominates over the current-induced breaking in the inlet). The enhancement of wave breaking is directly related to the attenuation of wave energy during certain times of the tidal cycle. This breaking process causes a transfer of mean momentum from the wave motion to the ocean currents. This has implications for nearshore sediment discharge and transport.

To view the spatial characteristics of the wave height and the wave breaking index over the whole model domain and along section A over various times of the tidal cycle we assumed a constant directional spectrum taken on Year day 87.42, as shown in Figure 2.6b. For this study we neglected wind forcing in the model hence wave development within the estuary because the wind caused no significant wave height changes (wave heights increased by only 2 cm for a 10 m/s wind input). Thus we only considered the effects of changing sea level and current by the tides. Figure 2.8 shows the spatial distribution of the wave height and wave breaking index distributed over the model domain during slack low water (SLW), maximum flood, slack high water (SHW), and maximum ebb. During SLW when the water level was 1 m below mean sea level, there were no waves within the estuary and wave breaking occurred all over the ebb shoaling region. On the flood tide, with a current velocity of -1 m/s distributed evenly over the domain, the waves propagated closer to shore with breaking happening closer to shore. At SHW when the water level was 1 m above mean sea level, there was the least breaking and significant wave heights extended right to the coast and into the estuary. During the ebb tide, with a current of 1 m/s distributed evenly over the domain, the larger wave heights were translated offshore with smaller wave heights right to the inner shelf. This implies that the current also contributes to the wave characteristics but to a lesser extent than the depth.

Figure 2.9 demonstrates in detail the changes in wave height along section A for various times in the tidal cycle using observed (as shown in Figure 2.4) flood/ebb asymmetries in the estuarine current magnitude because most of this section is within the tidal channel. The greatest wave heights occurred during SHW and the lowest wave heights during SLW (a difference of approximately 1 m) with intermediate wave heights during current flows. All along section A there appeared to be a constant difference in wave heights between the ebbing and flooding tide, with greatest levels during the flood. This characteristic applies throughout the domain and is a direct result of using a constant current velocity.

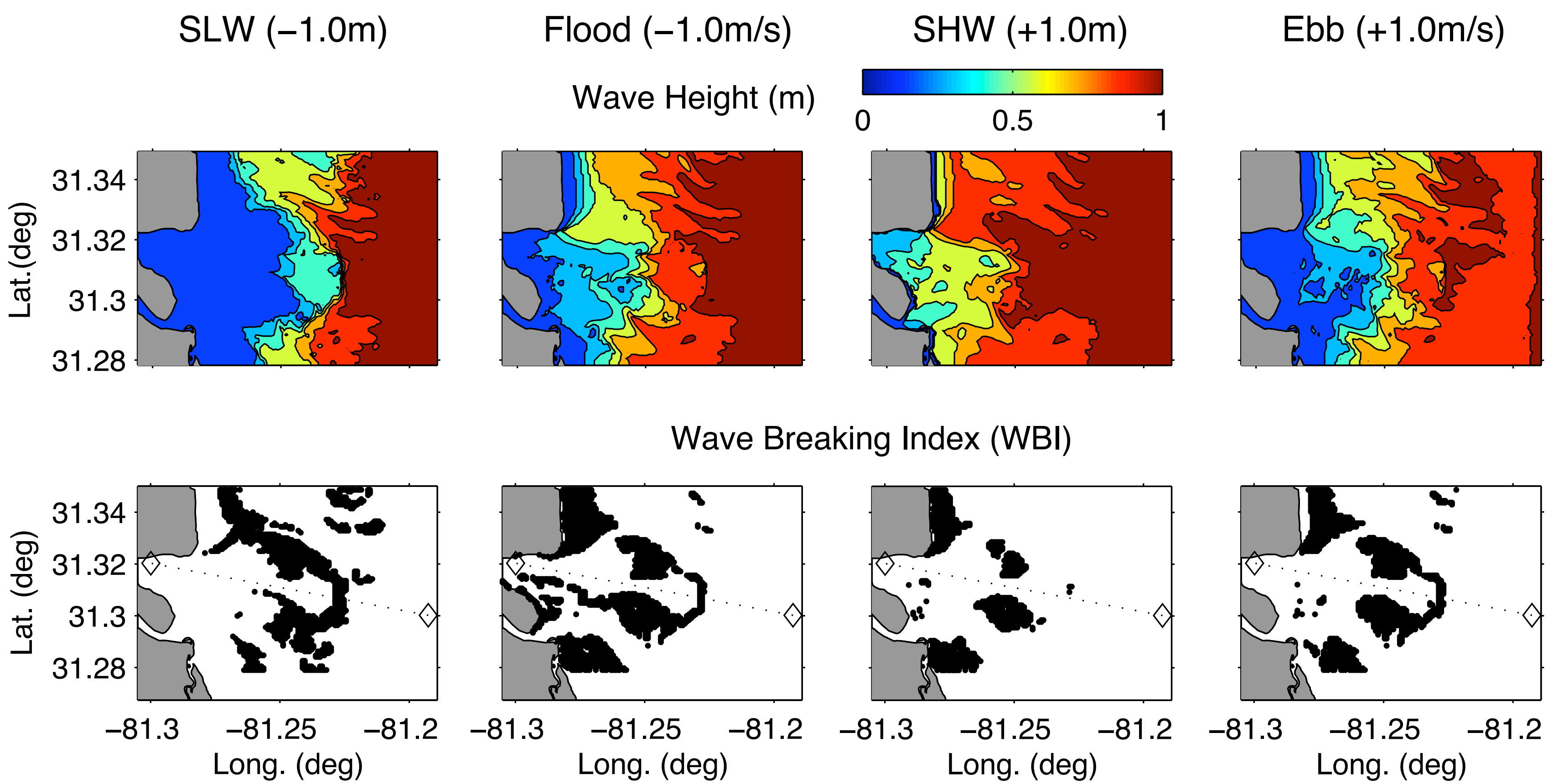

Figure 2.8: The spatial distribution of significant wave height and wave breaking index (WBI) during different phases of the tidal cycle: Slack Low Water (SLW), Flood, Slack High Water (SHW) and Ebb.

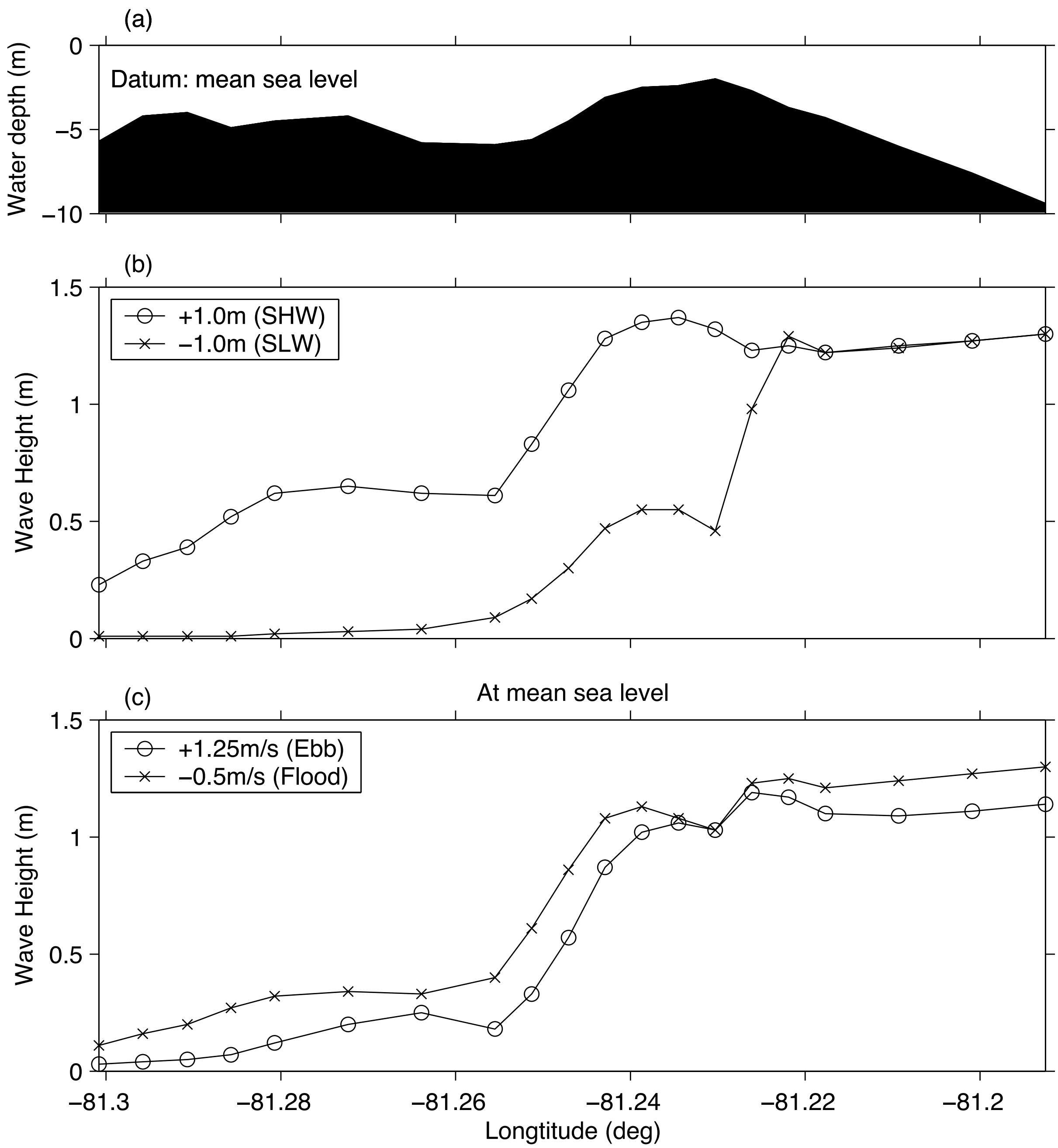

Figure 2.9: (a) Bottom bathymetry along section A. (b) Wave height changes along section A for tidal height changes when the current was slack. (c) Wave height changes along section A for tidal current changes for a constant mean sea level height.

It should be noted that even though the current affect was not the dominant factor, it is possible that the wave-current interaction effect could be over (or under) estimated in certain regions, since a uniform current field was used throughout the domain. The current structure can be altered by the bottom topography and by channel pathways. For example, in this study domain there is the shoal area outside the estuary and deeper regions within the center of the main channel.

2.5 Discussion and Conclusions

A study of sea surface wave propagation and its energy deformation was carried out using field observations and numerical experiments over a region spanning the midshelf of the South Atlantic Bight to the Altamaha River Estuary. It was found that wave heights on the shelf region correlate with the wind observations and that the wave heights were attenuated by at least 75%, possibly because of bottom friction, as they propagate from the midshelf (at 20 m depth) to the inner shelf (at 10 m depth) a distance of 15 km.

Directional observations on the inner shelf indicated that most of the wave energy is incident from the easterly direction except for occasional north- and south-easterly propagating waves. After interacting with the shoaling region of the Altamaha River, the wave energy within the estuary becomes periodic in time with greater wave energy during flood to high water phase of the tide and very low wave energy during ebb to low water. Decrease in wave height shoreward of the bar is also a result of the increase in water depth within the Altamaha River channel.

The periodic modulation of the surface wave energy inside the estuary is a direct result of enhanced depth and current-induced wave breaking that occurs at the ebb shoaling region surrounding the Altamaha River mouth at longitude 81.23°W. Modeling results with STWAVE showed that depth-induced wave breaking is significantly more important during the low water phase of the tide than current-induced wave breaking during the ebb phase of the tide. During the flood to high water phase of the tide wave energy propagates into the estuary. Temporal and modeled measurements of the significant wave height within the estuary showed a maximum wave height difference of 0.4 m between SHW and SLW. The maximum significant wave height, however almost always occurred approximately 1 h before the SHW, which means that wave height becomes maximum during the decelerating flood tide. This characteristic is also observed with the modeled results.

In this shallow water environment the wave field can alter the bottom friction felt by the mean current. From the bottom boundary layer model (BBLM) developed by Styles and Glenn (2002a) using the theoretical framework of Grant and Madsen (1979), wave-current interactions can lead to an apparent bottom roughness that is increased from typical hydraulic roughness values, leading to an enhanced bottom friction coefficient. For a flat bottom with silt (grain diameter 20 μm) the hydraulic roughness is $z_o = d/30 = 6.7 \times 10^{-5}$ cm (d is grain diameter and represents the physical roughness length) (Grant and Madsen, 1986). By including wave-current interactions associated with our observations (see Figure 2.10) there is an increase in the apparent bottom roughness up to a maximum value of $z_{o_a} \sim 8.5 \times 10^{-5}$ cm during the flooding to high water phase of the tide. It should be noted that in circulation models, these hydraulic roughness values are then added to the roughness lengths associated with the mean current frictional velocity which may be significantly greater.

Nevertheless, according to Perlin and Kit (2002), Kagan et al. (2001) and Signell and List (1997) this wave-enhanced bottom friction can have a significant damping effect on the circulation in enclosed bays (where mean currents are weak) and in coastal shorelines (where waves are large). For the Altamaha River Sound higher friction values during the latter stages of the flood tide (as the flow decreases and the waves are maximal) could potentially retard the inflow thus increasing the net river and bio-geo-chemical transport offshore. As a result, surface wave energy can be another factor that affects the small scale flow and mixing at the bottom boundary layer. Recent work by Mellor (2002), has shown that the bottom boundary layer model works well for boundary layer algorithms that invoke eddy viscosity parameterizations which do not depend on the turbulent kinetic energy. For $k - \epsilon$ and 2.5

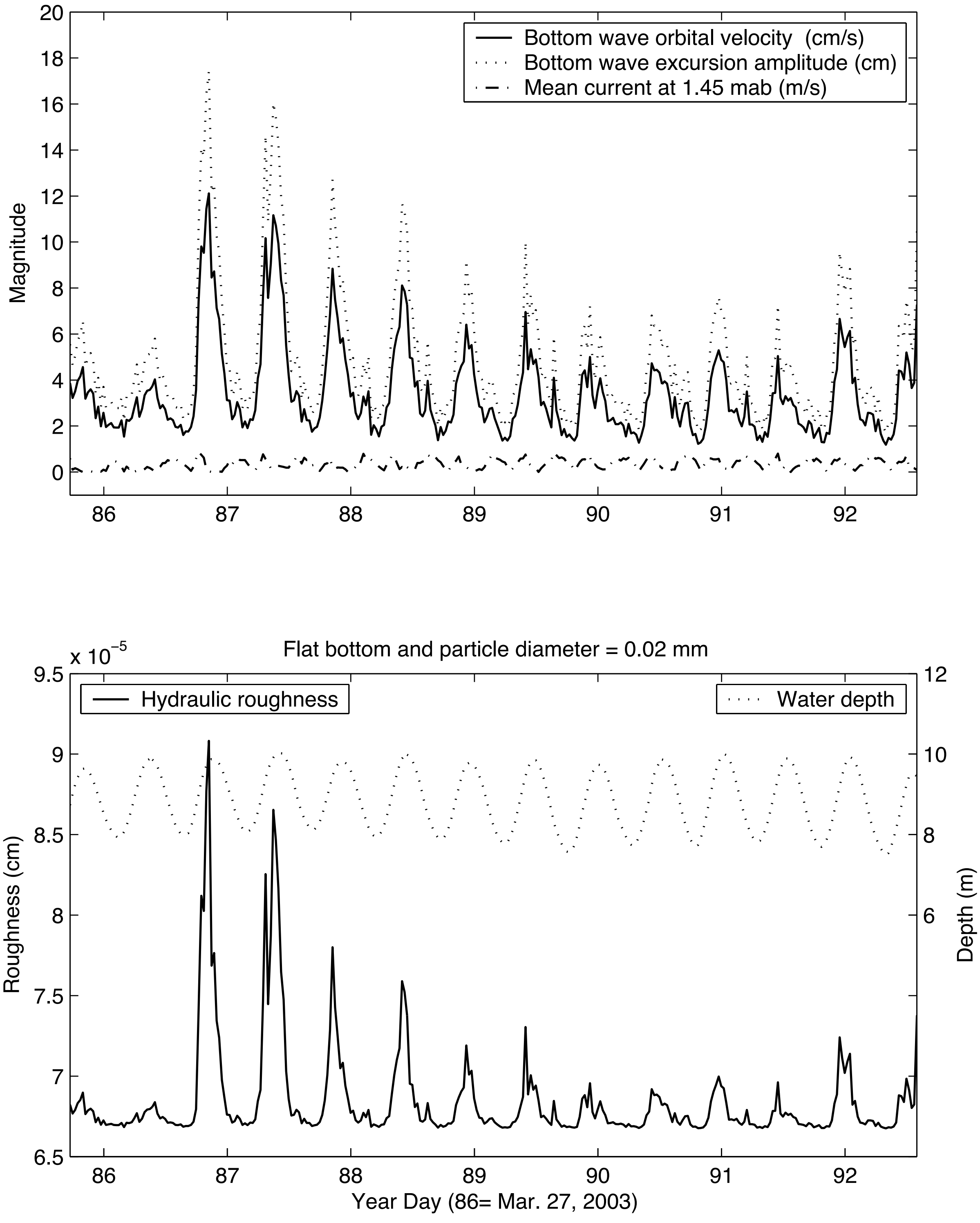

Figure 2.10: A summary of the wave and current parameters as measured 1.45 meters above bottom. The apparent hydraulic roughness as a function of time compared with the tidal cycle.

closure type models Mellor (2002) developed a parameterization for the waves which is in the form of an apparent production of TKE that adds to the shear production of the mean current.

Acknowledgments. This work was supported by the NSF (OCE-9982133) as part of the Georgia Coastal Ecosystems Long Term Ecological Research (GCE-LTER) project (http://gce-lter.marsci.uga.edu/lter/index.htm) and by the University of Georgia Research Foundation, Faculty Research Grant program. Special thanks go to Dr. Jane M. Smith of the U.S. Army Engineer Research and Development Center for providing the STWAVE source code and for help on model runs. The authors would like to thank Captain Raymond Sweatte and the crew of the R/V Savannah for their enthusiastic support in instrument deployment and recovery.

Chapter 3

VARIATION OF TURBULENT FLOW WITH RIVER DISCHARGE IN THE ALTAMAHA RIVER ESTUARY, GEORGIA[1]

[1]Ki Ryong Kang, Daniela Di Iorio. To be submitted for publication in *Journal of Geophysical Research*

Abstract

Turbulent flow characteristics under two significantly different river discharge (minimum and maximum) periods were studied in the Altamaha River Estuary, GA using a variety of moored instrumentation, combined with detailed water column profiling from an anchored vessel. Estimates of the Reynolds stress, shear production (P), dissipation rate (ϵ) and buoyancy flux (B) were derived and compared for the two contrasting river conditions which essentially characterized the estuary as well mixed during low discharge and partially mixed during high discharge. Wave effects were removed from the measurement of turbulent kinetic energy (TKE) using a linear filtration method and then a $-5/3$ slope was fit for an indirect measurement of ϵ. We suggest two possible mechanisms for the observed flood/ebb asymmetries in the shear production of energy: wave-induced bottom roughness change and the competing effects of the barotropic and baroclinic pressure gradients. Flood/ebb asymmetries in the buoyancy flux, calculated by the dynamic approach in which the flux is estimated as a residual after other terms in the simplified density conservation equation are measured, showed that during ebb the buoyancy flux was more of a sink than during flood where it was a weak source. A balance of production and dissipation of energy was not obtained, giving at most a factor of 2 difference implying that turbulent transport of TKE is a consideration. A one-dimensional turbulence modeling experiment obtained several turbulent parameters during a low river discharge period but could not reproduce flood tide magnitudes. For the high river discharge period the phasing of the mean and turbulent flow characteristics during flood could not be reproduced. Nevertheless depth dependent predictions revealed details of the bottom boundary layer height and strength of turbulence above the bottom boundary layer during times of strong stratification.

Keywords: boundary layer flow, turbulent kinetic energy, Altamaha River Estuary, Georgia

3.1 Introduction

Turbulence is responsible for mixing water mass properties and for transferring momentum between spatial scales because of its irregular, random, highly dissipative, continuous, and three dimensional flow characteristics (Tennekes and Lumley, 1999; Salmon, 1998). The water motion near the bed affects the movement of sediments including deposition and suspension, and the distribution of chemical, biological and physical properties that are related to water quality (Gonzalez, 1984; Green et al., 1990; Trowbridge and Madsen, 1984a,b). Spatial scales of turbulence range from the dissipative microscales to the energy containing scales of a few meters. Because of the small-scale motion and intermittent spatial and temporal characteristics, it has been difficult to measure directly the three-dimensional properties of turbulent flow in the ocean even though many researchers have tried to do so since the 1950s (Nihoul, 1977). With recently developed high frequency acoustic techniques it has become possible to measure many turbulent quantities within the bottom boundary layer and water column of estuarine and coastal environments (see for example Simpson et al., 2005; Lueck et al., 1997; Voulgaris and Trowbridge, 1997; Trowbridge et al., 1999; Lu and Lueck, 1999a,b; Wahl, 2000; Rippeth et al., 2001; Stacey, 1999; Stacey et al., 1999; Shaw et al., 2001).

Some of the factors affecting turbulence in the bottom boundary layer are the bed drag characteristics, velocity shear and density gradients. In shallow areas, wind generated surface wave motions can reach the bottom, with greater attenuation as depth increases, and affect the measurement of turbulent flow variability in terms of bottom stress (Styles and Glenn, 2002a; Trowbridge and Madsen, 1984a,b). Very near the bottom the waves produce a very thin wave boundary layer in which the flow is turbulent and can affect the mean current boundary layer. Because of nonlinear interactions between wave and turbulence and their overlapping scales, it is difficult to completely separate wave and turbulent motions in observations of velocity data. However, if we assume that the wave and turbulence are linearly combined, the spectral separation method (Agrawal and Aubrey, 1992; Wolf, 1999) can be applied to wave-contaminated velocity data together with information from bottom mounted pressure spectra. This linear filtration method uses the coherence spectra between pressure and flow data, and was originally derived by Bendat and Piersol (1971). Over the frequency band where the motions overlap the pressure fluctuations due to surface undulations, the coherence will be high.

Stratification and velocity shear are important competitors in estuarine dynamics because when a density gradient exists it resists the momentum exchange by turbulence so more shear is needed to keep the momentum exchange happening (Dyer, 1997). It is very useful to quantify the ratio between the stabilizing force of density stratification ($\partial\rho/\partial z$) and destabilizing influence of the velocity shear ($\partial U/\partial z$, $\partial V/\partial z$) in order to check whether or not the turbulent flow is stable. The gradient Richardson number, Ri_g is defined by

$$\mathrm{Ri}_g = \frac{N^2}{(dU/dz)^2 + (dV/dz)^2}, \tag{3.1}$$

where $N^2 = -(\frac{g}{\rho})\frac{d\rho}{dz}$ is the Brunt-Väisälä frequency and is a measure of stratification, U and V are the along (x) and cross channel (y) velocity components, and z is the vertical with positive upward. The formation and growth of the instability of stratified fluid was studied by Miles (1961, 1963) and Miles and Howard (1964), and the criteria for instability is still used because it is very simple and readily applicable: "*the sufficient condition for an inviscid continuously stratified flow to be stable to small disturbance is that $Ri_g > 0.25$ everywhere in the flow*". When $\mathrm{Ri}_g < 0.25$ (generally called Kelvin-Helmholtz instabilities), the velocity shear rapidly steepens the wave motion between layers, and eventually leads to mixing of water from above and below a layer.

The estuarine system of the Georgia coast is characterized by a series of barrier islands and extensive salt marsh complexes (see Figure 3.1). As an important source of fresh water input to Georgia coastal water, the Altamaha River has a monthly median discharge of 250 m^3/s with peak discharge during very early spring (Alber and Sheldon, 1999). With the annual difference between maximum and minimum river discharge over 1500 m^3/s, turbulent mixing processes take place actively in this estuary. The main estuarine flow here is driven by fresh water discharge, tidal-, wind- and to a lesser extend wave-induced flow. The depth

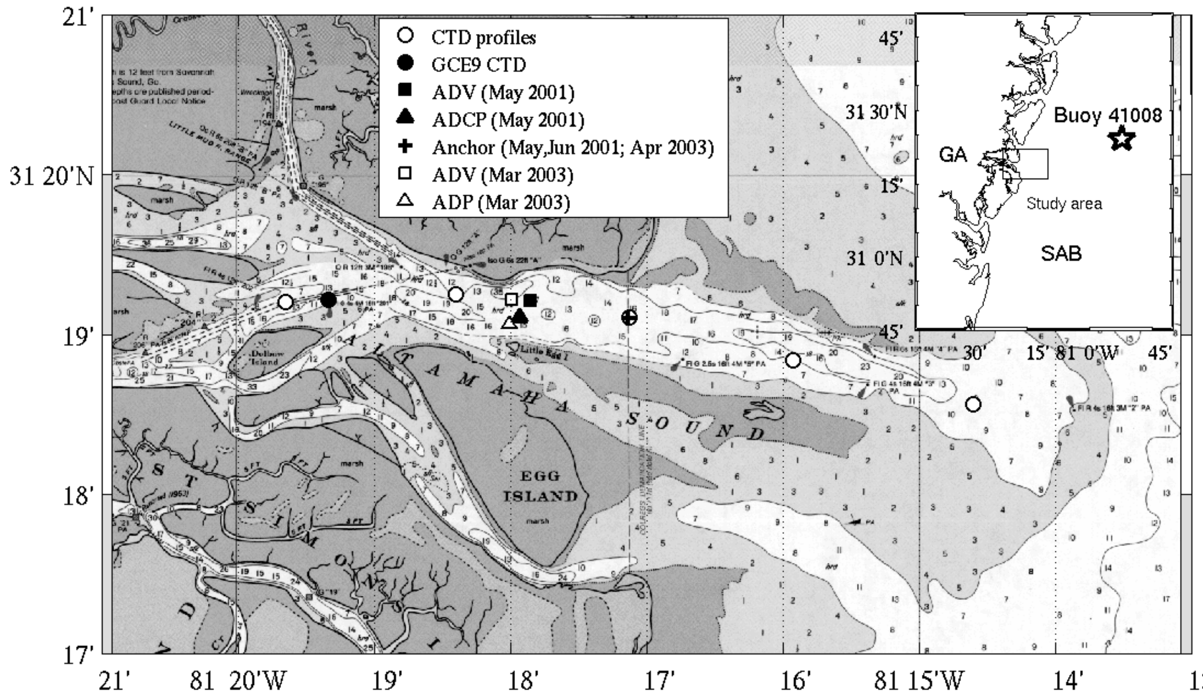

Figure 3.1: Georgia coastal study area showing deployed instrumentation on a hydrographic chart of the Altamaha River Sound. Bathymetry is in feet relative to mean lowest low water. Profiles of conductivity-temperature-depth (CTD) were carried out at stations [-4, -2, 0, 2, 4]km during one low and one high water transect, and long term monitoring of the water properties is carried out at GCE9 of the GCE-LTER project.

and width of the main channel connecting the Altamaha River to the coastal ocean are approximately 7 m and 1 km respectively (see Figure 3.1). One interesting bottom feature is that a bar surrounds the mouth of the estuary which inhibits surface wave energy from propagating into the estuary during ebb and low water periods (Kang and DiIorio, 2004).

Turbulent mixing and turbulent flow characteristics are essential factors in understanding the hydrodynamics of estuaries and in modeling the interaction between intertidal and nearshore systems so our focus is on the effect of changing river discharge on the characteristics of the turbulent kinetic energy. Many observational and numerical studies have been carried out in coastal regions and in partially stratified estuaries (see for example Trowbridge et al., 1999; Lu et al., 2000; Peters and Bokhorst, 2000; Burchard et al., 1998; Gaspar et al., 1990). Seim et al. (2002) measured the Reynolds stress in a sinuous bend of the Satilla River and found asymmetries related to curvature with magnitudes following the spring-neap tidal cycle. Prior to our study, an examination of turbulent flow characteristics in this area has not been carried out even though turbulence in estuarine and coastal regions is a key component to understanding many physical, biological and biogeochemical processes and for the development of circulation models.

The observational program, study area and the physical environment in terms of salinity and flow variations are described in section 3.2. The Reynolds stress and TKE variations corrected for waves are introduced in section 3.3 along with a measure of the shear and buoyant production and molecular dissipation. One-dimensional turbulent model experiments are introduced in section 3.4. In this section we examine if a 1-dimensional turbulent model can simulate several turbulent flow parameters such as the Reynolds stress, TKE and dissipation rate using only depth averaged velocity, surface and bottom temperature and salinity, and along channel density gradients. Finally, section 3.5 summarizes the turbulent flow characteristics with implications to bottom boundary layer dynamics.

3.2 Observational Program

The field experiment for studying the characteristics of turbulent flow as a function of river discharge in the Altamaha River estuary was carried out over a neap/spring tidal cycle from May 29 to Jun 6, 2001 and from March 25 to April 2, 2003. The experiments were designed specifically to observe changes in bottom turbulent flow and water column stability structure within the estuary during two different stratification regimes in the estuary. The May 2001 experiment was during a low river discharge period and the March 2003 experiment was during the maximum river discharge for the year. Figure 3.1 shows a hydrographic chart of the study area in relation to the Georgia coast and South Atlantic Bight (SAB) together with deployed instrumentation, and Figure 3.2 shows annual variations of the river discharge for 2001 and 2003. Observations were also supplemented with meteorological data collected from the NOAA NDBC buoy in Gray's Reef National Marine Sanctuary 30 km offshore Sapelo Island, GA.

3.2.1 Instrumentation

The first observation period occurred during the May 2001 Georgia Coastal Ecosystems - Long Term Ecological Research (GCE-LTER) survey cruise when the river discharge was low (200 $m^3\ s^{-1}$). Figure 3.1 shows the instrumentation deployed and station locations within Altamaha Sound. An RDI 600 kHz Workhorse acoustic Doppler current profiler (ADCP) and a SonTek 5 MHz acoustic Doppler velocimeter (ADV) were deployed over a spring/neap cycle in the center of the channel at 6.5 m depth. The ADV mooring also consisted of surface and bottom SeaBird Microcat conductivity-temperature-depth (CTD) meters sampling at 6 min intervals. Current velocity profiles by the ADCP were also sampled every 6 min with 0.5 m bin depths with the first sample at 1.5 meter above bottom (mab). The ADV was programmed in burst sampling mode in order to observe the bottom boundary layer mean and turbulent flow characteristics and the wave properties at 1.4 mab. Burst sampling was carried out every 30 min with three bursts: 0.1 Hz for 5.3 min, then 4 Hz for 17 min, and

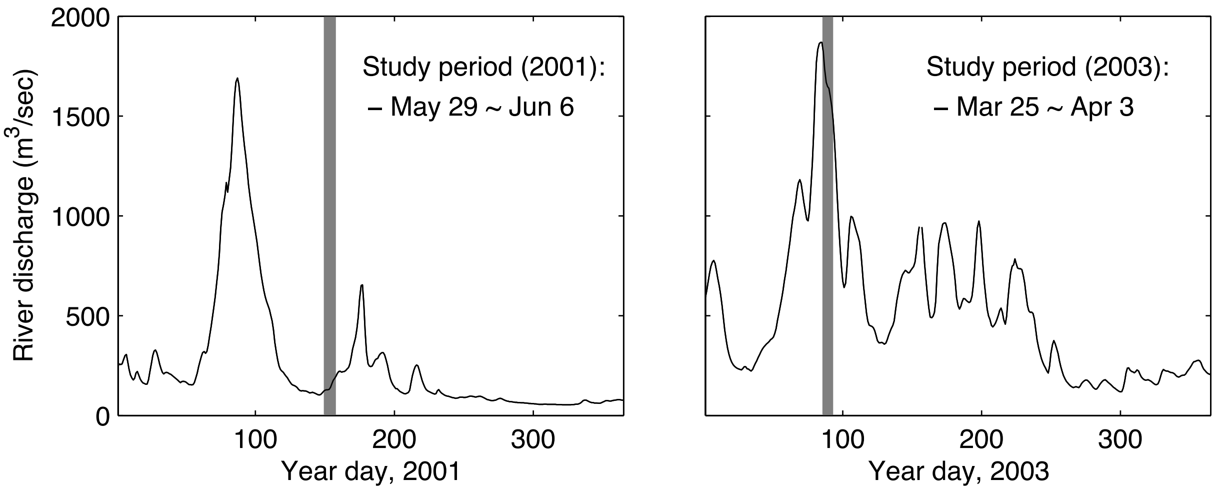

Figure 3.2: Altamaha River discharge in 2001 (left) and 2003 (right) with highlighted zone corresponding to our measurement program.

then 25 Hz for 5.5 min. The sampling of wave energy entering the estuary was designed to quantify their effects on the bottom turbulent flow. The research vessel *RV Savannah* was anchored close to the moorings, at the 'colregs demarcation line' which is also defined as the 0 km CTD profile station. Two (one spring and one neap) 13-hour time series of CTD profiles were taken every 30 min. Finally ship transects were carried out along the channel for CTD profiles during one low and one high water period starting 2 h prior to slack water.

The second observation period was during the March 2003 GCE-LTER survey cruise when the river discharge was almost ten times larger than in 2001 (1800 m^3 s^{-1} as shown in 3.2). The moored instruments consisted of a 4-beam SonTek 3 MHz acoustic Doppler profiler (ADP) and the velocimeter (ADV) together with surface and bottom CTDs deployed in the same configuration as the first experiment (see Figure 3.1). The ADP was set to sample with 0.2 m bin size every 5 min with the CTDs having the same 5 min sampling interval. The ADP was also programmed in beam coordinate mode, but due to the low signal to noise ratio, the turbulent beam velocity variances could not be resolved. In addition, the *RV Savannah* was anchored in the channel for one 13-hour survey of CTD profiles every 30 min and ship transects were carried out along the channel for a low and high water survey. In 2002 the GCE-LTER project had established its long term monitoring network of CTDs along the Altamaha River and its permanent station is identified as the GCE9 CTD marker in Figure 3.1. Both these observation campaigns produced good quality data that were used to quantify some turbulent bottom boundary layer characteristics as a function of tidal phase and stratification.

3.2.2 The Altamaha River Estuary

The Altamaha River estuary, because of its shallow depth (< 10 m) and strong tides (~ 1 m/s flows), can be classified as ranging from a well mixed to a partially mixed regime depending on the river discharge and its seasonal variation (100-1800 m^3/s). The input of fresh water in estuaries contributes to an increase of vertical and horizontal density gradients and sea surface slopes. These characteristics cause both barotropic and baroclinic forcing, resulting in the classic estuarine exchange circulation where fresh water flows out on top and oceanic water flows in at depth. Mixing processes in estuaries are driven mainly by tide and wind forcing and the interaction of the longitudinal density gradient with the vertical current shear leads to strained induced periodic stratification (SIPS) (Simpson et al., 1990) termed "tidal straining". This periodic forcing induces periodic stratification with the semi-diurnal tide, as will be discussed.

Figure 3.3 summarizes the mean atmospheric and oceanic forcing for both of our observational programs. For 2001 the winds were fairly steady ranging in magnitude between 5 and 10 m/s. They blew predominantly from the southerly direction creating upwelling-favorable conditions that can promote exchange between the estuary and the coastal waters. For 2003 the winds were much more variable with a strong wind burst approaching 15 m/s from the northwesterly direction.

The salinity underwent rapid and large changes over the tidal cycle throughout the water column with maximum values during the HW phase of the tide and greater salinity near the bottom. The bottom MicroCat conductivity was fouled toward the end of the 2001 deployment. The salinity difference between surface and bottom during May 2001 started to increase after high tide becoming maximal during the ebb tide which is consistent with the SIPS process. During the flood to high water phase, the salinity difference was close to 0 except on a few occasions when the salinity difference approached a local maximum (see for example day 153, 154 and 155 close to midnight). This has implications for stability as will be discussed. During neap tide on Year day 149 the salinity difference was greatest and as the spring tide approached on Year Day 156, the differences appear to diminish presumably due to more energetic mixing. March 2003 showed entirely different characteristics due to the high freshwater discharge. During the time surrounding low water the entire water column was fresh and during the time surrounding high water strong stratification existed. Right at

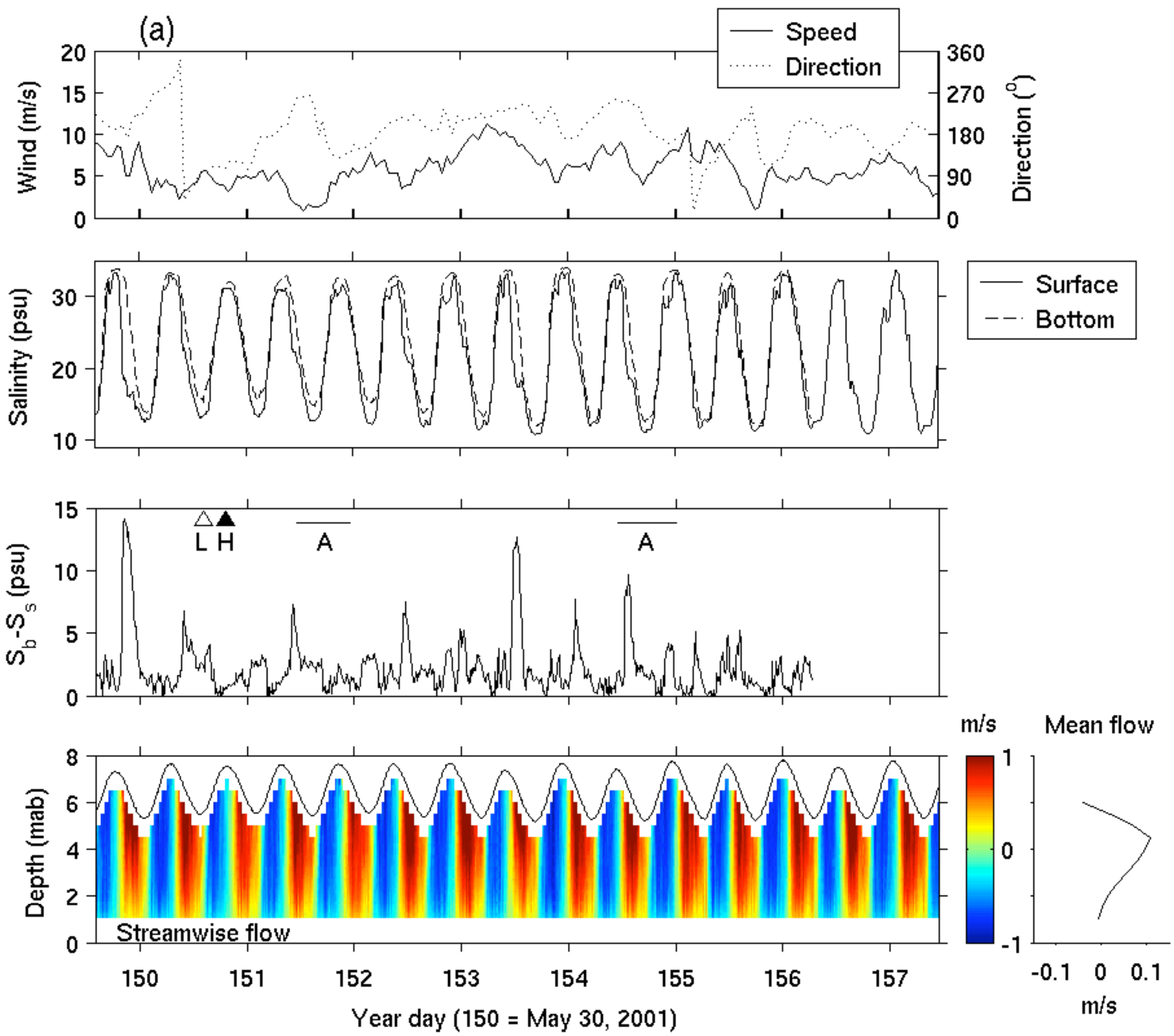

Figure 3.3: Wind speed and direction, surface and bottom salinities and their differences together with the along-channel flow ($107.1^{o}T$) during a) low river discharge of May 2001 and b) high river discharge of Mar 2003. Times for low (L) and high (H) water ship transects and anchor (A) time series are also shown.

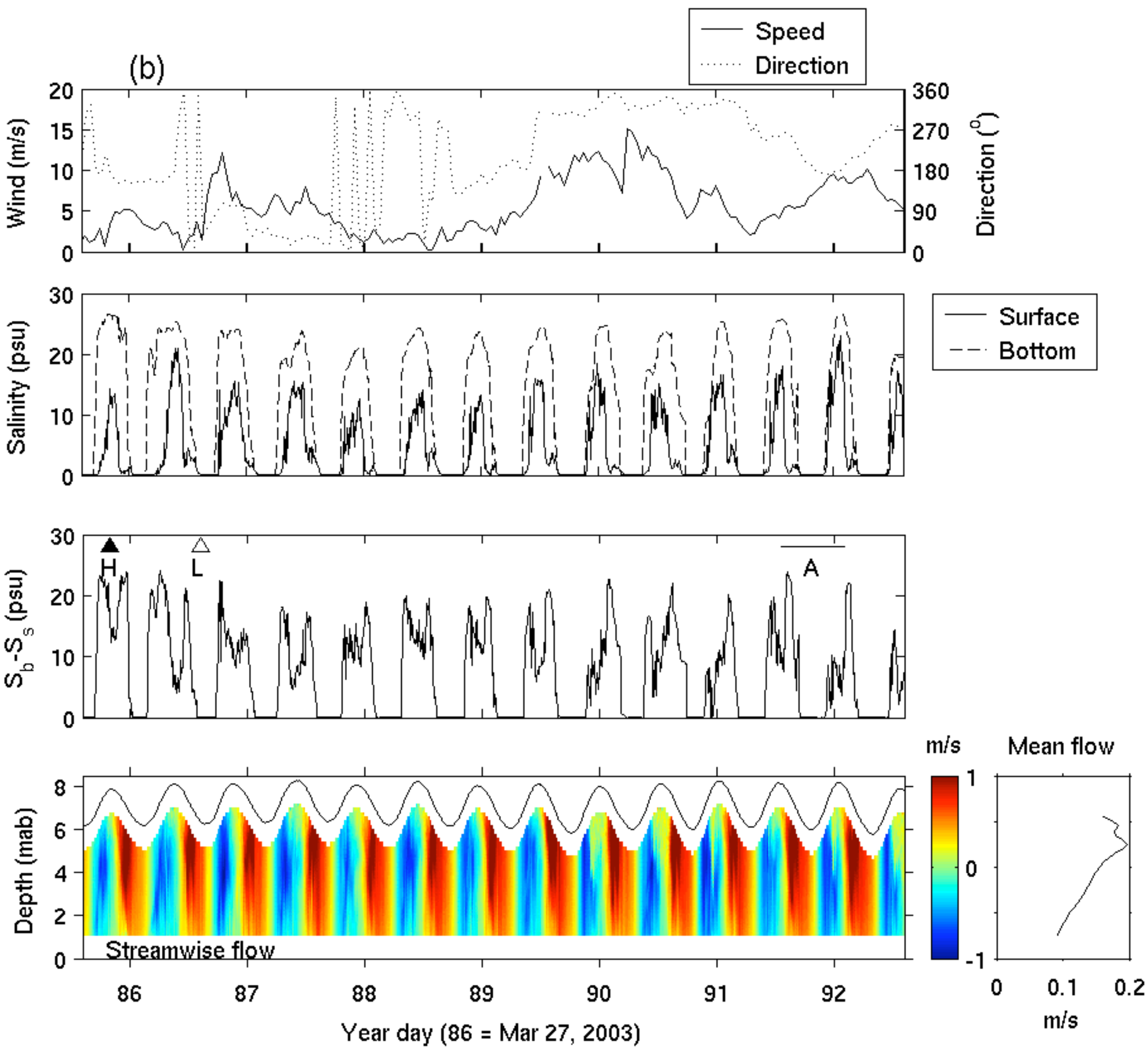

Figure 3.3 continued.

slack high water for a brief period of time the salinity difference showed a local minimum corresponding to more oceanic conditions throughout the water column.

Figure 3.4 shows the salinity structure along the Altamaha Sound channel carried out during times denoted by the open (low water) and closed (high water) triangles in Figure 3.3. Deployed instruments were located at the 1 km mark and the anchor station at 0 km, In May 2001 well mixed conditions occurred at the end of the flood tide and fresher and weakly stratified conditions at the end of the ebb tide. In Mar 2003 strong stratification occurred during high water with fresh conditions during low water. Highly stratified water at slack low water occurs further downstream away from our time series measurements. Based on the sectional salinity distribution along the channel, the tidal excursion distance for this time was only 4 km whereas it was greater than 8 km in 2001.

The along-channel flow was characterized by strong tidal oscillations dominated by the semi-diurnal principal lunar tide (M2). The tidal range was at least 2 m and maximum flow speeds observed exceeded 1 m/s during the ebb tide and order of -1 m/s during flood (cross-channel flows were typically less than 0.1 m/s and therefore not shown). In May 2001 the tidally averaged flow showed a net residual flow of 0.1 m/s out of the estuary at 4.5 mab and no net inflow at depth. The March 2003 flow showed that the high flow rate of the river essentially holds back the advancing tide. Also the flood tide near the surface was retarded prior to slack high water which is attributed to the westerly wind forcing event on year days 90-91. The net residual flow was much stronger throughout the water column with flows approaching 0.2 m/s in the surface layer.

More detailed analysis of the temporally varying stratification and shear is described in Figure 3.5. Stratification, along channel flow speeds and the resulting water column stability computed using the gradient Richardson number (3.1) are shown over the 13 h anchor time series in Year 2001 on day 151 (close to neap) and 154 (close to spring) and in Year 2003 on Day 91 (spring tide). The results for 2001 show some differences that may be associated with neap and spring tides. A few days after the neap tide the density was well mixed until slack

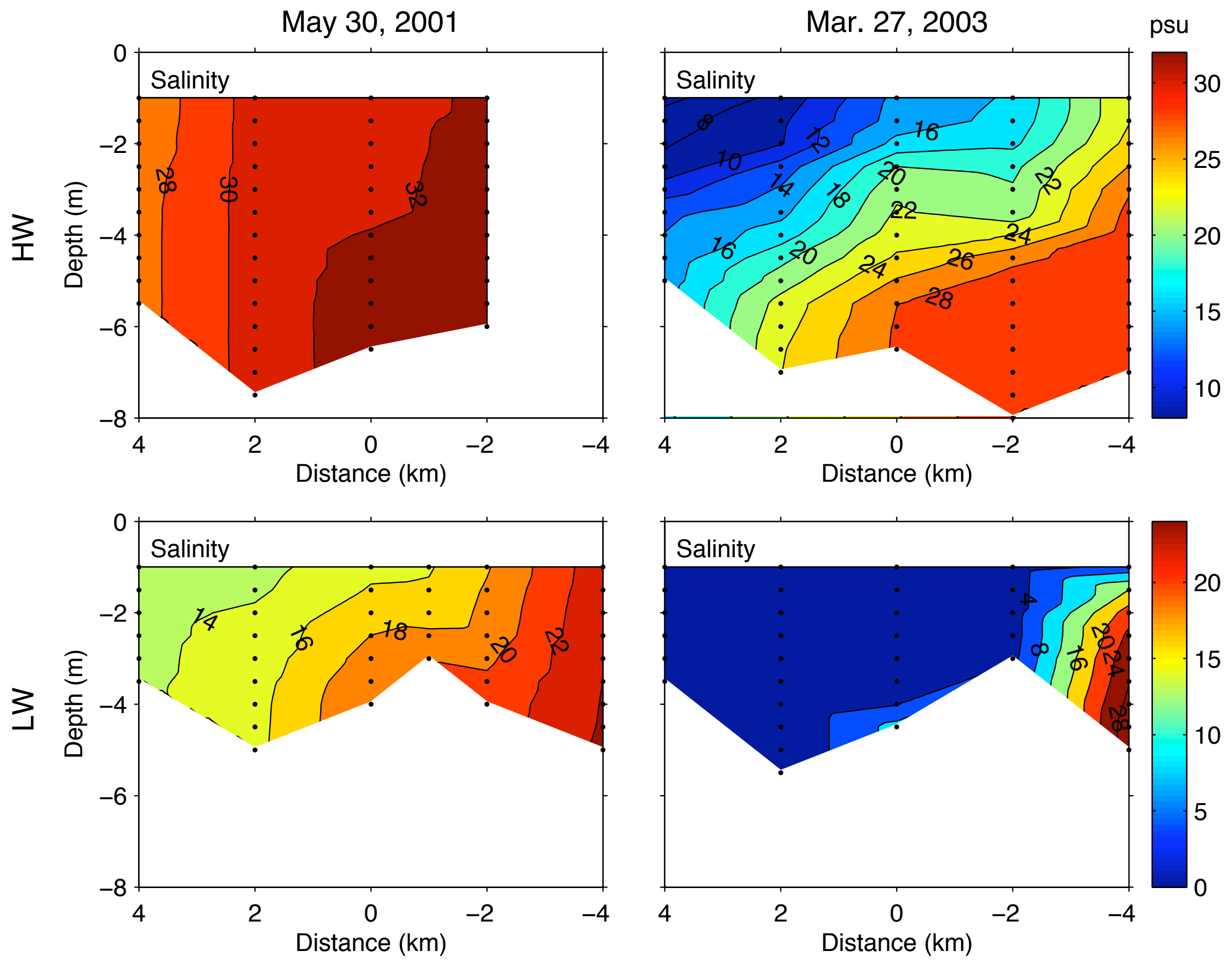

Figure 3.4: Salinity along the Altamaha River during high and low water for the low river discharge period (May 2001) and high river discharge period (Mar 2003).

low water when there was weak stratification which was then quickly mixed by the flooding tide. At the end of the flood tide, weak stratification started to increase and persisted until shortly after the following ebb tide. The current shear during this time was fairly weak and thus the gradient Richardson number shows stable conditions ($\mathrm{Ri}_g > 0.25$) wherever there was some stratification. That is, the shear cannot overcome the stabilizing effects of stratification. The spring tide event showed much stronger shear conditions and similar stratification through the tidal cycle. The gradient Richardson number, however showed that the water column was more easily mixed by the destabilizing shear effects ($\mathrm{Ri}_g < 0.25$). In both these studies the flow during ebb was more uniformly sheared throughout the water column whereas during flood the shear was concentrated near the bottom. According to Jay (1991), this can be due to the superposition of baroclinic and barotropic flows.

For 2003 the stratification on the ebb tide persisted longer than during the flood because the seaward ebbing flow was strengthened throughout the water column and the landward flood tide was shortened. The high river discharge together with wind forcing created a sheared flow during the end of the flooding tide as the surface waters were retarded before the deeper waters. As a result of the strong stable stratification the Richardson number showed very stable water column conditions during the ebb and flood tide only at the pycnocline depth.

3.3 Turbulent Kinetic Energy

In sheared flow, a simplified form for the equation of turbulent kinetic energy per unit mass, $E = 1/2(\overline{u'^2} + \overline{v'^2} + \overline{w'^2})$ is,

$$-\frac{\partial E}{\partial t} - \overline{u'w'}\frac{\partial U}{\partial z} - \overline{v'w'}\frac{\partial V}{\partial z} = \frac{g}{\rho_o}\overline{\rho' w'} + \epsilon \tag{3.2}$$

(Tennekes and Lumley, 1999), where z is the vertical direction, $\mathbf{U} = (U(z), V(z), 0)$ is the mean flow, $\mathbf{u'} = (u', v', w')$ is the turbulent velocity vector, ρ_o is a mean reference density, ρ' is the turbulent density fluctuation, g is the gravitational acceleration and the overbar

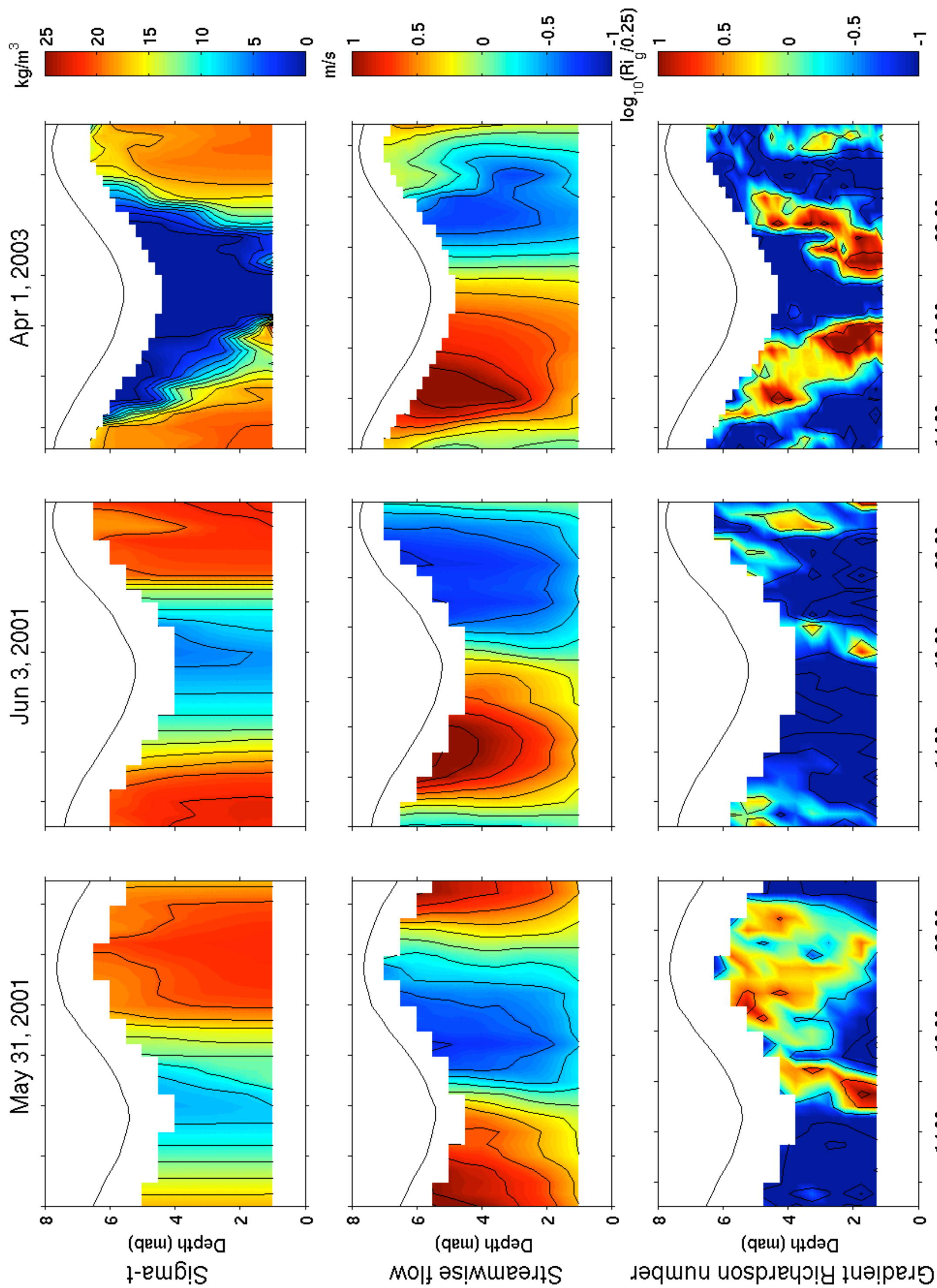

Figure 3.5: One tidal cycle (13 h time series) of stratification, along channel flow (107.1^o from North), and the gradient Richardson number on May 31,2001 (close to Neap), Jun.3,2001 (close to Spring), and Apr.1, 2003 (on Spring).

represents a time average. The terms on the right-hand side represent losses of E: the first term is the vertical buoyancy flux associated with work against gravity in a stable stratified fluid and the second term ϵ represents the loss of energy to heat by molecular viscosity. The terms on the left-hand side represent rate of change of E and the production of E by interaction of the mean shear with the Reynolds stresses $-\overline{u'w'}$ and $-\overline{v'w'}$, which are the vertical fluxes of horizontal momentum.

The vertical buoyancy flux can be estimated following the method of Simpson et al. (2005), from the conservation of mass equation,

$$\frac{\partial \rho}{\partial t} + U\frac{\partial \rho}{\partial x} = -\frac{\partial \overline{\rho' w'}}{\partial z} \tag{3.3}$$

where $\rho(x, z, t)$ is the density independent of the channel cross-section and the horizontal buoyancy flux terms $-\partial\overline{u'\rho'}/\partial x$ and $-\partial\overline{v'\rho'}/\partial y$ are assumed negligible. In the following sections we attempt to quantify the various terms represented in these equations, in order to understand the cycle of turbulent energy for the different river discharge regimes and hence stratification.

3.3.1 Reynolds Stresses

Direct calculations of the along and cross channel Reynolds stresses $-\overline{u'w'}$ and $-\overline{v'w'}$ respectively were calculated from the ADV's 25 Hz sampled data over 5.5 min every 30 min. Since Voulgaris and Trowbridge (1997)'s evaluation of the ADV for turbulent flow measurements, this instrument has been widely used for point measurements of turbulent flow characteristics (see for example Trowbridge et al., 1999; Trowbridge and Elgar, 2001; Shaw and Trowbridge, 2001; Simpson et al., 2005). Turbulent velocity data were logged relative to an Earth coordinate system (positive for East/North/Up) and therefore corrected for heading, pitch and roll. Pitch and roll, for all the data, both remained less than 3.5^o settling into a tilt less than 2^o after 2 days. Some spikes associated with instrument noise were removed, the mean flow was removed by linear detrending, and the data were then rotated from the earth coordinate system to one aligned with the channel direction. The correlation between the along-channel

(107.1^oT) and vertical velocity components ($-\overline{u'w'}$), and the cross-channel (17.1^oT) and vertical velocity components ($-\overline{v'w'}$) were then computed.

Figure 3.6 shows time series of the Reynolds stress and the mean flow for each burst taken at 1.4 mab together with the corresponding significant wave height for the May 2001 and March 2003 observational periods. The temporal variation of the Reynolds stress followed the tidal cycle with positive values corresponding to positive (ebb) flow and negative values corresponding to negative (flood) flow with zero values corresponding to slack water. The observed stress ranged in value from -2.0 to $\sim 1.0 \times 10^{-3}\mathrm{m}^2\mathrm{s}^{-2}$ for 2001 and -2.0 to $\sim 6.0 \times 10^{-3}\mathrm{m}^2\mathrm{s}^{-2}$ for 2003. The cross-channel stress was significantly less and was negligible compared to the along-channel stress for 2001, but in 2003 the cross-stream stress became more significant during the ebb tide.

One interesting observation of the May 2001 data is that the magnitude of the Reynolds stress for flood tide was relatively higher and more erratic than those for ebb tide even though the mean tidal flow was slightly ebb-dominated. This implies that there were asymmetries in the forcing mechanisms that contributed to this measurement or to the vertical momentum exchange. According to Kang and DiIorio (2004), wave energy propagating approximately in the along-channel direction of Altamaha Sound existed primarily during flood to high water phase of the tide with maximum wave heights approximately 2 h before slack high water as shown in Figure 3.6; little to no wave energy exists from ebb to slack low water because of enhanced wave breaking due to the ebb shoaling effects at the mouth of the Altamaha River where islands and submerged sandbars surround the river channel.

In this shallow environment the wave field can alter the bottom friction felt by the current as the spatial scales of stress carrying turbulence overlap the spatial scales of the wave-induced orbital velocities. From the bottom boundary layer model (BBLM) developed by Styles and Glenn (2002a) using the theoretical framework of Grant and Madsen (1979), wave-current interactions can lead to an apparent bottom roughness that is increased from typical hydraulic roughness values as discussed in Kang and DiIorio (2004), leading to an

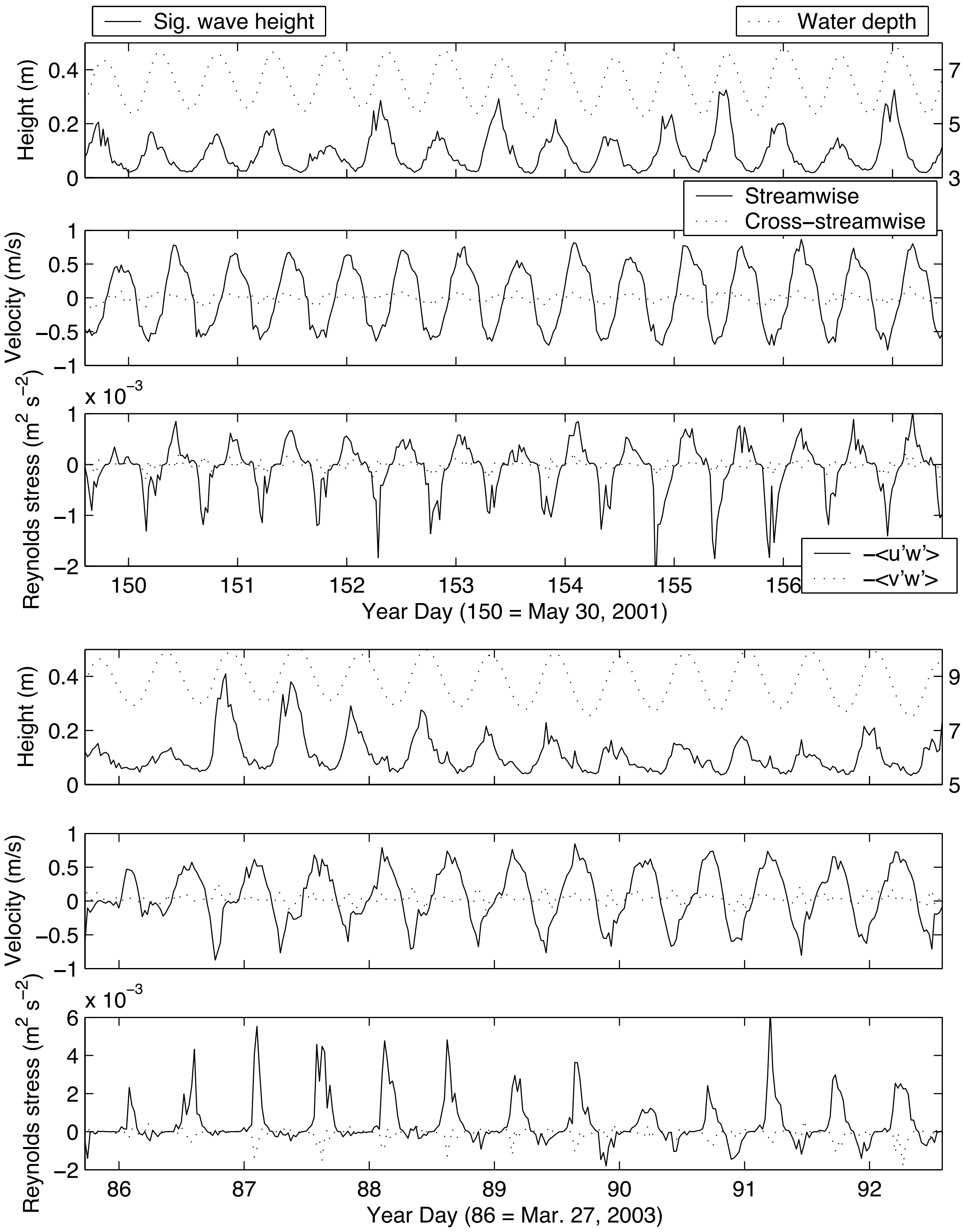

Figure 3.6: The significant wave heights in Altamaha Sound together with along and cross channel flows and Reynolds stresses observed at 1.4 mab for May 2001 (upper) and March 2003 (lower) experimental periods.

enhanced bottom friction coefficient. According to Mellor (1975) the effects of the wave field on the mean current flow are felt through an increase in stress, which is due to an increase in turbulent kinetic energy, which in turn is due to an increase in shear production. As a result, he developed a procedure to parameterize the effects of oscillatory flow on the mean current in numerical models by adding an apparent production term.

Another mechanism for asymmetry of the Reynolds stress may be due to the asymmetry in pressure gradients. The barotropic pressure gradient term is associated with horizontal changes in surface elevation and is produced by several mechanisms. First, the propagating tidal wave creates temporal variations in the water surface elevation and secondly, a freshwater river outflow creates a barotropic pressure gradient in the seaward direction. These processes can be approximated as (neglecting any barotropic response to the baroclinic effect),

$$\frac{-1}{\rho_o}\frac{\partial P_{bt}}{\partial x} = \frac{2\pi U}{T_{M2}}\cos\left(\frac{2\pi t}{T_{M2}}\right) + g\frac{\Delta H}{\Delta x}, \tag{3.4}$$

where T_{M2} is the period of the M2 tidal constituent and $\Delta H/\Delta x$ is the sea surface slope caused by the difference in river gauge heights. The baroclinic pressure gradient can be approximated as,

$$\frac{-1}{\rho_o}\frac{\partial P_{bc}}{\partial x} = \frac{g}{\rho_o}\frac{\partial \rho_o}{\partial x}(z-h), \tag{3.5}$$

where $z = 0$ at the bottom and h is the depth. Thus the baroclinic and barotropic pressure gradients were in the same direction during the flood flow (i.e. upstream) for 2001 when the river gauge height produced a negligible barotropic forcing downstream. During ebb flow the barotropic tidal and baroclinic pressure gradients were in opposite directions, thus creating a smaller stress during ebb.

For 2003 the river gauge height adds an important and strong barotropic forcing seaward, as the current showed a strong ebb-dominant flow, which can diminish the effect of barotropic tidal forcing and baroclinic forcing landward during flood thus reducing the stresses. The ebb flow then adds the river and tidal barotropic pressure gradients thus creating large stresses. This is consistent with the 2003 observations showing that the stress during flood is practically negligible. The start of the measurement was just after neap tide and from day 85 to 88 the river current was strong enough to resist the tidal current in the near bottom. At the onset of spring tide, the flood flow became strengthened and the stress increased.

3.3.2 Energy Spectra - TKE and Dissipation

The estimate of the turbulent kinetic energy and its dissipation rate required a method to remove wave-induced orbital motions. It is difficult to completely separate wave-induced and turbulent motion because of non-linear interactions and because of the temporal and spatial scales that are common to both. Many people have used linear filtration methods to separate wave-induced and turbulent motion (Bendat and Piersol, 1971; Benilov, 1978; Kitaigorodskii et al., 1983; Agrawal and Aubrey, 1992; Wolf, 1999). This method, which we adopt here because the waves are weak and monochromatic and our turbulent frequencies extend to the dominant wave frequency, is based on the coherence between the observed wave height (or pressure from bottom mounted sensors) and the velocity field.

Using Bendat and Piersol (1971)'s method, we calculated a measure of coherence between the pressure (p) and current velocity (u) using,

$$\gamma_u^2 = \frac{C_{pu} C_{pu}^*}{S_p S_u}, \tag{3.6}$$

where C_{pu} is the cross-spectrum of the pressure and along channel flow with C_{pu}^* its complex conjugate, S_p and S_u are the power spectra of the pressure and along channel flow speed respectively. The power spectrum of the wave-removed turbulent motion $S_{u'}$ was then obtained as,

$$S_{u'} = S_u (1 - \gamma_u^2). \tag{3.7}$$

For the cross channel and vertical flow components, the same procedure was applied with negligible corrections made to the cross channel velocity fluctuations since the waves propagate predominantly along channel.

The raw spectral energy densities (S_u dotted lines) and its wave removed form ($S_{u'}$ solid) are shown in Figure 3.7 for the along channel flow speed during 4 stages of the tidal cycle in

2001. Wave-induced orbital motions are non-existent during SLW and greatest 2 hours prior to SHW (as was shown in Figure 3.6). During ebb shortly after SHW small orbital motions exist. Wave frequencies are dominant at $\sim$0.2 Hz. A $-5/3$ slope which is indicative of the inertial subrange where TKE is transferred from the larger energy producing scales to the smaller dissipating scales is also plotted (dashed line) as a reference.

The TKE ($E = 1/2(\overline{u'^2} + \overline{v'^2} + \overline{w'^2})$ was then calculated using the wave-removed energy spectra and is defined as $\int_0^{\infty}(S_{u'} + S_{v'} + S_{w'})df$. The estimates using the linear filtration method, are shown in Figure 3.8. For May 2001, the TKE variation follows an M_4 periodic pattern and the wave correction on flood is almost always higher than that on ebb. By removing the wave motions, the TKE levels were reduced up to 2×10^{-3}m^2/s^2. The level of TKE for ebb and flood tide are similar with increasing magnitude as spring tide approaches. It should be noted that finite record lengths which affect the velocity variance measurement can lead to underestimates of the TKE. Agrawal and Aubrey (1992) comment that this is a limitation of the linear filtration method.

The TKE time series of March 2003 was almost a factor of 10 greater than those observed for May 2001 and was always greatest on the ebb tide, with maximum values $\sim 2\times10^{-2}$m^{2}s^{-2}. The magnitude and duration of flow at 1.4 mab was higher and longer during ebb tide thus creating a stronger shear between the bottom and 1.4 mab (see Figure 3.5). The overall magnitude of TKE on the flood tide was similar to the values of May 2001 but a more pronounced spring/neap variation occurred. Despite the strong ebb flow, wave effects still contributed to a small bias in the TKE estimate.

The dissipation rate of turbulent kinetic energy (ϵ) was estimated using the theoretical equation for TKE in the inertial subrange. First, we applied the linear filtration method described above to remove the wave effects, and then we focused on the frequency range where a $-5/3$ slope existed (Figure 3.7), which overlapped the wave-orbital motion scale. Over the frequency range of 0.1 Hz to 3 Hz we then applied the theoretical, one-dimensional wave number spectrum of velocity fluctuations under the assumption that the turbulence is

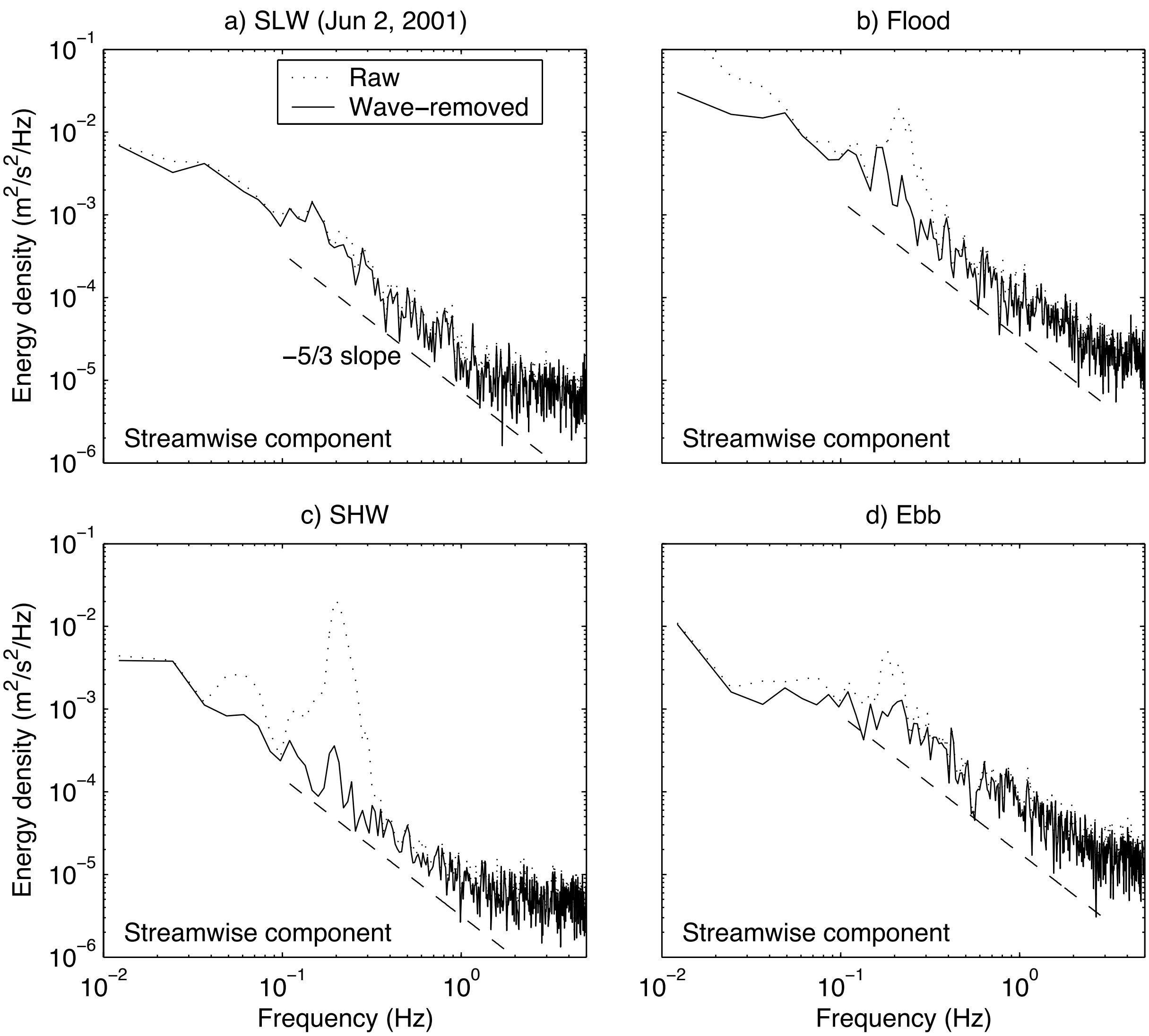

Figure 3.7: Power spectral density measurements of the along channel flow showing the effects of wave orbital motions (dotted curve) and their removal (solid curve). The $-5/3$ slope indicating the inertial subrange for turbulence is shown as a dashed line.

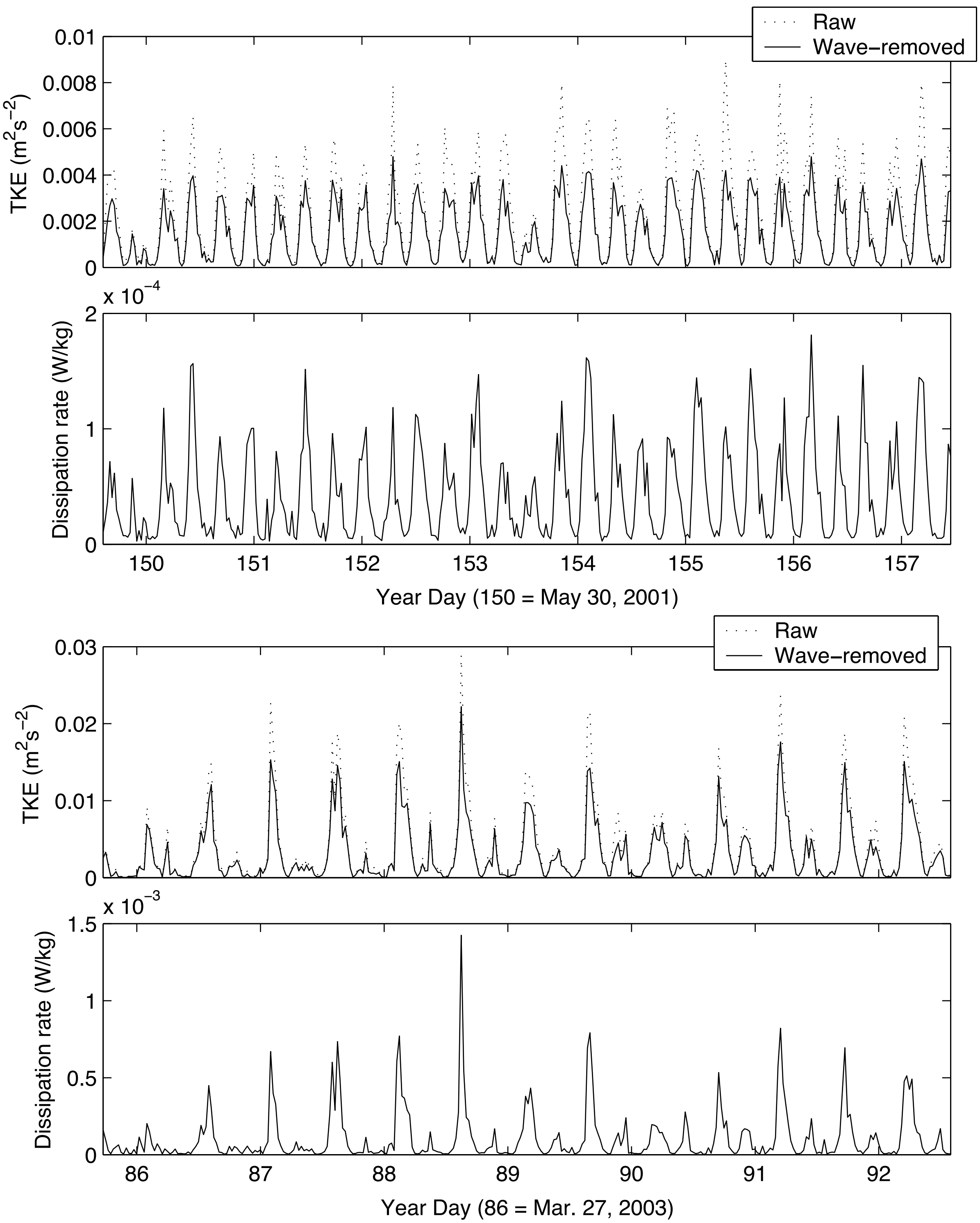

Figure 3.8: The turbulent kinetic energy at 1.4 mab before (dotted curve) and after (solid curve) correction of wave orbital motions. The TKE dissipation rate (per unit mass) is also shown at 1.4 mab. Measurements are shown for May 2001 (upper) and March 2003 (lower).

isotropic and homogeneous (Batchelor, 1951; Tennekes and Lumley, 1999),

$$S_{u'}(f) = \frac{9}{55}\alpha\epsilon^{2/3}f^{-5/3}\left(\frac{2\pi}{U}\right)^{-2/3}, \tag{3.8}$$

where $\alpha = 1.56$ is a constant, f is the cyclic frequency, and $\int_0^\infty S_{u'}(f)df = 1/2\overline{u'^2}$ is the one-dimensional spectral energy density. The turbulent velocity measurements with the ADV produced a noise level of approximately 5×10^{-6} m^2/s^2/Hz during slack water and thus the measurement is limited to when flows were greater than 0.1 m/s.

Figure 3.8 shows the estimated TKE dissipation rate (per unit mass). The levels approach 2×10^{-4}W/kg in 2001 and 1×10^{-3}W/kg in 2003. These are very high values and are expected given the strong tides and shallow waters. In 2003 the dissipation during flood increased as the spring tide approached and actually exceeded those observed in 2001. A detailed turbulent kinetic energy budget is presented below in section 3.4.

3.3.3 Buoyancy Flux

Horizontal and vertical density gradients and velocity shear are ubiquitous characteristics of many estuaries. The straining process (described by Simpson et al., 1990)during flood flow tends to induce an unstable profile in which heavier water overlies lighter water near the bed, and during ebb tends to induce a stable profile. This tendency toward instability creates a vertical mass flux that leads to production of TKE ($g/\rho_o\overline{w'\rho'} < 0$) and conversely the tendency toward stability creates a sink of TKE ($g/\rho_o\overline{w'\rho'} > 0$). Direct measurements of the buoyancy flux after compensating for waves have been obtained by Trowbridge et al. (1999) and Shaw et al. (2001) using benthic acoustic stress sensors (BASS). However, here we used an indirect method developed by Simpson et al. (2005) using the mass conservation equation.

Averaging (3.3) with respect to depth, assuming a rigid lid and flat bottom, and then subtracting from (3.3) gives

$$\frac{\partial(\rho - \hat{\rho})}{\partial t} + (U - \hat{U})\frac{\partial \rho}{\partial x} = -\frac{\partial \overline{\rho' w'}}{\partial z}, \tag{3.9}$$

where $\hat{\rho}$ and $\hat{U}$ are the depth averaged density and along channel velocity respectively. The buoyancy flux, defined as $B = (g/\rho_o)\overline{w'\rho'}$ can then be estimated for well-mixed and partially mixed regimes of the Altamaha River. When $B > 0$ ($B < 0$) it represents a sink (source) of TKE corresponding to ebb (flood) flow. Integrating (3.9) from some height ζ from the sea bed to the surface (h) gives,

$$B(\zeta) = \frac{g}{\rho_o}\frac{\partial \rho}{\partial x}\int_{\zeta}^{h}(U - \hat{U})dz, \tag{3.10}$$

for the vertically homogeneous case and,

$$B(\zeta) = \frac{g}{\rho_o}\frac{\partial \rho}{\partial x}\int_{\zeta}^{h}(U - \hat{U})dz + \frac{g}{\rho_o}\int_{\zeta}^{h}\frac{\partial(\rho - \hat{\rho})}{\partial t}dz, \tag{3.11}$$

for stratified and unsteady conditions.

Vertically Homogeneous Case

The buoyancy flux derived by (3.10) above is positive (negative) for stable (unstable) conditions and increases as ζ increases, becoming a maximum at $\zeta = \zeta_0$ where $U(z) = \hat{U}$ and then decreases as the surface is approached. Figure 3.9a) and b) shows time series of the buoyancy flux in the water column for May 2001 and March 2003 respectively using equation (3.10). An average horizontal density gradient of $\partial\rho/\partial x \simeq 1.5 \times 10^{-3}$ kg/m^4 was approximated as the difference between moored CTDs and anchor station CTD profiles (a separation of 1114 m). The difference remained somewhat constant over the two 13 hour times series and the variability observed ($< 1 \times 10^{-3}$) was not large enough to affect the buoyancy flux value. For 2003 the horizontal density gradient was measured using the GCE-LTER long term monitoring station at GCE9 together with deployed surface and bottom CTDs (a separation of 2125 m). Because of the large river discharge the gradient ranges from 0 to 5.0×10^{-3}kg/m^4 causing the buoyancy flux to disappear during the low water tidal phase.

The buoyancy flux for May 2001 varied periodically with the tide from -1.8×10^{-5}W/kg to 1.14×10^{-5} W/kg with negative values on flood and positive values on ebb. This implies that the flood tide was inducing instabilities and the ebb was tending to stabilize. The depth

a)

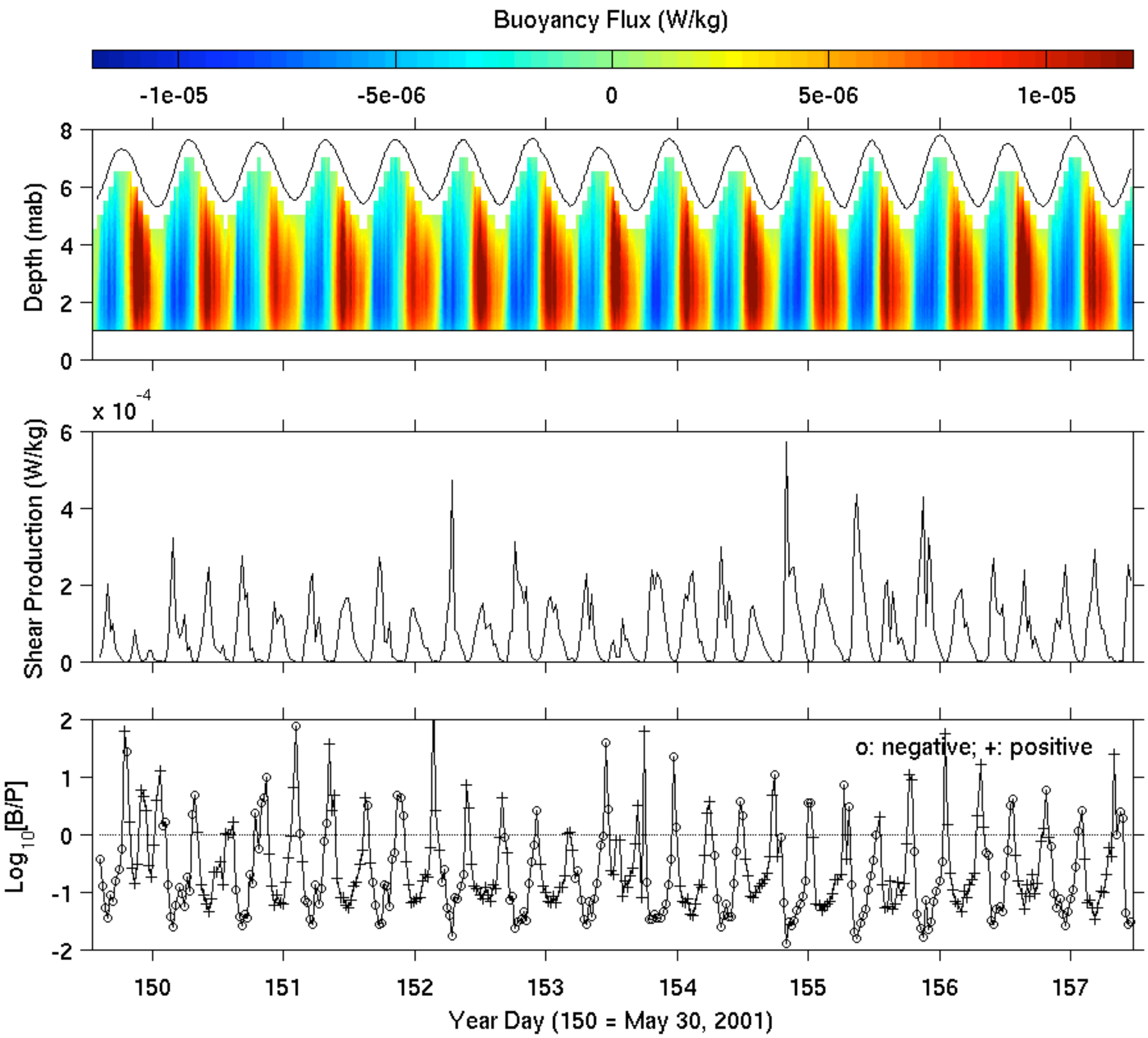

Figure 3.9: (a) The buoyancy flux as a function of depth for a constant along channel density gradient ($\partial\rho/\partial x = 1.5 \times 10^{-3}$kg/m^3/m), shear production and the ratio of buoyancy (source or sink) to shear production for May 2001. (b) The tidally varying along channel density gradient, buoyancy fluxes, shear production and ratio of buoyancy to shear production for Mar 2003.

b)

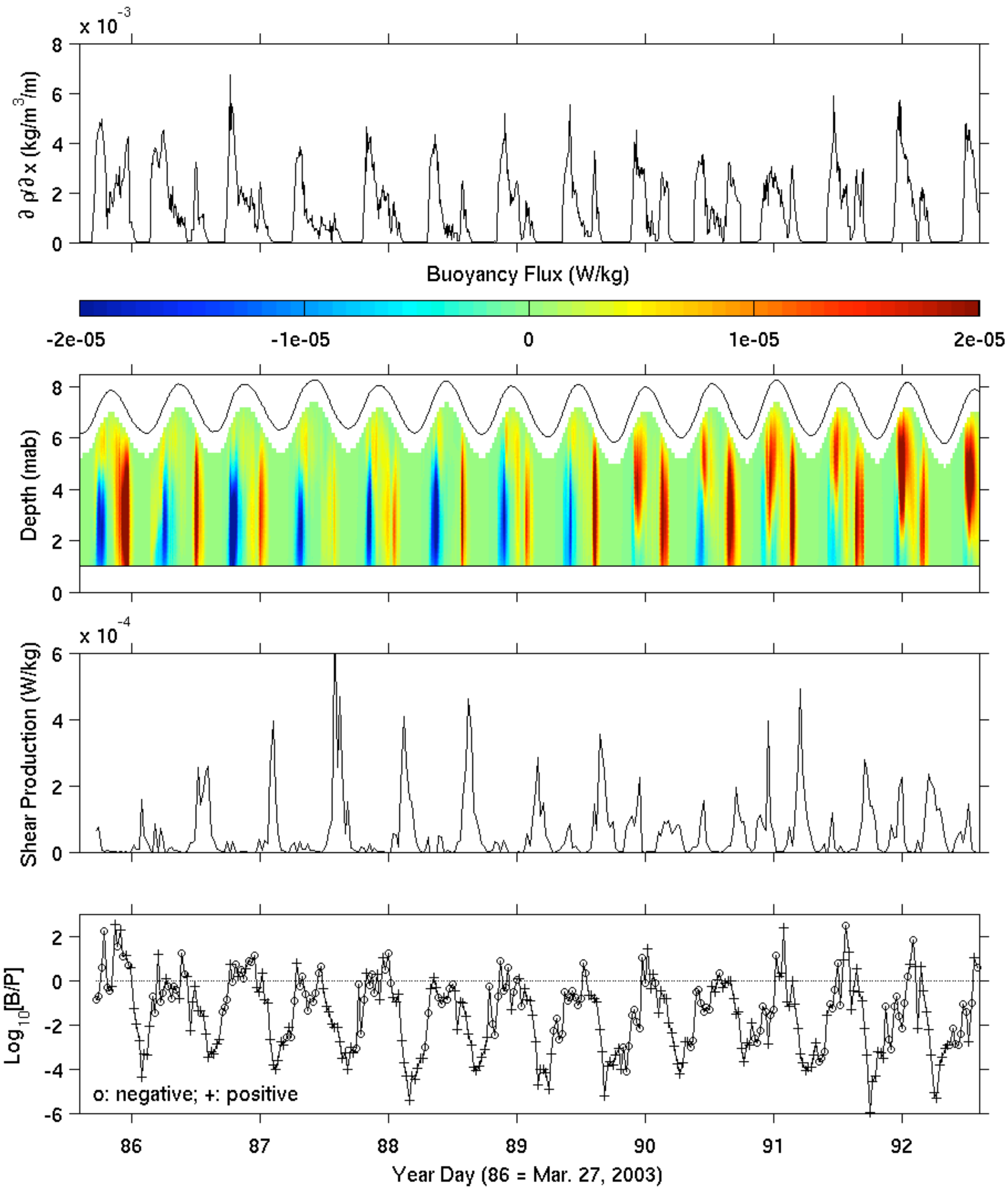

Figure 3.9 continued.

of the maximum buoyancy flux was at approximately 2.5 mab. For March 2003 period, the buoyancy flux during neap tide showed a production of energy (negative) during flood and a sink of energy (positive) during ebb with values higher than those in 2001 due to the higher along channel density gradient. As the spring tide approached and when the winds were strong from the westerly direction the flood tide was also tending to stabilize as much as during the ebb. The depth of maximum buoyancy flux as a result was higher up in the water column during this time approaching 5 mab.

The shear production at 1.4 mab, calculated using the observed Reynolds' stresses and mean shear,

$$P = -\overline{u'w'}\frac{\partial U}{\partial z} - \overline{v'w'}\frac{\partial V}{\partial z}, \tag{3.12}$$

can be compared to the buoyancy production at the same depth as shown in Figure 3.9. The ratio of buoyancy to production is defined as the flux Richardson number $\mathrm{Ri}_f = B/P$. For 2001 the buoyancy flux on ebb was approximately 10% of the shear production ($\mathrm{Ri}_f = 0.1$) and on flood it approximated $\mathrm{Ri}_f = 0.03$ implying that buoyancy was generally an energy sink as opposed to a producer. During slack water when the production and buoyancy approach 0 the ratio behaved uncertainly. Based on these estimates we can approximate the minimum mixing rate in the near bottom for a given stratification of $N^2 = (-g/\rho_o)\partial\rho/\partial z = .002s^{-2}$, from the equation,

$$K_\rho = \frac{\mathrm{Ri}_f}{1 - \mathrm{Ri}_f}\frac{\epsilon}{N^2}. \tag{3.13}$$

which is derived from a balance of production and dissipation of energy and from the parameterizition $-\overline{\rho' w'} = K_\rho \partial\rho/\partial z$. For $\epsilon = 1 \times 10^{-4}$ W/kg, $K_\rho = 55$ cm^2/s during flood and $K_\rho = 15$ cm^2/s on ebb.

For 2003 shear production on the flooding tide was very small toward the neap tide and increased as the spring tide approached. When the shear production was small on flood the buoyancy production could be approximately 30% the shear production. As the spring tide approached, the buoyancy was reduced to approximately 10% of the shear production similar to the 2001 case. On ebb tide, however, the production of energy was high so that the flux

Richardson number Ri_f became very small (approaching 0) and buoyancy effects were negligible. Mixing rates during this time when the stratification had increased to $N^2 = 0.02\mathrm{s}^{-2}$ were approximately $K_\rho \simeq 5 - 20$ cm^2/s. The Ozmidov length scale, which characterizes the largest possible overturn that turbulence can accomplish in the presence of stratification is defined as $\ell_O = (\epsilon/N^3)^{1/2} \approx 0.2$m where $N \sim 0.02\mathrm{s}^{-2}$ is the Brunt-Väisälä frequency. This is the largest eddy scale that can overturn and essentially mix with surrounding water and is a small number which corroborates the low vertical mixing parameter. For 2001 $\ell_O \approx 1$m and the water column had higher mixing rates.

Stratified Conditions

When there was a strong vertical density gradient that varied with time, as seen for example in March 2003, the buoyancy flux can be estimated based on equation (3.11). Using the 13-hour CTD time series, the buoyancy flux was estimated using the temporally varying inhomogeneous term and compared to the buoyancy flux caused by shear straining the density field. For May 2001 the water column was well mixed most of the time. The inhomogeneous terms had an order of 10^{-6}W/kg and thus was negligible compared to the straining term.

Figure 3.10 compares the level of the buoyancy flux computed with only advection and shear with that computed with only the non-steady vertical density variations, and with that computed by their sum. It is evident that the temporal variations of stratification played a key role in affecting the buoyancy flux calculated by this method, as vertical inhomogeneities created greater magnitudes with order of 10^{-5} W/kg. The maxima occurred primarily when there was a large change in stratification, going from well-mixed vertically homogeneous conditions at slack low and high water to strongly stratified conditions during ebb and flood flow. The flux Richardson number at 1.4 mab was modified accordingly showing that buoyancy was a greater sink of energy during the flooding tide.

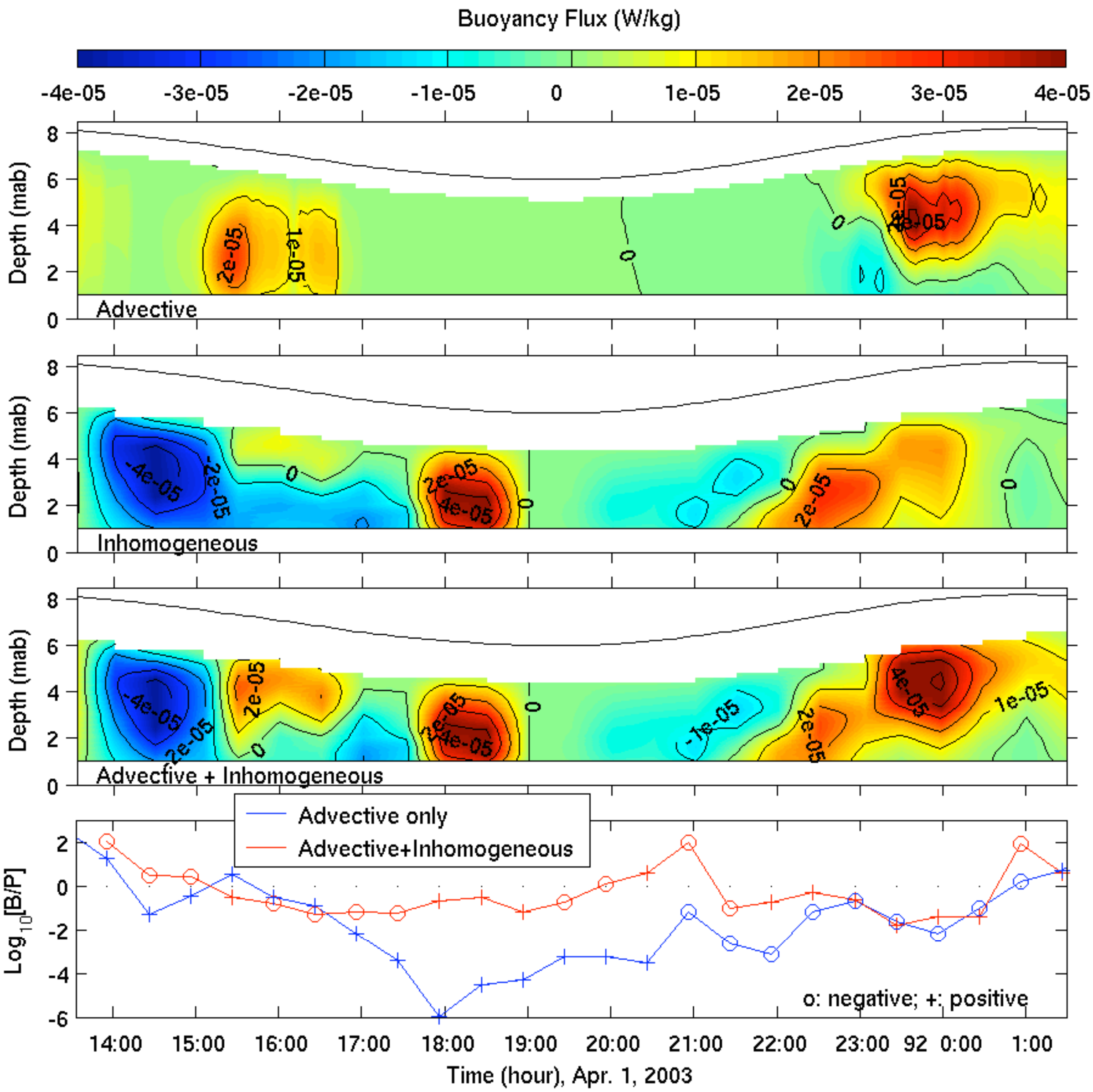

Figure 3.10: Contributions to the buoyancy flux by the straining of the horizontal density gradient (advective), the inhomogeneities that vary with time (non-steady state), and their sum (advective+inhomogeneous). The flux Richardson change as a result of the non-steady inhomogeneous water column.

3.3.4 TKE Budget

A local TKE budget is useful for examining the dynamics of turbulent flow. In shear flow whose statistical properties are steady and homogeneous, the TKE is introduced at the larger scales where the mean flow does work against the Reynolds stresses, and is dissipated at the smaller scales by molecular viscosity. A balance of production and dissipation is achieved provided that buoyancy losses (or gains) produced by density variations do not exist. Several examples of this balance in the estuaries were shown by Sanford and Lien (1999), Trowbridge et al. (1999), and Stacey et al. (1999). Both Sanford and Lien (1999) and Trowbridge et al. (1999) found that the two terms were balanced near the bottom; Sanford and Lien (1999) found that the dissipation exceeded the production above mid depth. Stacey et al. (1999) divided the water column into three vertically separated regimes where TKE transport potentially plays a role in moving energy into or out of the regions: i) the near bottom, where the local production is greater than local destruction of turbulence ($P - B > \epsilon$), which implies that energy must get transported out of the region, ii) the interface, where the local production is balanced with the local destruction of turbulence ($P - B \simeq \epsilon$), and finally iii) above the interface, where the destruction exceeds the local production ($P - B < \epsilon$) and this layer must receive energy from the near bottom.

The scatter diagrams shown in Figure 3.11 summarize the TKE budget at 1.4 mab for the May 2001 and March 2003 cases separated into flood and ebb phases of the tidal cycle. Dissipation of TKE energy (ϵ) is plotted versus production ($P - B$) where B was predominantly an order of magnitude smaller than the other terms. The flood tidal cycle for May 2001 clearly showed more enhanced production of energy compared to its dissipation level. This is because the Reynolds stresses were generally a factor of 2 greater on flood than on ebb. During ebb tide the TKE rates show more of a balance between production and dissipation. This asymmetry in TKE rates can be due to the asymmetric forcing between flood and ebb tide discussed previously (wave-current interactions and/or barotropic/baroclinic pressure gradients). Higher production of energy in the lower layer during flood implies that energy

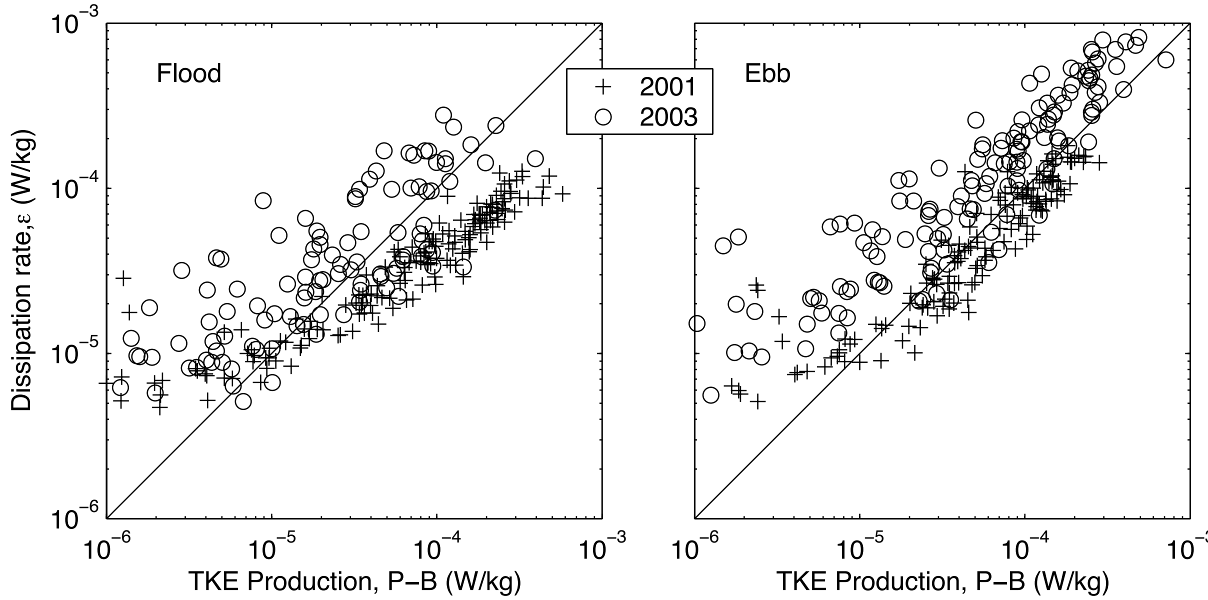

Figure 3.11: Scatter plots of TKE dissipation (ϵ) versus production ($P - B$) rates during flood and ebb flow. May 2001 data are represented by + and Mar 2003 data by $\circ$.

may be exported out of the area by turbulent transport mechanisms. These are identified by the triple correlation terms $\partial/\partial x_j(\overline{u_j'E})$ in the turbulent kinetic energy equation.

In March 2003, regardless of ebb or flood tide, the dissipation of energy was generally greater than the production (by a factor of 2) and followed a linear relationship. In this case the dissipation may be a more accurate measure of the local conditions because transport mechanisms may add to the shear production, bringing turbulence to the area. A snapshot of the Richardson number showed very stable conditions during the advancing and receding tide. This implies that the stratification suppresses the destabilizing effects of the shear, thus reducing the production of energy.

3.4 Numerical Simulation

Numerical modeling can provide a synthetic approach to understanding physical processes even where simplified equations are used. In this section, we will try to answer two questions: 1) Can a one-dimensional model be used to simulate the time varying turbulence characteristics throughout the water column using surface and bottom temperature and salinity and depth-averaged current velocity profiles? and 2) How are turbulent parameters such as the Reynolds stress, shear production and dissipation rates distributed in the water column and how do they change? Below we provide brief introduction to the turbulence model used and discuss the simplifications made for this study.

3.4.1 The Numerical Model

The General Ocean Turbulence Model (GOTM, Burchard et al. (1999)), sometimes called the $k-\epsilon$ two-equation turbulence model, is available as freeware for simulating small-scale turbulence and vertical mixing as a function of depth. This model has been used in many oceanic environments: applications to estuaries, open seas, and lakes are summarized in the GOTM manual. Examples of estuarine environments where this model has been used include studies in the Eastern Scheldt of the Netherlands and Knebel Vig of Denmark. In the Eastern Scheldt, which is weakly stratified with fine sediments, the TKE dissipation rate was well predicted by including fine sediments to account for bottom friction characteristics. In the Knebel Vig, which is a highly stratified estuary, the simulated dissipation rate showed greater values just above the halocline, indicating that the halocline acts like a boundary for turbulent mixing. Open sea cases in the northern North Sea and the Irish Sea were used to simulate sea surface temperature variation, mixed layer depth, and the vertical structure of temperature using input factors such as surface velocity, surface buoyancy flux (including solar radiation and the net heat flux) and wind stress. (For more typical examples of these model runs, see Burchard et al. (1999)).

In addition, Burchard et al. (1998), Burchard and Baumert (1995), Burchard et al. (2002) and more recently Simpson et al. (2002) carried out model-data comparisons of the semi-diurnal cycle of dissipation in a region of freshwater influence (ROFI) environment and showed that the model gives a reasonable account of dissipation and its asymmetric pattern on ebb and flood tide. Through their model analyses, the variation of quantities that are related to turbulent mixing was determined by the role of convective motions forced by tidal straining near the end of the flood tide. Because of these successes we applied this model in the Altamaha River Sound, which varies from a well mixed to a partially mixed regime. The model enables us to extend our turbulence predictions to the entire water column in order to find if there are any significant variations with depth. Time series of current data (i.e. ADV or ADCP data) and water column CTD characteristics obtained during the observation periods described previously were used as input to this one-dimensional model.

The major assumptions for the model are i) a uniform velocity field (hence advection terms are neglected, ii) negligible horizontal diffusive terms, and iii) a hydrostatic balance. The model is based on seven dynamical equations: momentum equations for u (eastward) and v (northward), hydrostatic approximation in the vertical, potential temperature T (℃), salinity S (psu), turbulent kinetic energy k (m^2/s^2) describing large scale motions and turbulent kinetic energy dissipation rate ϵ (m^2/s^3) describing the small scales. The governing equations are given in Cartesian coordinates with x directed east, y directed north and z upward with a reference of $z = 0$ located at mean sea level. The water column ranges from $-H(x, y)$ to $\zeta(t, x, y)$. These simplified equations are summarized as follows:

$$\frac{\partial u}{\partial t} - \frac{\partial}{\partial z}\left((\nu_t + \nu)\frac{\partial u}{\partial z}\right) = -\frac{1}{\rho_0}\frac{\partial p}{\partial x} + fv, \tag{3.14}$$

$$\frac{\partial v}{\partial t} - \frac{\partial}{\partial z}\left((\nu_t + \nu)\frac{\partial v}{\partial z}\right) = -\frac{1}{\rho_0}\frac{\partial p}{\partial y} - fu, \tag{3.15}$$

$$\frac{\partial p}{\partial z} + g\rho = 0 \tag{3.16}$$

$$\frac{\partial T}{\partial t} + u\frac{\partial T}{\partial x} + v\frac{\partial T}{\partial y} + w\frac{\partial T}{\partial z} - \frac{\partial}{\partial z}\left((\nu_t^{'} + \nu')\frac{\partial T}{\partial z}\right) = \frac{1}{c_p\rho_o}\frac{\partial I}{\partial z}, \tag{3.17}$$

$$\frac{\partial S}{\partial t} + u\frac{\partial S}{\partial x} + v\frac{\partial S}{\partial y} + w\frac{\partial S}{\partial z} - \frac{\partial}{\partial z}\left((\nu_t^{'} + \nu^{''})\frac{\partial S}{\partial z}\right) = 0, \tag{3.18}$$

$$\frac{\partial k}{\partial t} - \frac{\partial}{\partial z}\left(\nu_k\frac{\partial k}{\partial z}\right) = P + B - \epsilon, \tag{3.19}$$

$$\frac{\partial \epsilon}{\partial t} - \frac{\partial}{\partial z}\left(\nu_\epsilon\frac{\partial \epsilon}{\partial z}\right) = \frac{\epsilon}{k}(c_1 P + c_3 B - c_2\epsilon), \tag{3.20}$$

where ν_t is the vertical eddy (turbulent) viscosity, $\nu = 1 \times 10^{-6}\mathrm{m}^2\mathrm{s}^{-1}$ is the molecular viscosity, g is gravitational acceleration, p is pressure, $f = 2\Omega\sin\phi$ is the Coriolis parameter with the earth's angular velocity Ω and latitude ϕ, I is the net heat flux (including short wave solar radiation, longwave radiation, sensible and latent heat fluxes), $c_p = 3980 \;\; \mathrm{J\ kg^{-1}K^{-1}}$ is the specific heat capacity for sea water, ρ_o is a mean density, $\nu' = 1.4 \times 10^{-7}\mathrm{m}^2\mathrm{s}^{-1}$ and $\nu^{''} = 1.1 \times 10^{-9}\mathrm{m}^2\mathrm{s}^{-1}$ are the molecular diffusivities for temperature and salinity respectively, ν_t' is the vertical eddy diffusivity for both heat and salt, ν_k is the eddy diffusivity for k, $P = \nu_t((\frac{\partial u}{\partial z})^2 + (\frac{\partial v}{\partial z})^2)$ is the shear production of turbulent kinetic energy. The buoyancy production of TKE defined in GOTM is $B = -(g/\rho_o)\overline{\rho' w'} = \nu_t^{'}\frac{g}{\rho_o}\frac{\partial \rho}{\partial z}$, ν_ϵ is the eddy diffusivity for ϵ and c_1, c_2 and c_3 are experimental parameters. The bottom boundary condition for dynamic transport is the standard condition $u, v = 0$ at $z = -H$. Since the model uses a relationship between the eddy viscosity and turbulent kinetic energy to solve the TKE equation, it also needs a dimensionless function which is the so-called stability function. For this stability function which contains the second-momentum closure assumptions, the new

Canuto et al. (2001)'s method was adopted. This function depends on shear and stratification effects.

The pressure gradients along x and y can be expressed as

$$-\frac{1}{\rho_0}\frac{\partial p}{\partial x} = -g\frac{\rho}{\rho_0}\frac{\partial \zeta}{\partial x} + \int_z^\zeta \frac{\partial b}{\partial x}dz \tag{3.21}$$

$$-\frac{1}{\rho_0}\frac{\partial p}{\partial y} = -g\frac{\rho}{\rho_0}\frac{\partial \zeta}{\partial y} + \int_z^\zeta \frac{\partial b}{\partial y}dz \tag{3.22}$$

where $b = -g\frac{\rho-\rho_o}{\rho_o}$ is a measure of buoyancy and the potential density ρ is calculated using the UNESCO equation of state. The terms on the right-hand side in (3.21) and (3.22) are the barotropic and baroclinic pressure gradients, respectively. If tide gauges along the Altamaha existed then the pressure data could be used directly to measure the barotropic forcing term. The density gradients along x and y directions are parameterized from observational data as the baroclinic effect cannot be ignored.

The input data for the model also includes depth averaged current velocity, surface and bottom temperature and salinity, and longitudinal (and latitudinal when available) temperature and salinity gradients for the 2001 and 2003 observational programs, which were previously introduced in Figures 3.3 and 3.9b. As the surface temperature is directly input into the model, the net heat flux is ignored. For 2001 a constant longitudinal density gradient was used whereas for 2003 the time varying gradients was used. The depth-averaged velocities were used in the model to calculated the barotropic tidal forcing term and to represent flow variations like ebb-dominance due to buoyancy.

In order to apply the 1-dimensional turbulence model to the Altamaha River estuary, the model was first tuned using observed data. Profiles of current velocity, potential temperature and salinity together with the turbulent parameters of interest are output from the model all as a function of time and as a function of depth. By comparing the observed quantities to model-computed variables at a specific depth, for example with the ADV data at 1.4 mab, the model was tuned by altering the bottom friction parameter. Different bottom roughness values were tested for each of the two cases and the ones showing the best correlation with observations were chosen: $z_o = 0.5$ cm for 2001 and $z_o = 13$ cm for 2003. These are large bottom roughness coefficients that may correspond to seabed ripple forms. Once model-calculated and observed parameters showed the best correlation between the flow, stress, TKE and dissipation results at 1.4 mab, we then analyze turbulent parameters as a function of depth.

3.4.2 Model Results

This numerical model was evaluated to determine if it is possible to simulate the mean flow and turbulent flow characteristics such as the Reynolds stress, TKE and dissipation rate, in such an energetic tidally forced system. If this is the case, it will then be possible to simulate depth dependent variations. Figure 3.12a) and b) show a comparison between model-computed and observed values at the ADV station (1.4 mab) for 2001 and 2003 respectively. The model results, in general, capture the main temporal variability for each parameter. For 2001 a bottom roughness of $z_o = 0.5$ cm was necessary to get the correct levels of bottom stress (i.e. Reynolds stress) and as a result the simulated flow was slightly damped compared to the observations. This is more apparent in 2003 where the bottom roughness was increased to $z_o = 13$ cm, presumably because of the increased drag due to the higher river flow.

The flood/ebb asymmetries in bottom stress for 2001 that we attributed to imbalances in barotropic forcing or wave effects is clearly not evident in the modelled output for 2001. The model-computed Reynolds stress does not have the higher negative values during the flood tide. This may be because the wave effect was not included in the modeling or it may be because a constant along channel density gradient was used thereby underestimating the baroclinic forcing during the flood tide. For 2003 the flood/ebb asymmetries associated with the higher river discharge period is captured, which clearly shows the increase in friction velocities during flood as spring tide is approached. The TKE and dissipation rate of TKE is modulated with the M4 tidal period, with maxima corresponding to strong flows and minima

a)

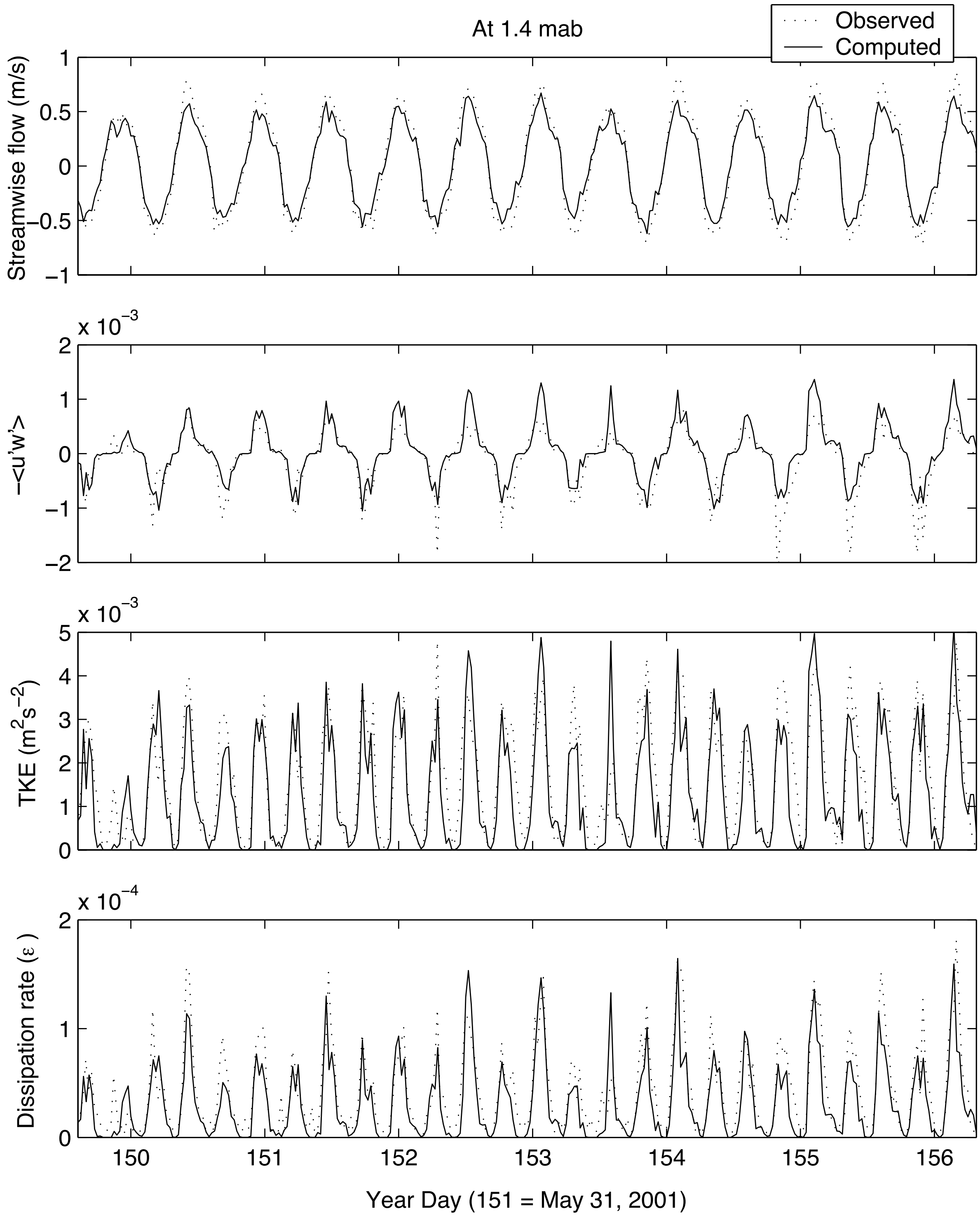

Figure 3.12: Comparison of model and observed streamwise flow, Reynolds stress, TKE and dissipation rate of TKE all at 1.4 mab during a) low river discharge of May 2001 and b) high river discharge of Mar 2003.

b)

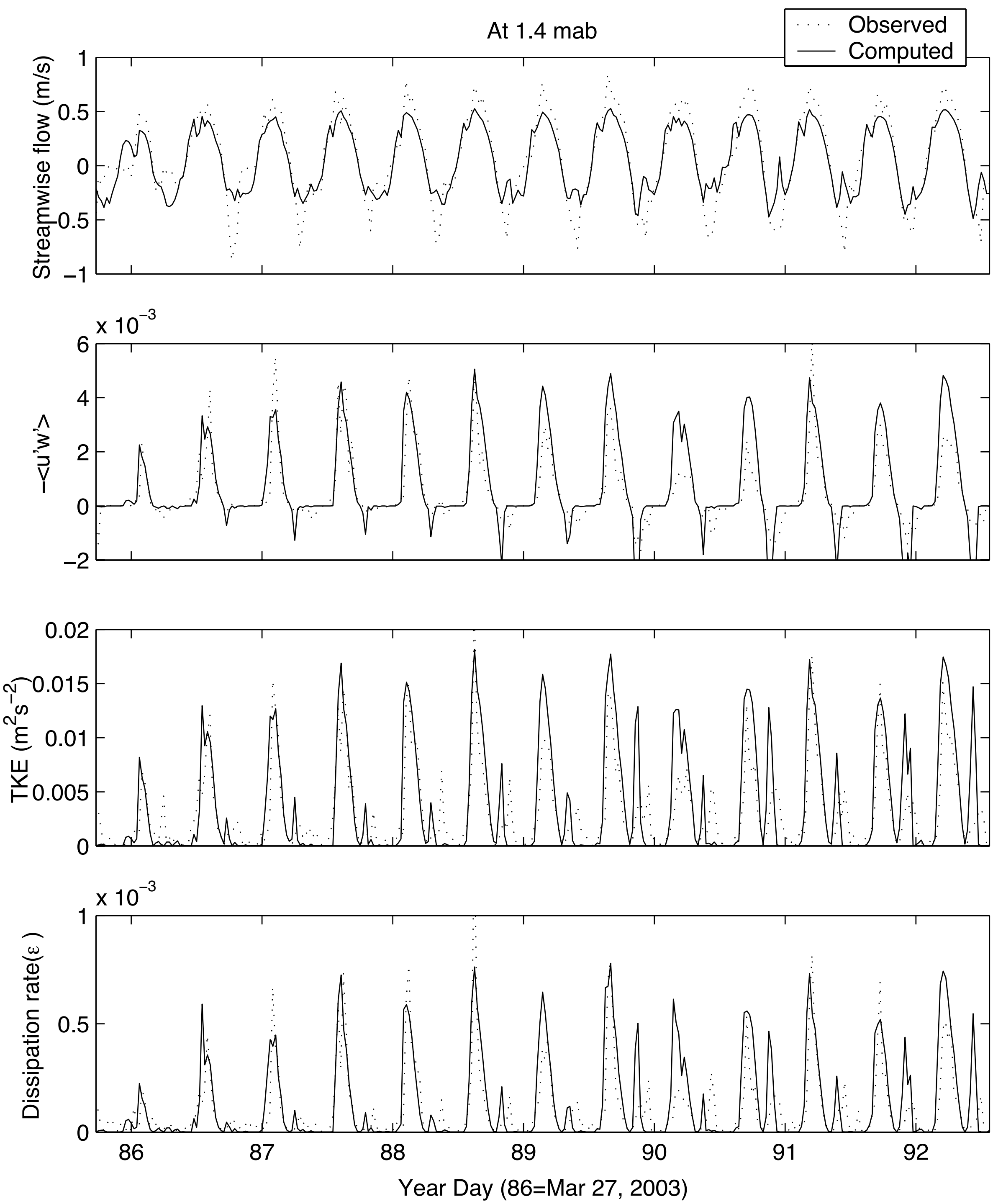

Figure 3.12 continued

during slack water. The comparison between the modeled and measured results for 2001 are not very different: the amplitude and phasing are generally consistent. For 2003, however, the phasing for the flood tide is not captured. The TKE and dissipation rate measurements are maximal somewhat later in time during flood than predicted with the model. This is because the short duration flood is not captured by the model. In general the model-data comparison for 2001 is fairly good whereas for 2003 many discrepancies exist.

Figure 3.13 shows linear correlation coefficients between the modeled parameters and the observed values. Despite some of the discrepancies described previously all variables were well correlated giving a correlation coefficient (r) greater than 0.8 except for the dissipation rate in 2003. The 2001 situation is clearly modeled better than the 2003 case.

One of main goals for applying the model, within known limitations, was to predict observations of turbulence throughout the water column to identify variations or features as a function of depth and time. Figure 3.14 shows the model results of the density, Reynolds stress magnitude, shear production and TKE dissipation rate as a function of time and depth. According to the 2001 results, the stress, shear production, and dissipation rate are all maximal at the bed during both flood and ebb tides; they are then minimal during slack water. As the height above the sea bed is increased these quantities are attenuated showing that the whole water column forms part of the bottom boundary layer because the water is well mixed. In fact the shear production and dissipation extend higher into the water column during the ebb tide than during the flood. This is presumably because of the uniformly sheared flow during ebb tides compared to a sheared profile concentrated close to the bed on flood. This flood/ebb asymmetry clearly has implications for the bottom boundary layer height which is low during flood and higher in the water column during ebb.

The ebb-dominance in 2003 is clearly seen in all the turbulence parameters in Figure 3.14b. What is interesting to note is that the Reynolds stress becomes maximal only when the water column becomes homogeneous and that is about half way through the ebb tide.

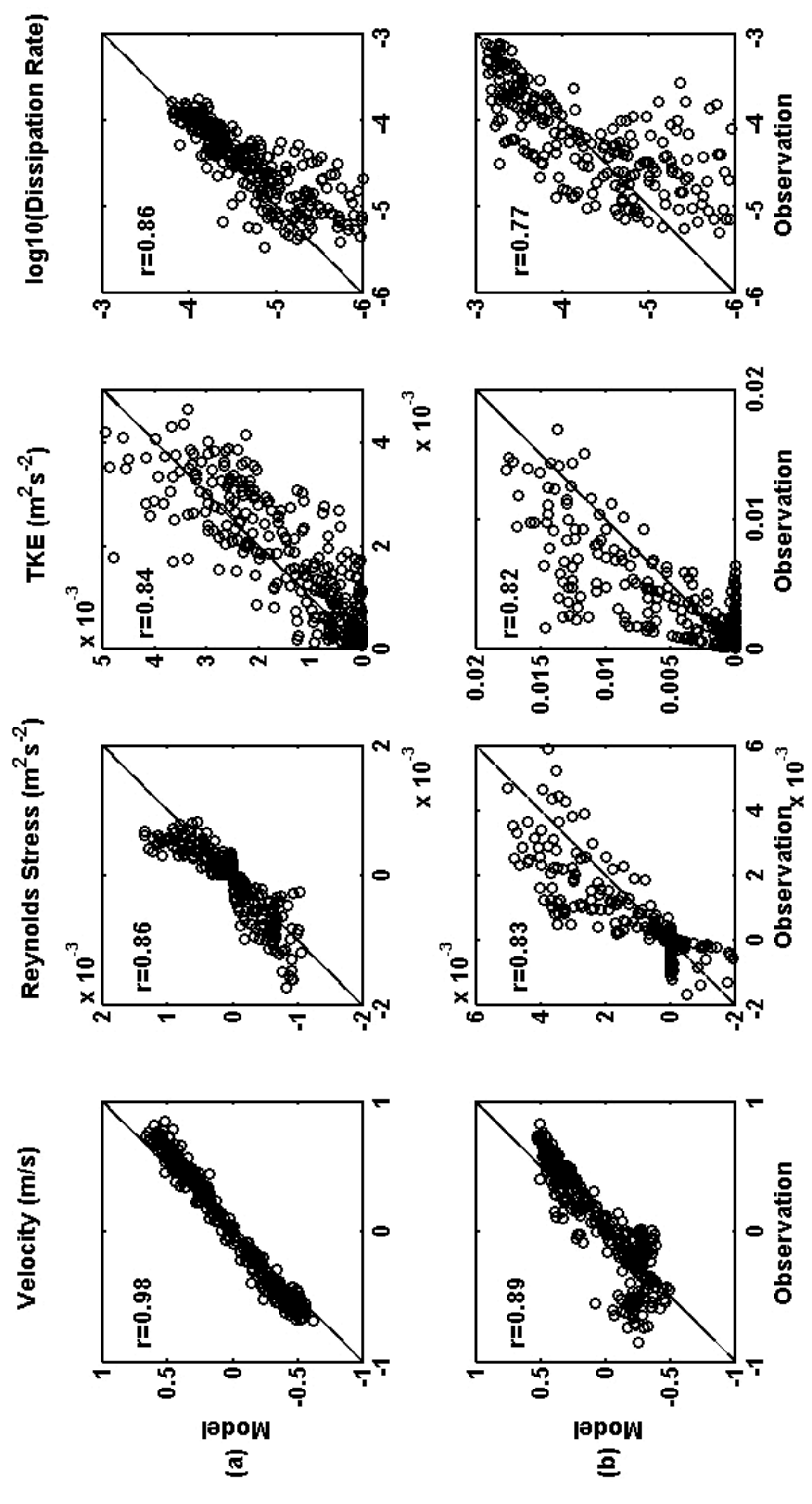

Figure 3.13: Correlation coefficients between model and observation results at 1.4 mab during a) low river discharge of May 2001 and b) high river discharge of Mar 2003.

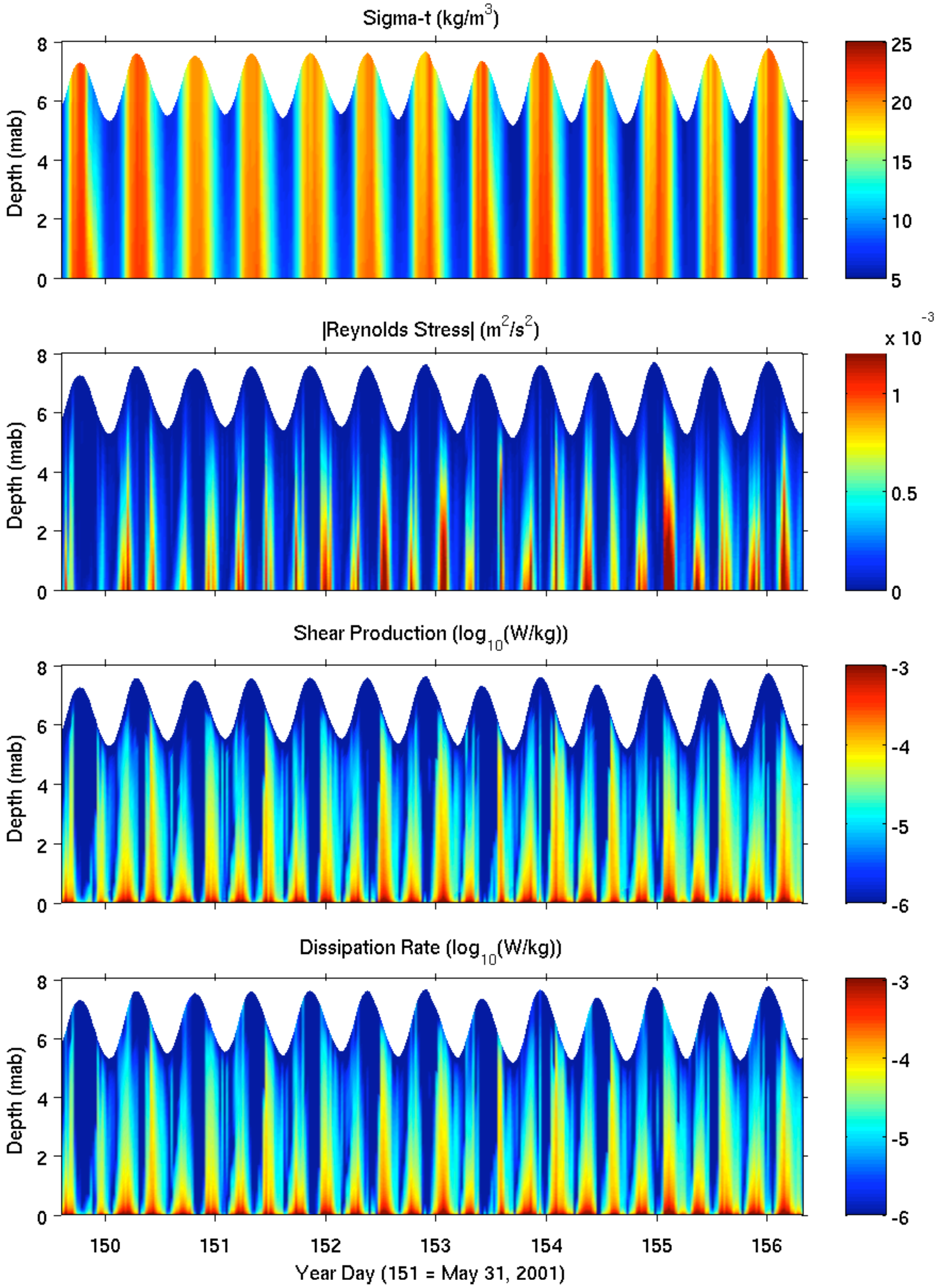

a)

Figure 3.14: Model-computed turbulence flow characteristics: σ_t, Reynolds stress, shear production and the TKE dissipation rate during a) low river discharge of May 2001 and b) high river discharge of Mar 2003.

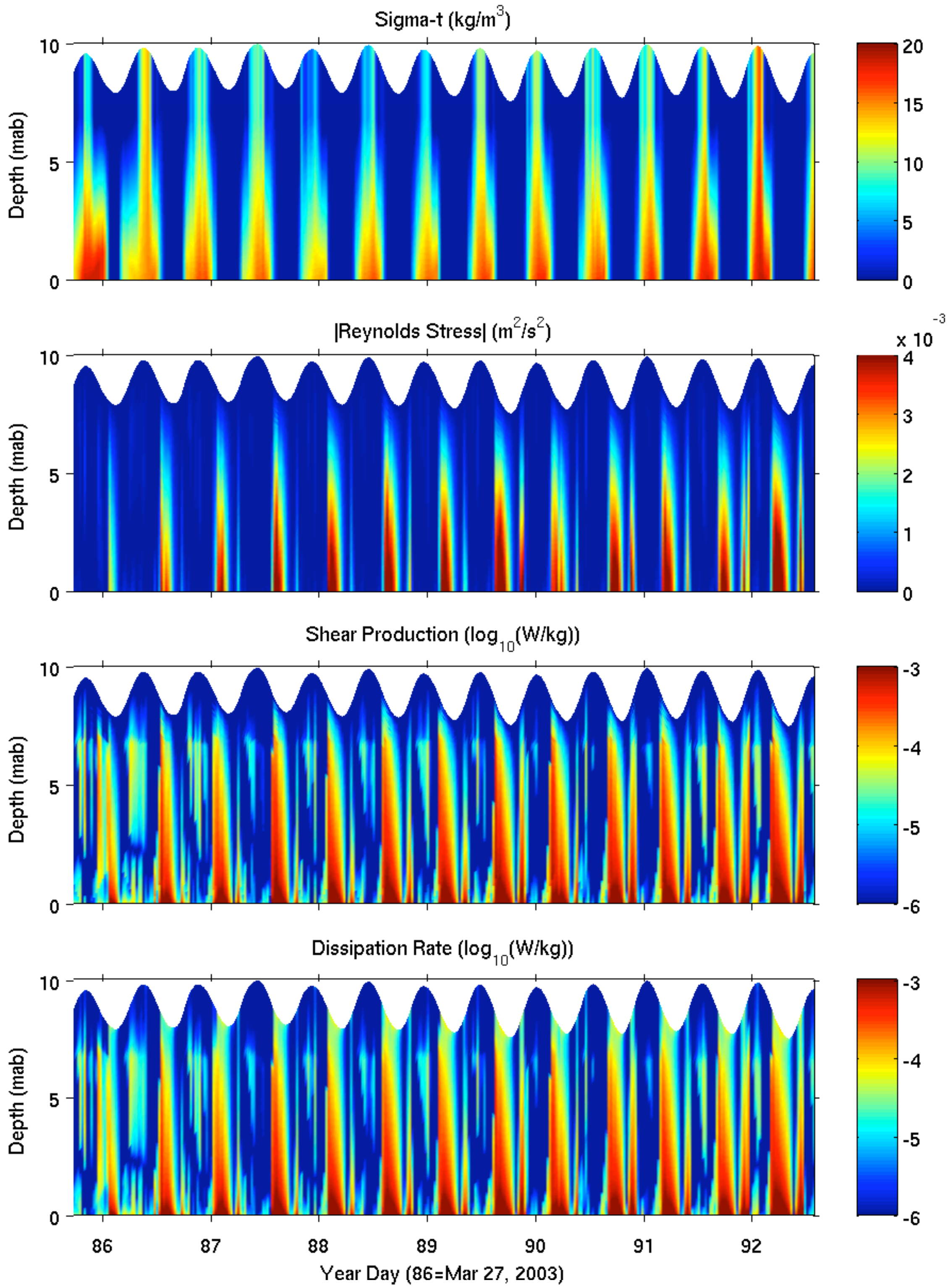

b)
Figure 3.14 continued

The strong stratification that exists suppresses the turbulence in the bottom boundary layer. Another key feature to note in Figure 3.14b) is the existence of high turbulence levels within the water column that is separated from the bottom boundary layer. This occurs predominantly when there is a strong pycnocline, which implies that the strong stratification acts like a boundary layer during the flooding tide, enhancing the shear production and dissipation. The application of this one-dimensional model to a time of high river discharge clearly remains a challenge and further observations of turbulence within the water column are needed in order to verify such occurrences.

3.5 Summary and Conclusions

A study of the turbulent flow characteristics during two different river discharge periods, was carried out in the Altamaha River estuary, GA. The measurement period covered a spring/neap cycle in May 2001, and March 2003, using several bottom mounted flow measuring instruments, and a 13 h time series of detailed water column profiles from an anchored vessel. The results obtained clearly show the effects of river discharge, tidal straining of the density field, waves and wind forcing on turbulent characteristics.

The marked increase of river discharge in 2003 changed the flow structure and density distribution, giving a shortened tidal excursion distance of 4 km, partially stratified conditions during flood and ebb flow and a horizontal density gradient that varied with the tidal cycle from 0 (completely fresh conditions at low water) to 6×10^{-3} kg/m^4. The ebb was stronger due to the increased river-driven barotropic pressure gradient, giving a net residual flow approaching 0.2 m/s in the surface layer. The near surface flood tide, in addition to being shortened by the river flow was also retarded by offshore westerly wind bursts.

The low and high river discharge period resulted also in different gradient Richardson numbers. In 2001, neap tide showed stable stratification starting at low water and continuing to high water. Thus, we expect turbulent activity to be low in the upper water column and high closer to the boundary. During spring tide, the water column becomes essentially well mixed and turbulent levels should be higher throughout the water column. The asymmetry in the shear distribution between flood and ebb presumably demonstrates the competing effects of the barotropic tidal and baroclinic gravitational forcing. When the barotropic and baroclinic forces are aligned during the flood, stresses can be increased, which potentially provides a mechanism by which sediment and benthic material are resuspended and transported upstream. Future experiments in this channel (with tide gauge instruments that can resolve the sea level difference) during low river discharge should include a study of the momentum balance to fully test this hypothesis. Also, ADCP instruments implementing the beam variance method for resolving Reynolds stresses throughout the water column should be implemented. It should be noted that our deployments were programmed to log all pings in beam coordinates but due to high pitch and roll angles the stress calculations were useless.

In 2003, because strong stratification existed on both the ebb and flood, it result in stable conditions in the this region. With the stronger and prolonged ebb tide, near bottom turbulence showed very strong asymmetries, always giving higher values on ebb. This presumably is because the river- and tide- induced barotropic pressure gradient are aligned during ebb and become greater than the opposing gravitational baroclinic effect. This provides a mechanism for transport of material seaward throughout the water column.

Wave forcing in the channel could also contribute to flood and ebb asymmetries by increasing the hydraulic roughness and hence bottom friction felt by the current boundary layer. This effect is expected to be small given that the friction velocity is so high. These effects can be tested with future modeling of one-dimensional turbulence that includes wave parameterizations. Nevertheless, non-linear wave-current interactions can still provide a mechanism which can affect the Reynolds stress. To remove any biases on the stress associated with waves, future studies could implement the dual sensor differencing technique of Trowbridge (1997) where two ADV's are separated by a distance larger than the turbulence scales and smaller than the wave scales. Because of waves, corrections were made to the spectral energy density of the turbulent velocity so that the TKE and the dissipation rates do not include these effects. The TKE levels were reduced up to 5×10^{-3} m^2/s^2 and the levels for ebb and flood tide became similar in magnitude for 2001.

Buoyancy flux estimations, assuming vertically homogeneous conditions, showed that the flood tide is an energy source (B$<$ 0) and that the ebb tide is an energy sink (B$>$ 0), consistent with the SIPS process where flood tide induces instabilities and the ebb tends to stabilize them. Our estimates of the buoyancy input indicate that it is relatively small compared to the shear production with a ratio $|\mathrm{Ri}_f| = |B|/P \sim 0.03 - 0.1$ for low river discharge (2001). The ratio of $|\mathrm{Ri}_f| = |B|/P \sim 0.001 - 0.1$ for high river discharge (2003) had higher values in magnitude corresponding to ebb tide. For neap tide the B/P ratio is relatively greater, approaching 0.3. Mixing levels, calculated from the flux Richardson number, dissipation and stratification were higher during 2001 than 2003. In 2003, vertical homogeneity could not be assumed given that the stratification changed with time - going from essentially homogeneous at slack low water to strongly stratified during flood to ebb. Including this effect in the buoyancy flux estimate, changed the flux estimate on the ebb as a result of the rapidly decreasing salinity. In our estimation of the vertical buoyancy flux we neglected the horizontal buoyancy fluxes ($\partial u'\rho'/\partial x$) which may also be a factor contributing to temporal density variations.

The budget for the rate of change of turbulent kinetic energy clearly shows that in general $P - B \neq \epsilon$ in this environment, particularly in 2003 when there was a high river discharge. The difference between the TKE production and dissipation is up to a factor of 2 and suggests that turbulent transport mechanisms may play a role in the energy balance. The buoyancy term was estimated using the dynamic approach in which the flux is estimated as a residual after other terms in the simplified density conservation equation are measured. This is generally small compared to the shear production but we have included it for completeness. A direct measurement of the buoyancy flux term is not easy since it requires fast sampling of two sensors (flow and CTD) that must be synchronized in time.

The numerical modeling described the structure and change of the turbulent flow characteristics fairly well for 2001. According to model results, the Reynolds stress, shear production and dissipation rate showed peak values at both flood and ebb with maxima at the bed, and decreased upward in the water column with ebb tide extending higher into the water column than flood. The bottom boundary layer thus engulfs the whole water column on ebb. This is consistent with the velocity shear observed and may correspond to flood/ebb asymmetries in the baroclinic and barotropic forcing due to advected buoyancy fluxes. For 2003, because of the high river discharge and strong stratification, ebb-dominance in the turbulence quantities were predicted but the phasing was not for the flood tide. Measurements were not extended to the entire water column and they revealed internal turbulence properties that are separated from the bottom boundary layer during flood to high water. The increase in dissipation within the water column during the flooding tide may correspond to just above the halocline, which acts as an internal boundary layer.

Acknowledgments. This work was supported by the NSF (OCE-9982133) as part of the Georgia Coastal Ecosystems Long Term Ecological Research (GCE-LTER) project (http://gce-lter.marsci.uga.edu/lter/index.htm) and by the University of Georgia Research Foundation, Faculty Research Grant program . The authors would like to thank Captain Raymond Sweatte and the crew of the R/V Savannah for their enthusiastic support in instrument deployment and recovery.

Chapter 4

RESIDUAL CIRCULATION IN THE ALTAMAHA RIVER ESTUARY[1]

[1]Ki Ryong Kang and Daniela Di Iorio. To be submitted to *Estuarine, Coastal and Shelf Science.*

Abstract

A brief study of estuarine residual flows during a neap tide was performed using 13-hour roving acoustic Doppler current profiles (ADCP) and conductivity-temperature-depth profiles in the Altamaha River Estuary, GA. The method used here is a harmonic analysis one where the M2 tide is fit to the data and then separated from the flow so that a residual is obtained. We applied this method to depth-averaged data and to depth-dependent data. Results show that the M2 tide explains over 95% of the variability observed in the data. As the flow was dominated by the M2 tidal component in a narrow channel, the tidal ellipse distribution was essentially a back-and-forth motion. The amplitude of M2 velocity component increased slightly from the river mouth (0.45 m/s) to land (0.6 m/s) and the phase showed fairly constant values in the center of the channel and rapidly decreasing values near the northern and southern shoaling areas. The residual flow and transport calculated from depth-independent flow and depth-dependent flow shows temporal variability over the tidal time scale. Strong landward residual flows appeared during slack water which may be attributed to increased baroclinic forcing when turbulent mixing decreases. During flood and ebb flows the residual flow was seaward.

Keywords: tidal flow, residual flow, M2 component, ADCP, estuarine circulation, Altamaha River Estuary

4.1 Introduction

An estuary is a complex system where seawater is diluted with freshwater from land runoff (Dyer, 1997). This dilution process takes place because of enhanced turbulence and mixing levels due to many forcing mechanisms like tide-, buoyancy-, wind- and wave-induced motions. In addition, many substances are transported from the estuary to the near-shore zone via advective and dispersive processes. While tidal currents produce large fluxes of material or water itself, it is the tidally averaged (or removed) residual circulation (or net transport) that controls the net exchange of material. Thus, residual circulation is important for understanding net transport in estuarine systems. Estuarine circulation results from two important forcing mechanisms: barotropic and baroclinic pressure gradient flows (Jay, 1991; Jay and Smith, 1990; Simpson, 1997). The barotropic pressure gradient flow is driven by horizontal changes in sea surface elevation and is produced by several mechanisms: the propagating tidal wave that changes direction depending on the flooding or ebbing phase of the tide and the amount of freshwater outflow that is directed seaward. The baroclinic pressure gradient is caused by horizontal changes in density and drives the flow towards regions of lower density, which can result in a barotropic response in order to maintain continuity. In general, the barotropic forcing is larger than baroclinic-driven flows.

Nonlinear variations in bottom friction can create asymmetries in the propagation of the tidal wave, thus causing net transport in the longitudinal direction (Ianniello, 1977, 1979; Li and O'Donnel, 1997). Li and O'Donnel (1997) have argued that local nonlineararities in bottom friction are responsible for their observations of landward flux at both sides of the shoaling area of channels, with outward flux occurring in the central deeper waters. The baroclinic pressure gradient flow is forced by the longitudinal or latitudinal density gradient, with a maximum value at depth and zero at the surface. By averaging over the tidal period or removing the dominant tidal forcing the classical residual circuation is established in the estuary, wherein the landward baroclinic flow at depth is balanced by the seaward barotropic force at the surface. The streamwise density gradient is generally most important factor for describing gravitational circulation, but cross-stream gradients can affect secondary circulation patterns.

Estuarine residual flow has been studied by many researchers. Pritchard (1952, 1956), and Hansen and Rattray (1965) were the first to describe density-driven gravitational circulation in an estuary and Simpson et al. (1990) explained the role of horizontal density gradients in creating periodic vertical stratification by straining. Nunes-Vaz et al. (1989) studied the role of turbulence in estuarine mass transport and suggested that the time varying baroclinic-driven flow becomes maximum during slack water because turbulence and stratification are minimal. Stacey et al. (2001) found that the residual flow can be a periodic pulse strongly correlated with the tidal cycle because of the interactions between shear, stratification and mixing. The transverse or lateral structure of secondary circulation has also been studied by many researchers, (see for example Wong, 1994; Li and O'Donnel, 1997; Valle-Levinson et al., 2003) who have shown that net inflow tends to be concentrated in the deeper channels while the outflows appear over the shoals. Specifically Valle-Levinson et al. (2003) pointed out the importance of friction and Coriolis force in the circulation patterns. They demonstrated that asymmetries in the lateral structure of the streamwise flow disappear when large frictional damping is applied.

The estuarine system of the Altamaha River is complex because of the many different pathways that the river can take to the coastal area. Some of the flow is directed southward through the intracoastal waterway and some northward through various channels (see Figure 1.1 and 4.1). The Altamaha River is one of Georgia's largest rivers, providing extensive fresh water to coastal sea; river discharge has a large seasonal variability with peak flows during early spring and fall (depending on the number of hurricanes and tropical storm events) and then substantially less during the rest of the year (see Figure 4.2). The tidal range varies from 1.5 to 3 m during times of strong spring/neap variations. The flow is predominantly ebb-dominated, with magnitude $>$ 1m/s (DiIorio and Kang, 2003) in Altamaha Sound, where the width of main channel is about 1 km with a maximum depth of 8-10 m.

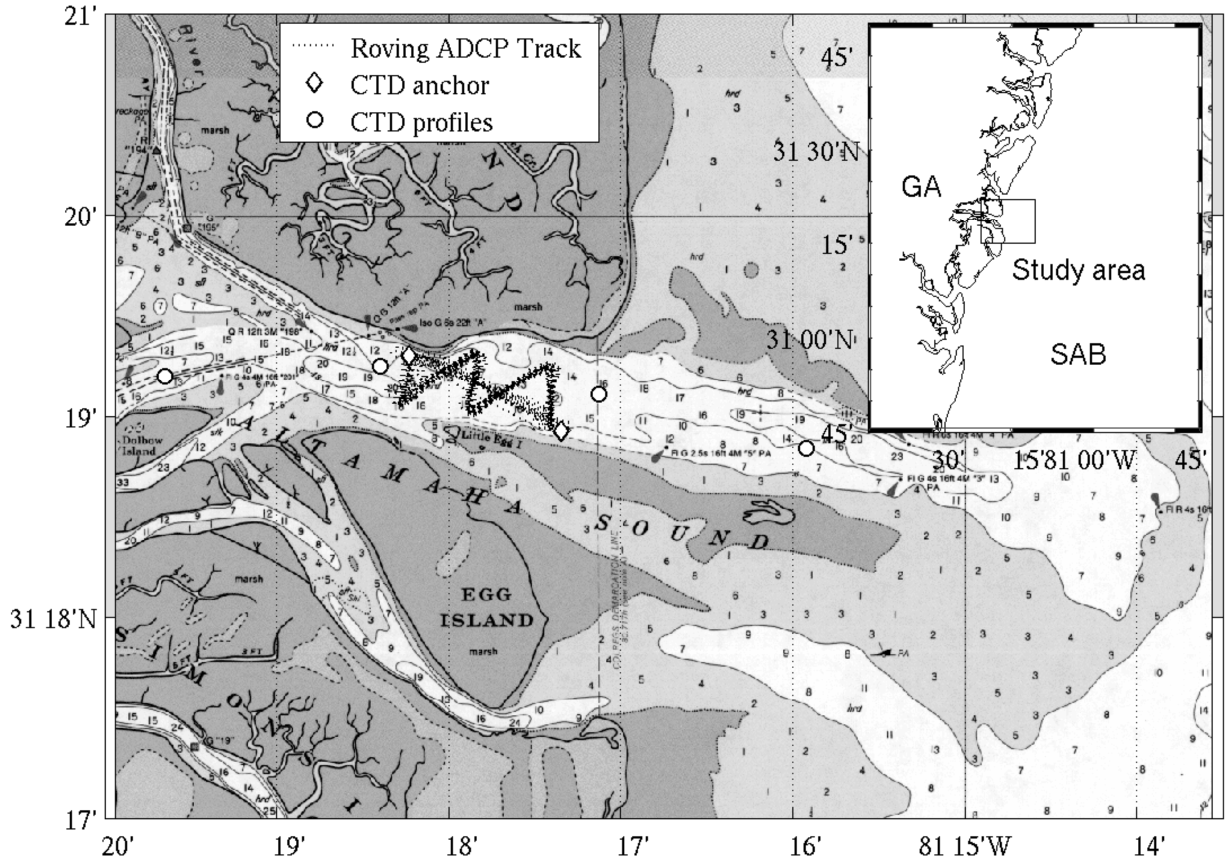

Figure 4.1: Study area showing roving ADCP track and CTD sampling stations on a hydrographic chart of the Altamaha River Sound.

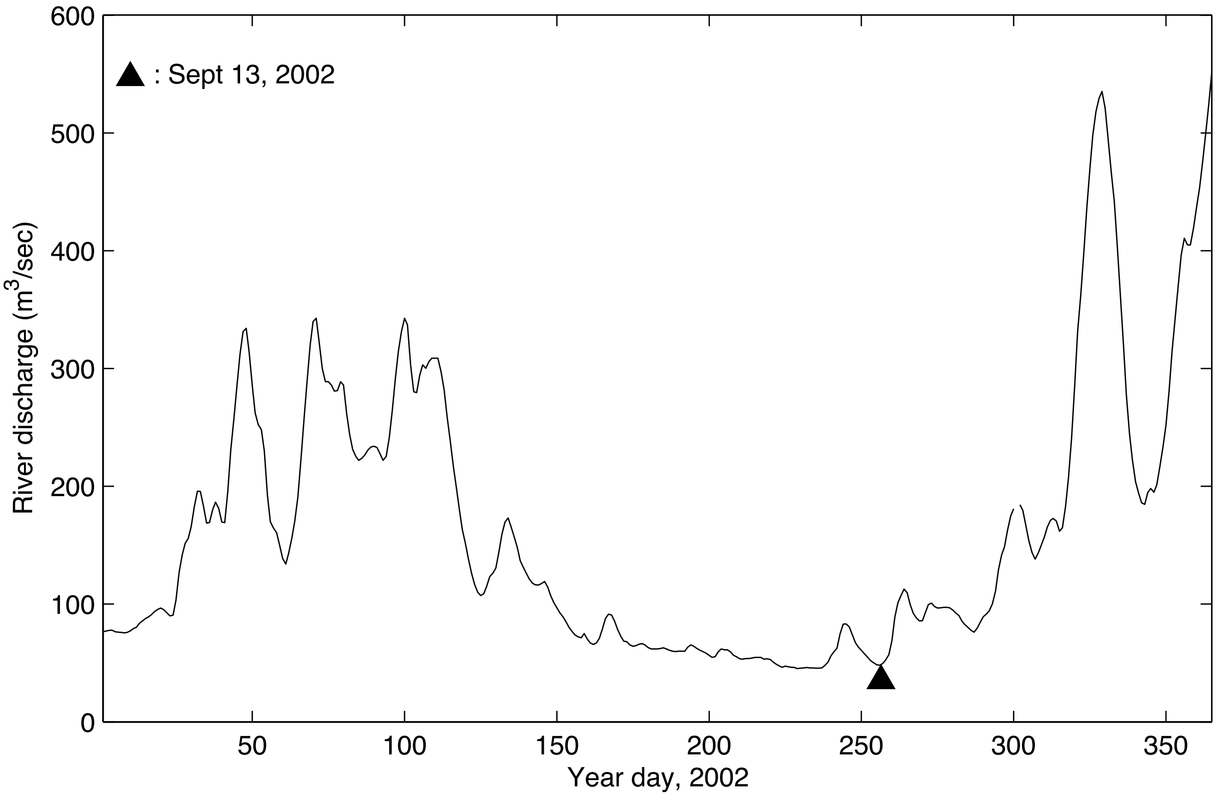

Figure 4.2: Discharge data for year 2002 showing that our measurement campaign was during a low river transport time.

The present study was focused on understanding the characteristics of the main transport and residual circulation through Altamaha River Sound during a time when the total river transport was low. The design and data processing procedure is described in Section 4.2, and in Section 4.3 we discuss the characteristics of the surface density distribution, the latitudinal and longitudinal density variations as a function of depth, the semidiurnal lunar tide (M2) characteristics, residual flow, and transport. Section 4.4 summarizes significant findings.

4.2 Field Sampling and Data Processing Methods

During the September 2002 LTER quarterly monitoring survey, a 13-hour time series of roving acoustic Doppler current profiles (ADCP) and conductivity-temperature-depth (CTD) profiles were performed at neap tide to investigate the cross- and along- channel variations of the current structure in Altamaha River Sound. This field campaign was specifically designed to resolve the residual flow and hence the net transport across three sections in the main channel by estimating the M2 tide in a least squares sense. Residual flow in this context refers to the flows without the principal lunar semidiurnal M2 tide. Figure 4.1 shows an expanded hydrographic chart of the study area with the ship track (dotted line) and CTD profile stations. Diamonds indicate CTD profiles over the 13-hour time series sampled on Sept 13, 2002 (neap tide) and circles show the CTD transect locations carried out on Sept 18, 2002. During this period ocean winds, measured 30 km offshore, blew consistently from the southerly direction with magnitudes 5 m/s (not shown here). The river discharge gauged at Doctortown, about 95 km upstream in the Altamaha River, was less than 100 m^3/s (see Figure 4.2).

In this study, a 1200 kHz broadband ADCP from RD Instruments mounted to a mast on the port side was used, together with flow through thermosalinographs and an SBE25 CTD profiler from SeaBird. The ADCP data were sampled at 2 Hz continuously for 13 hours with 0.25 m vertical bin size. The ADCP was operated in bottom tracking mode with the ship's gyrocompass as an external heading. The ship track line was in a zig-zag shape specifically designed to obtain three cross sections along the channel. Each zig-zag took approximately 45 min and a total of 17 such transects were made over the course of the 13 h tidal cycle. For each cross section we constructed a grid having a resolution of 30.8 m in the latitudinal direction and a varying resolution in the horizontal in order to encompass the horizontal spread of the transect lines (see Figure 4.3). The distance between section A and C was about 1.43 km, and the horizontal resolution for section A, B and C was 291, 264 and 238 meters, respectively. The mean position of all samples in each grid box is shown in Figure 4.3 as open circles. These points represent the grid position of the flow and surface salinity time series. Each profile of current within the grid represents an approximate average over 20 s (while the ship was within each grid) and 17 such averaged profiles exist at each grid point corresponding to 13 h of data.

As the data for each grid were unevenly sampled in time, the velocity profiles and depth time series were linearly interpolated at 30 min intervals prior to the tidal analysis. To capture the tidal flow characteristics, we applied the tidal harmonic analysis method, developed by Foreman (1996) and implemented into MATLAB as T_TIDE by Pawlowicz et al. (2002), to depth-averaged flow data,

$$\hat{\mathbf{U}}(x_i, y_j, t) = \frac{1}{h}\int_0^h \mathbf{U}(x_i, y_j, z_k, t)dz \tag{4.1}$$

and mean water depth h measured at each grid cell. The velocity vector $\mathbf{U} = (U, V)$ is the east-west and north-south velocity component, x_i is the along channel coordinate with $i = 1, 2, 3$ representing the number of grids along the channel (section A, B,and C respectively), y_j is the cross channel coordinate with $j = 1, ..., M$ is the cross channel grid number going from south to north, z_k is the depth with $k = 1, 2, ..., N$ is the vertical bin number going from just below the surface ($z_1 = -z_b$, where z_b is the blanking distance of the ADCP) to the bottom, and t is the time step. We have not corrected for variable surface elevation due to the tidal oscillation as described by Li et al. (2003) since most of our measurements are based on depth-averaged results. The lower panel of Figure 4.3 shows an example of the

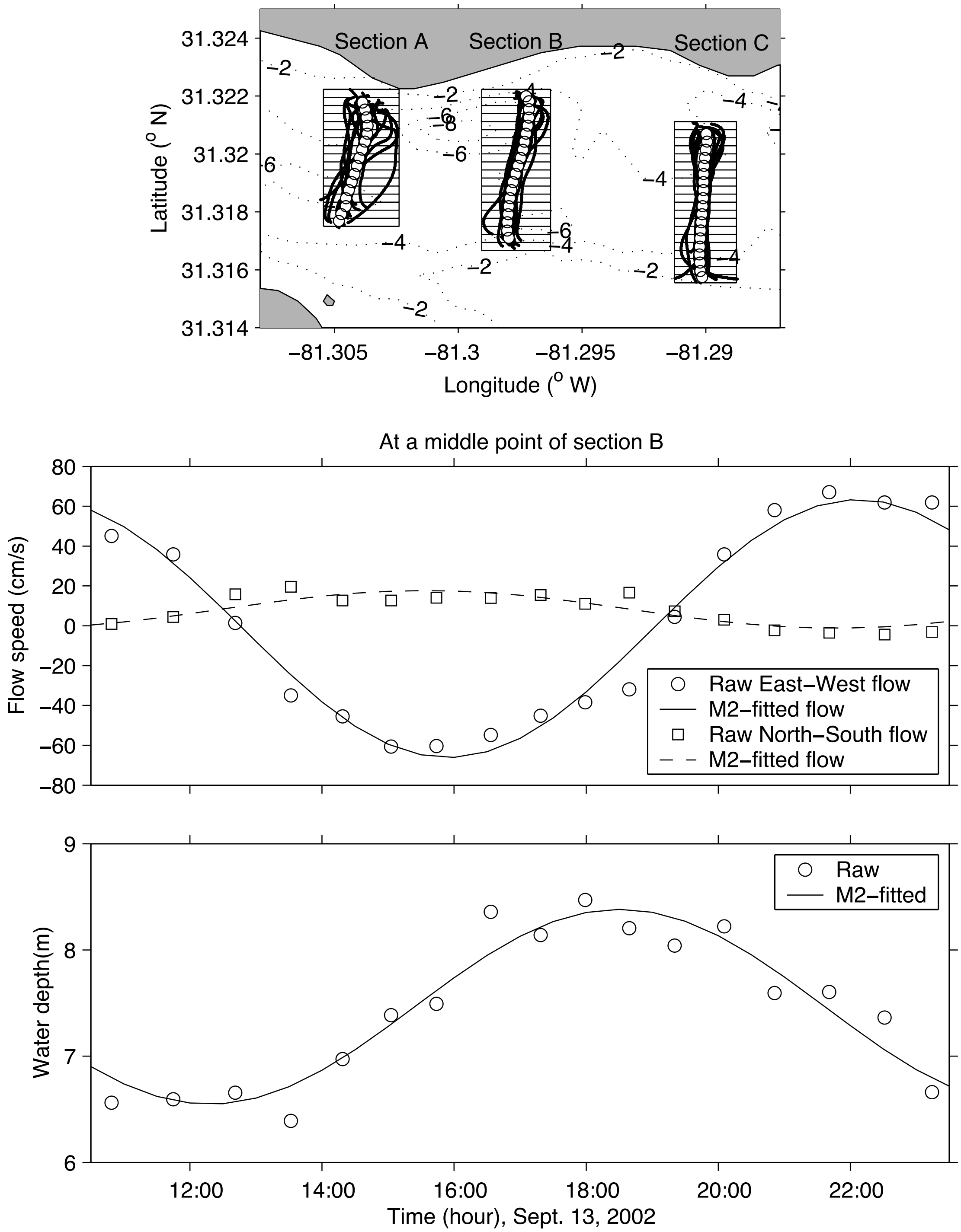

Figure 4.3: The roving ADCP tracks and averaged location of 1 second (about 30 m) grid cell in latitude direction. The circles indicate the mean location of each grid and solid lines show the tracks of the ship. The dotted line indicates the depth contour in meter unit. The lower panels show an example of M2 tidal constituent fit to the depth-averaged velocity and pressure data.

	Flow Velocity (cm/s)	Sea Level Height (m)
Major Axis	66.06	0.93
error Major Axis	9.07	.17
Minor Axis	1.62	
error Minor Axis	5.26	
Phase (deg)	315.29	30.85
error Phase (deg)	7.95	10.83

Table 4.1: An example of the amplitude (Major and Minor axes) and phase for the M2 tidal constituent fit to the velocity vector and sea level height. 95% confidence intervals are shown by the error terms.

depth averaged flow and the water depth with the M2 tidal constituent superimposed. This example represents the flow in the middle of section B at coordinate (x_2, y_{10}).

Both the east-west (solid curve) and the north-south (dashed curve) flow are plotted together with a least squares fit of the M2 tide showing a strong visual correlation with the observed data. The tidal height also shows a good fit in a least squares sense (minimum difference between observed and fitted values) indicating that this area is dominated by the semi-diurnal lunar tide. The greater variability in the water depth measurement may correspond to bathymetric features within the grid influencing the measurement rather than the tidal height. Table 4.1 lists the amplitude and phase parameters for this fit. The semidiurnal M2 component explained over 97% of the total variance of the depth-averaged flow and 94% of the tidal height variance. This method of applying an M2 tide to roving ADCP data was used by Li et al. (2000) and Li and Valle-Levinson (1998) for inferring the tidal elevation in shallow waters and for separating barotropic and baroclinic flows. In the Altamaha estuary case, the phase difference between the velocity and water depth fits was approximately -75.5 deg indicating that the M2 tidal propagation in this area was between a progressive and a standing wave.

The depth-averaged and depth-dependent residual flow was estimated by subtracting the M2 component derived from the depth-averaged and depth dependent flow,

$$\hat{\mathbf{U}}_r(x_i, y_j, t) > \; = \; \hat{\mathbf{U}}(x_i, y_j, t) - \hat{\mathbf{U}}_{M2}(x_i, y_j, t) \tag{4.2}$$

$$\mathbf{U}_r(x_i, y_j, z_k, t) \; = \; \mathbf{U}(x_i, y_j, z_k, t) - \mathbf{U}_{M2}(x_i, y_j, z_k, t) \tag{4.3}$$

where $\hat{}$ corresponds to depth averaged values and $\mathbf{U}_{M2} = (U_{M2}, V_{M2})$ is the M2 tidal flow constituent using either depth averaged flow and flow at each depth. The residual volume transport within each grid cell was then calculated by,

$$Q(x_i, y_j, t) = h(t)\Delta y \hat{U}_r(x_i, y_j, t) \tag{4.4}$$

where Δy is the latitudinal grid size of 30.8 m and h is the time varying water depth.

4.3 Results

4.3.1 Density Distribution

One key feature in most estuaries is the longitudinal salinity distribution ranging from freshwater to seawater, which is a driving mechanism for the baroclinic or gravitational circulation. A ‘sideways’ estuarine circulation can exist for wide estuaries having lateral density gradients and for relatively narrow estuaries where frictional effects are important (Valle-Levinson et al., 2003). As the flow strains the horizontal gradient, periodic stratification will exist. Figure 4.4 shows density profiles taken during the low and high water transects along the channel between stations -2 and 6 km in the Altamaha. The profiles show that the estuary is essentially well-mixed during this time with weak stratification existing between 0 and 2 km (where the roving ADCP surveys took place). The tidal excursion distance based on these salinity profiles is approximately 8 km. Typically the longitudinal density gradient has been measured in past observations with similar river transport to be 1.2×10^{-3}kg/m^3/m and can play a strong role in the tidal straining process.

Time series of the vertical density profiles for the northwest and southeast stations are also shown in Figure 4.4. The time difference between each profiles is approximately 40

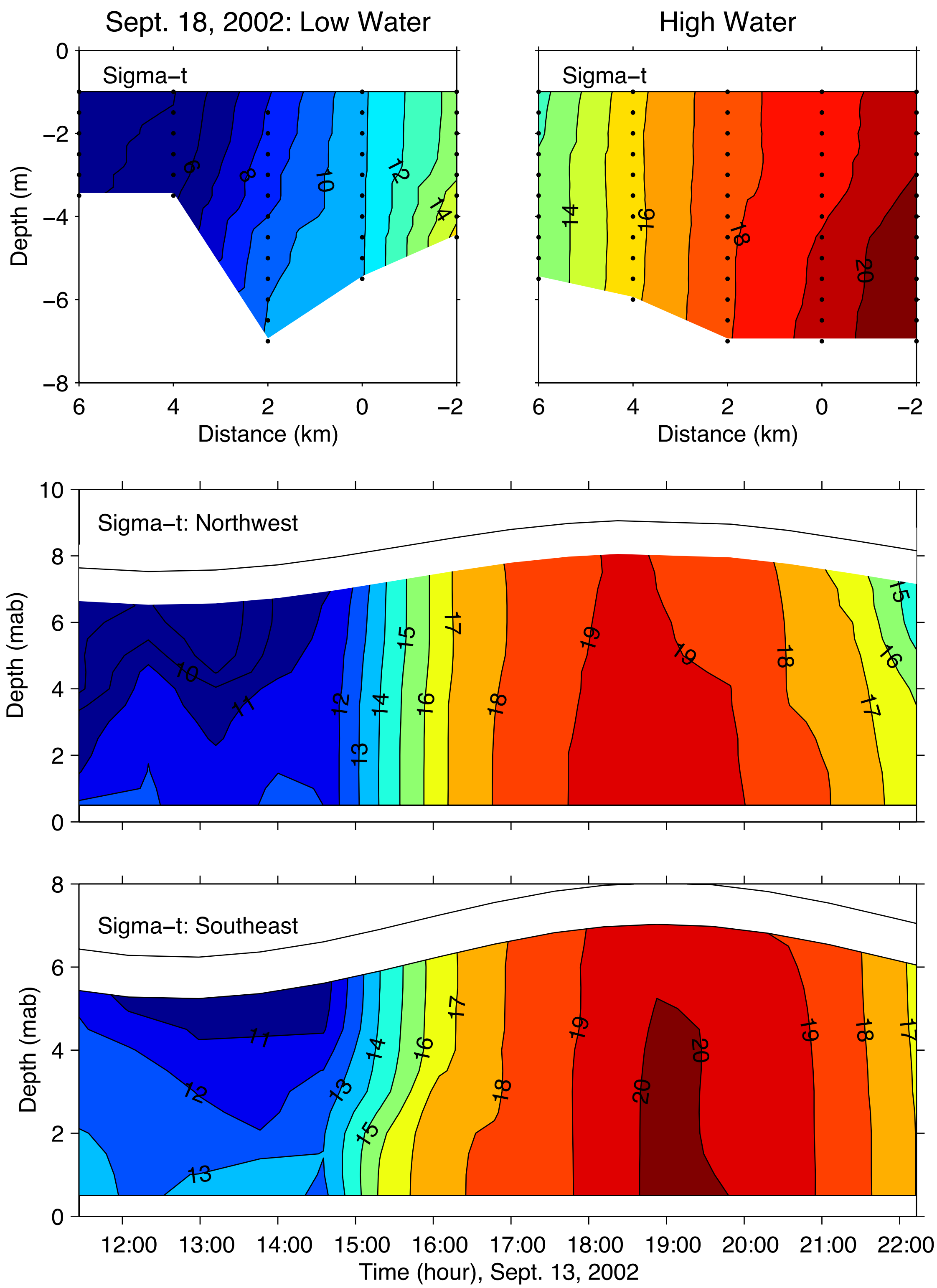

Figure 4.4: Density distribution along the CTD transect and time series at the two anchor stations.

min, which was the time it took to travel the 1.4 km distance separating the two stations. Both stations show more stratification during slack low water, which is then quickly mixed away at the onset of the flooding tide, becoming relatively homogeneous at high water. This is consistent with the strain induced periodic stratification (SIPS) process described by Simpson et al. (1990). The largest difference between these two stations is the greater amount of fresher water that exists at the northwest station during the ebb to low water tidal cycle. The northern side of the channel is deeper than the southern side which may be the result of scouring from the intracoastal waterway (refer to Figure 4.1) and this channel may contribute to the amount of freshwater on this side during the ebbing tide.

Surface density distributions interpolated over the zig-zag grid are shown in Figure 4.5 for different times in the tidal cycle. Each panel corresponds to approximately 40 min of time and so some tidal aliasing is incorporated into the data. The most striking feature evident is the latitudinal density gradient that exists during flood and ebb tide. During the flood tide, the water in the center of the channel has a higher density than along the coastal boundaries indicating that a residual flow outward may occur along the shoaling areas of the channel. For the ebb tide, the density distribution shows a higher density along the southern coastal boundary than along the northern boundary which is consistent with the CTD profiles in Figure 4.4. The latitudinal density difference at the surface is approximately 0.6 kg/m^3 for flood and $\sim$ 0.4 kg/m^3 for ebb. The CTD profiles in Figure 4.4 show that a greater lateral density gradient occurs at depth since more saline conditions are prevalent in the southeast station. During slack low water some surface latitudinal variations exist, indicating higher saline water stored over the shoaling area to the north. At the end of flood tide practically no latitudinal variations exist.

4.3.2 Tidal flow

Tidal flow plays a significant role in the dynamics of estuaries. The characteristics of tidal motion are strongly dependent on the shape of the estuary itself, in particular its width,

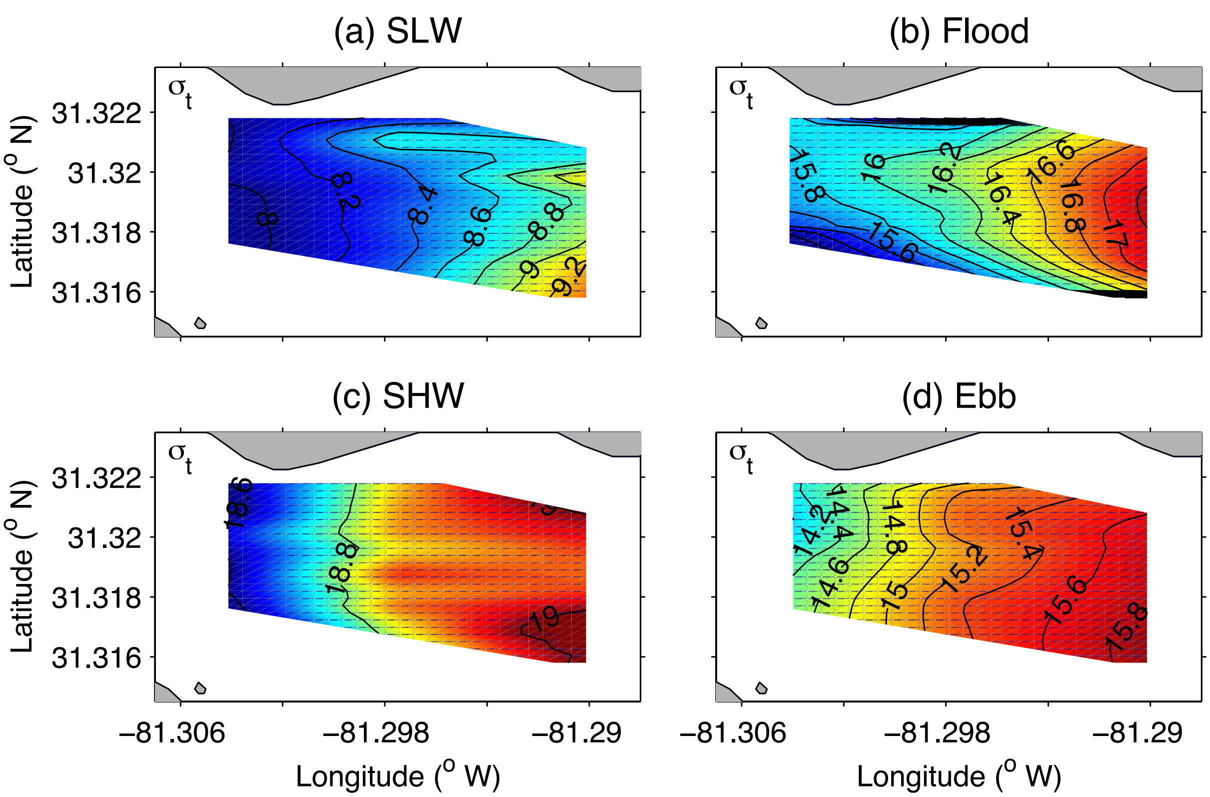

Figure 4.5: Horizontal density distribution with tidal period.

length, and bottom topography. Since estuarine environments are generally shallow compared to the tidal wave length, bottom friction can alter the tidal motion. Tidal energy is dissipated due to friction between the mean flow and the sea bed. This frictional damping is a non-linear process that depends on the square of the current speed and inversely on the depth. If there is a large amount of tidal energy dissipation, then the tidal wave becomes progressive and the amplitude and current may not be 90 degrees out of phase. In some extreme cases the maximum flood currents take place at high water, which also coincides with maximum salinity (Dyer, 1997). In the Altamaha River high tide occurs later for points further into the estuary and therefore can be described as a progressive wave over the whole estuarine domain.

Figure 4.6 shows the characteristics of the amplitude and phase of the M2 semidiurnal (T=12.42 hour) lunar tidal component as a function of space over the transect domain. As only 13 hours of data were collected only the M2 component was included in the analysis. The tidal ellipse shows that the flow pattern in the estuary is predominantly horizontal and somewhat aligned with the coastal boundaries. Maximum flows are predominantly in the northwest area as shown by the elongated ellipses. From the southeastern sampling region toward the northwest, the amplitude is increased from 45 cm/s to 55 cm/s, presumably due to changes in the water depth. The tidal phase over this short longitudinal section shows little variation except for the shoaling regions in both the north and south where the phase is significantly altered, presumably due to increased bottom friction.

Horizontal distributions of the surface, bottom and depth-averaged flows together with the M2 tidal constituent from depth-averaged data are shown in Figure 4.7. The surface flood flow shows slightly greater speeds in the center of the channel whereas the ebb flow is more concentrated on the northern shore. The near bottom flows are greatly reduced because of bottom friction, and show more lateral variability on ebb than on flood. The depth-averaged flow shows ebb-dominant flow (as the magnitudes are greater on ebb than on flood). This is caused by either the net river discharge or by the nonlinear interaction of the M2 tide

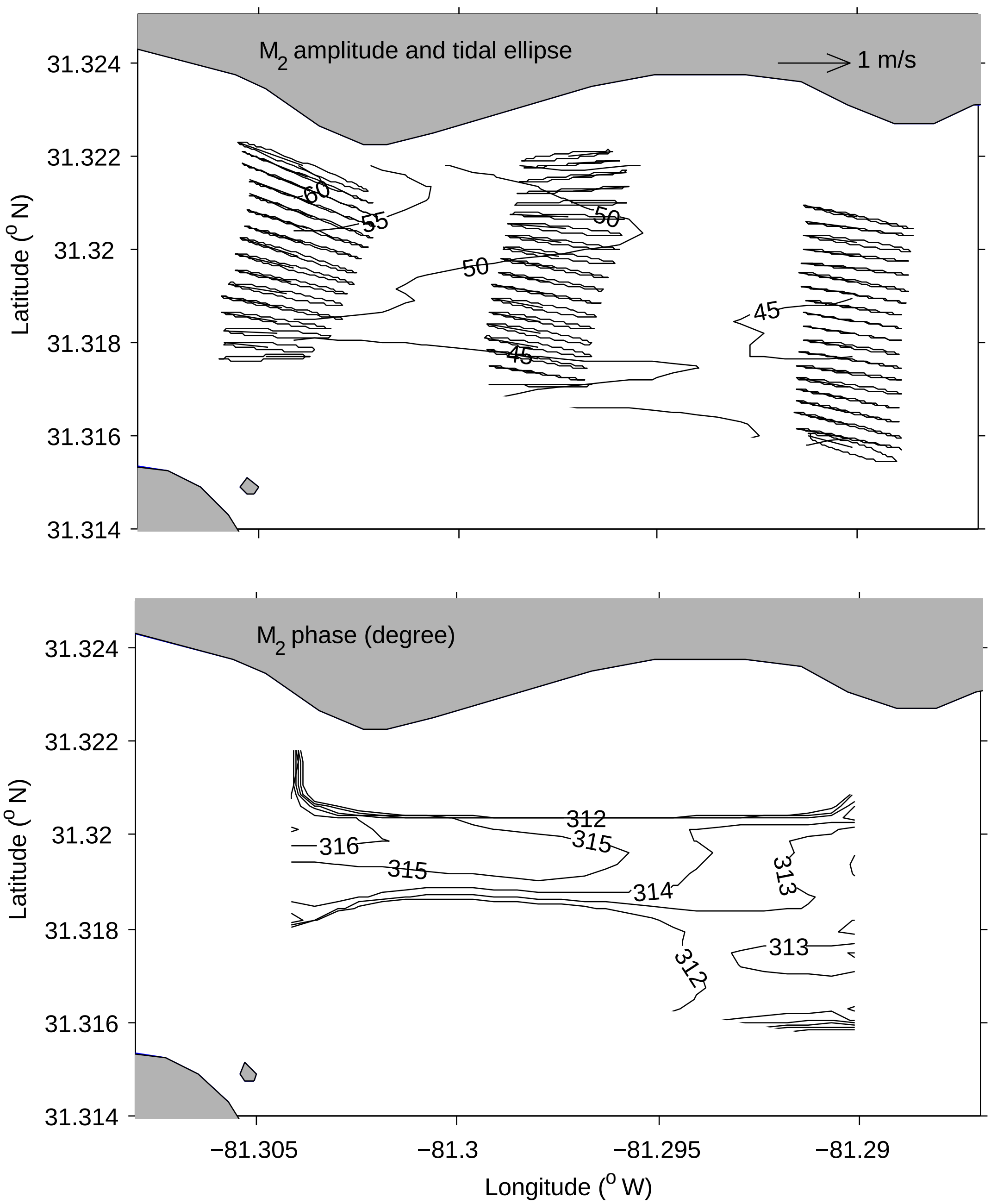

Figure 4.6: Tidal ellipse with amplitude and phase distribution of the M2 component. The phase is the degrees relative to Greenwich time.

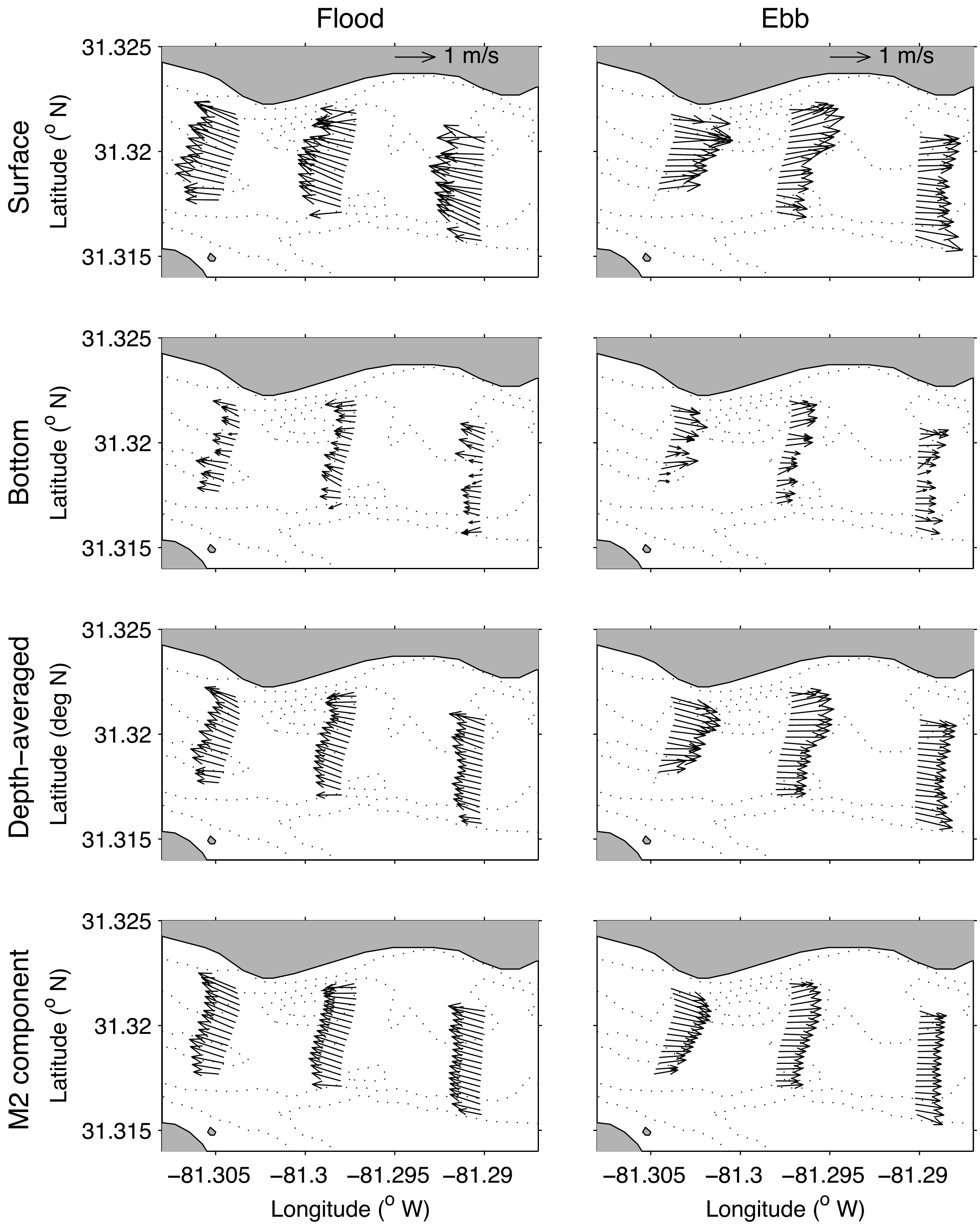

Figure 4.7: Horizontal flow at the surface, bottom, depth-averaged and M2 component during the flood and ebb tides. The surface layer indicates the first bin of the ADCP which is 2 meters below the surface, and bottom is taken from the last bin of ADCP data.

with bottom friction creating the M4 tidal harmonic that has twice the period of the M2 tide (Blanton et al., 2002). The M2 semidiurnal component, which represents a best fit to the time varying depth-averaged flow, smooths out the lateral and longitudinal variations. M2 flood is slightly greater than the depth-averaged flow, resulting in a positive (seaward) residual flow as will be shown. In contrast, the depth-averaged ebb flow is greater than the M2 component which will also result in a seaward residual flow.

4.3.3 Depth-averaged Residual Flow and Transport

The depth-averaged residual flow, $\hat{\mathbf{U}}_r(x_i, y_j, t)$, calculated from (4.2) is shown in Figure 4.8 over four stages of the tidal cycle. The most interesting thing to note is the residual seaward flow for both the flood and ebb tides and weaker landward flow during slack water. Generally speaking, the baroclinic flow is driven by the pressure gradient due to the longitudinal density gradient and traditionally it has been considered constant over tidal time scales. Recently Stacey et al. (2001) showed that the velocity scale for the baroclinic flow (modified here to include the density gradient rather than the salinity gradient) can be written as,

$$u_g \approx \frac{\frac{1}{\rho}\frac{\partial \rho}{\partial x} g H^2}{u_*}. \tag{4.5}$$

where H is a depth scaling and u_* is the friction velocity representing the turbulence levels and hence mixing. As the friction velocity increases, mixing increases and therefore the baroclinic flow decreases; as mixing decreases during slack water due to low flows and more stratified conditions the baroclinic flow increases. This scaling result is consistent with the results of Nunes-Vaz et al. (1989), who demonstrated that the baroclinic mass flux is greatest during the strongest stratification period which is at a time of minimum TKE. They further showed that the baroclinic-driven flow has a temporal variation that is consistent with the variations of turbulent mixing, which are at the tidal (M4 period) and spring-neap time scales.

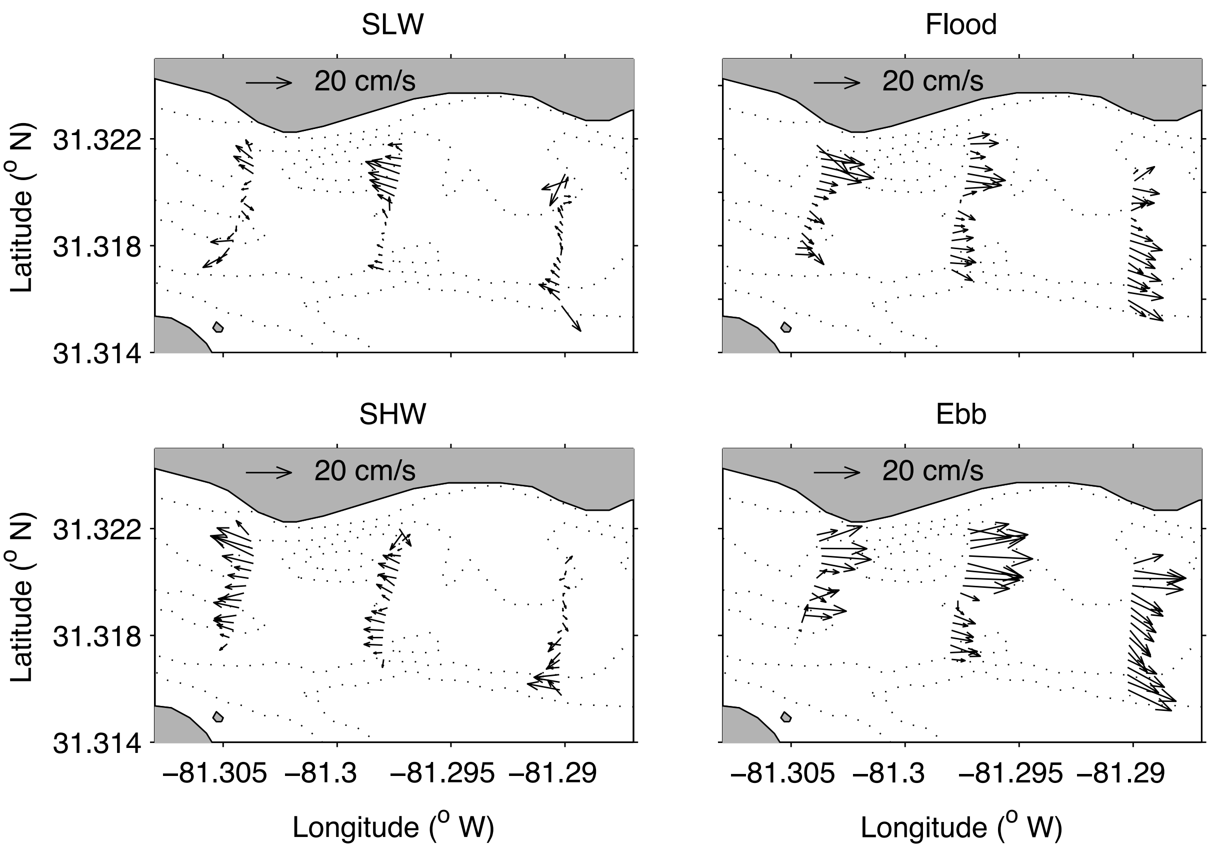

Figure 4.8: The horizontally and time varying depth-averaged residual flow.

The simplified momentum equation describing the barotropic flow is,

$$\frac{\partial U}{\partial t} = -\frac{1}{\rho}\frac{\partial p}{\partial x} + \frac{\partial}{\partial z}(\nu_t \frac{\partial U}{\partial z}) \tag{4.6}$$

where the Reynolds stresses have been parameterized in terms of the vertical mixing of momentum and shear. During the ebb tide, when mixing is weak ν_t is small as a result of increased stratification, therefore more shear develops, causing increased acceleration of the surface waters. On flood, as the stratification is destabilized, ν_t is large and so higher momentum surface waters are mixed down to the bottom thus increasing the near bed flows. Both the baroclinic and barotropic mechanism described create temporally varying residual flows that are dependent on the turbulence-enhenced mixing asymmetries and are thus not easily separated.

Figure 4.8 also shows some latitudinal variation of the residual flow. Maximum flows of 20 cm/s occur along the northern side of the channel for sections A and B and on the southern side at section C. This is more apparent in Figure 4.9 where the residual volume transport, estimated using (4.4), is shown. The transport is more enhanced where the depths are greatest. During slack water, the data shows that a significant amount of transport is upstream which has implications for moving particulates and biological organisms from the coastal ocean into the estuarine environment.

The time variability of the total and residual flow speed and transport are shown in Figure 4.10 over the tidal cycle sampled. The total transport shows that the tides move a significant amount of water into and out of the estuary. For each of the sections the streamwise transports are not that different, having the same phase and similar magnitudes (ranging from -1800 m^3/s to a maximum of 2000 m^3/s on ebb). The depth- and latitudinally-averaged flow speeds range from -0.6 m/s to 0.8 m/s. The residual volume transport (and flow) show positive (seaward) values during the flooding and ebbing tide and negative (landward) values during slack water. The residual flow speeds are a maximum of 15 cm/s. This temporal variability is consistent within all cross sections. Clearly the residual flow is not constant over the tidal time period. It should be noted that traditionally residual flows are computed

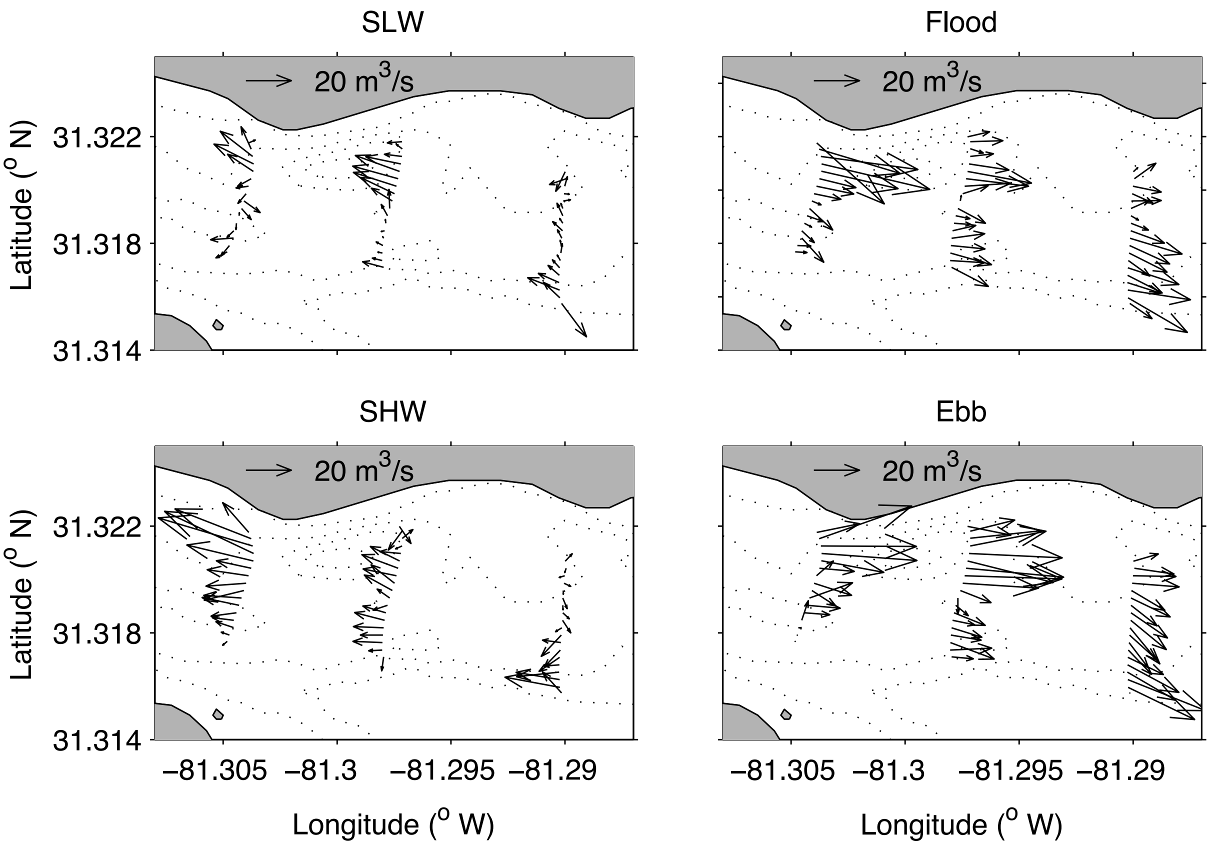

Figure 4.9: The horizontally and time varying net transport through a latitudinal grid size of 30.8 m.

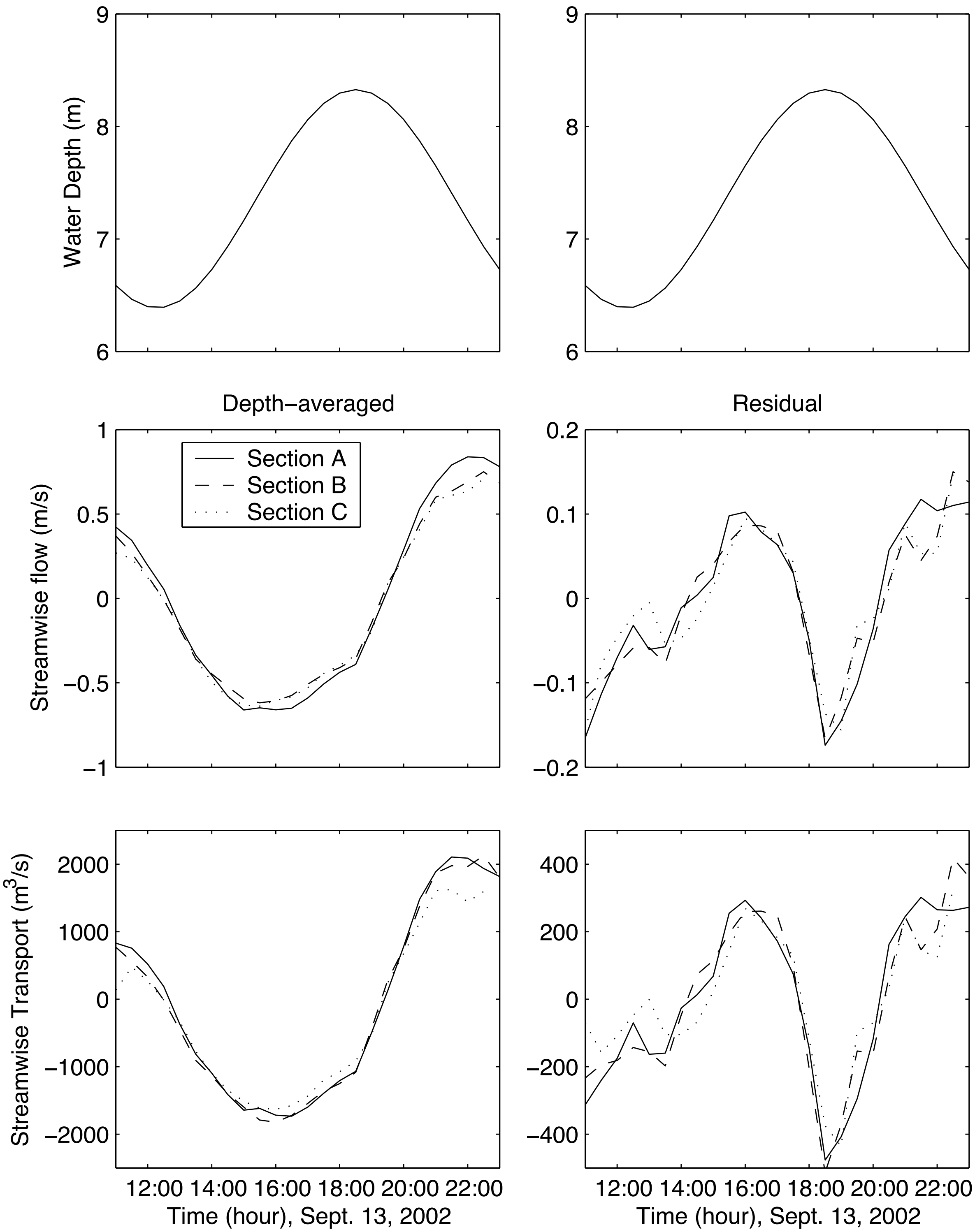

Figure 4.10: Time variation of the depth- and latitudinally-averaged streamwise flow and the total net transport together with their residuals for each cross section.

by low-pass filtering or tidally averaging and it is possible that these methods remove any temporal variability that exists on tidal time scales. Since these measurements were carried out during a neap tide when presumably mixing is weak we expect the residual flow to be maximal at this time. Clearly comparisons with a spring tide is necessary.

4.3.4 Depth-dependent Residual Flow

The depth-dependent residual flow calculated using equation (4.3) is shown in Figure 4.11 for each cross section during four phases of the tide: slack low water, flood, slack high water and ebb. In these figures, the current velocity was resolved into along and cross channel components. The angle of the x-axis (Eastward) was approximately -17 degrees. The flow denoted by the color blue corresponds to landward flow and red colors correspond to seaward flow (out of the estuary); arrows indicate cross channel flows with arrows pointing to the right representing northward flow and arrows pointing to the left as southward flow. Along section A, there is a deep hole scoured along the northern side of the channel and most of the main flow is concentrated within it. The residual flows during flood and ebb tide are mostly concentrated in the deepest part of the channel corresponding to net outward flow. During the flood tide the residual flow is predominantly in the main channel flowing seaward with stronger flows near the surface and a strong secondary circulation to the south; During the ebb tide the secondary circulation is predominantly to the north. The residual flow during slack low water appears to have strong flow into the estuary at depth and flow out of the estuary toward the shoaling region to the south. The cross-sectional velocities for this flow is northward in the deepest part and southward onto the shoaling banks, causing divergence within the center of the channel. During slack high water the net flow landward extends throughout the water column and a similar divergence in the cross sectional flow is observed.

a)

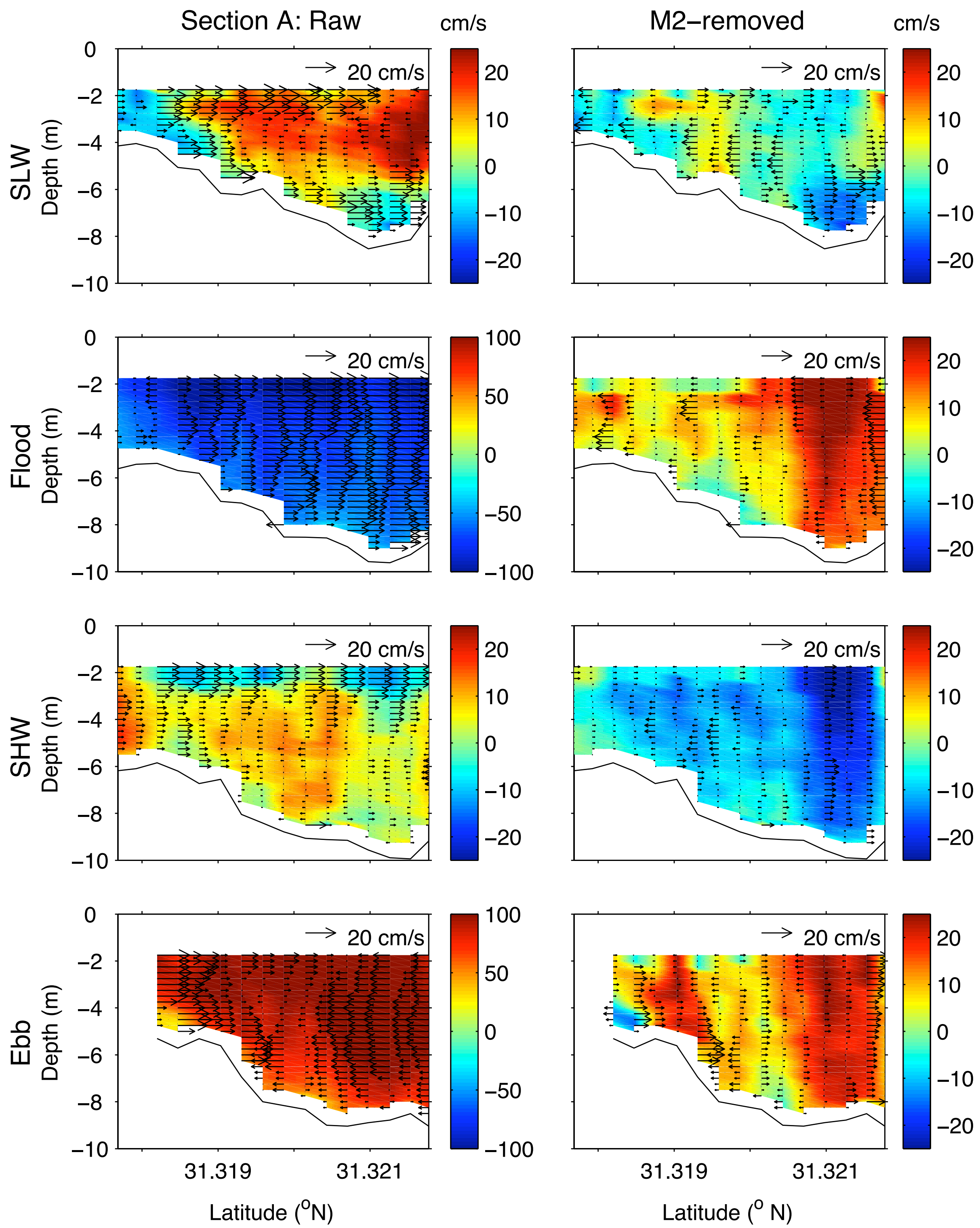

Figure 4.11: Mean flow and residual circulation across a) section A, b) section B and c) section C.

b)

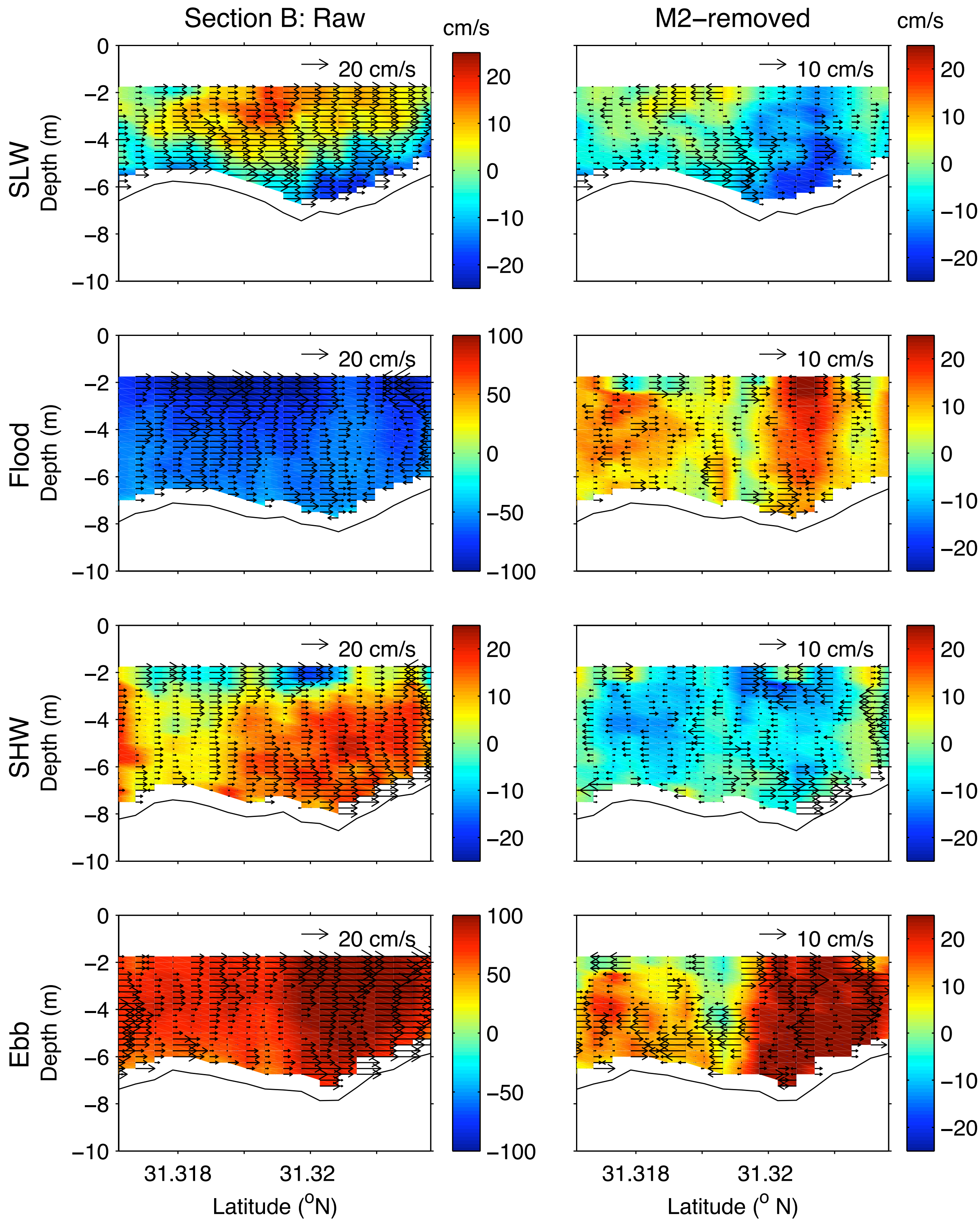

Figure 4.11 continued.

c)

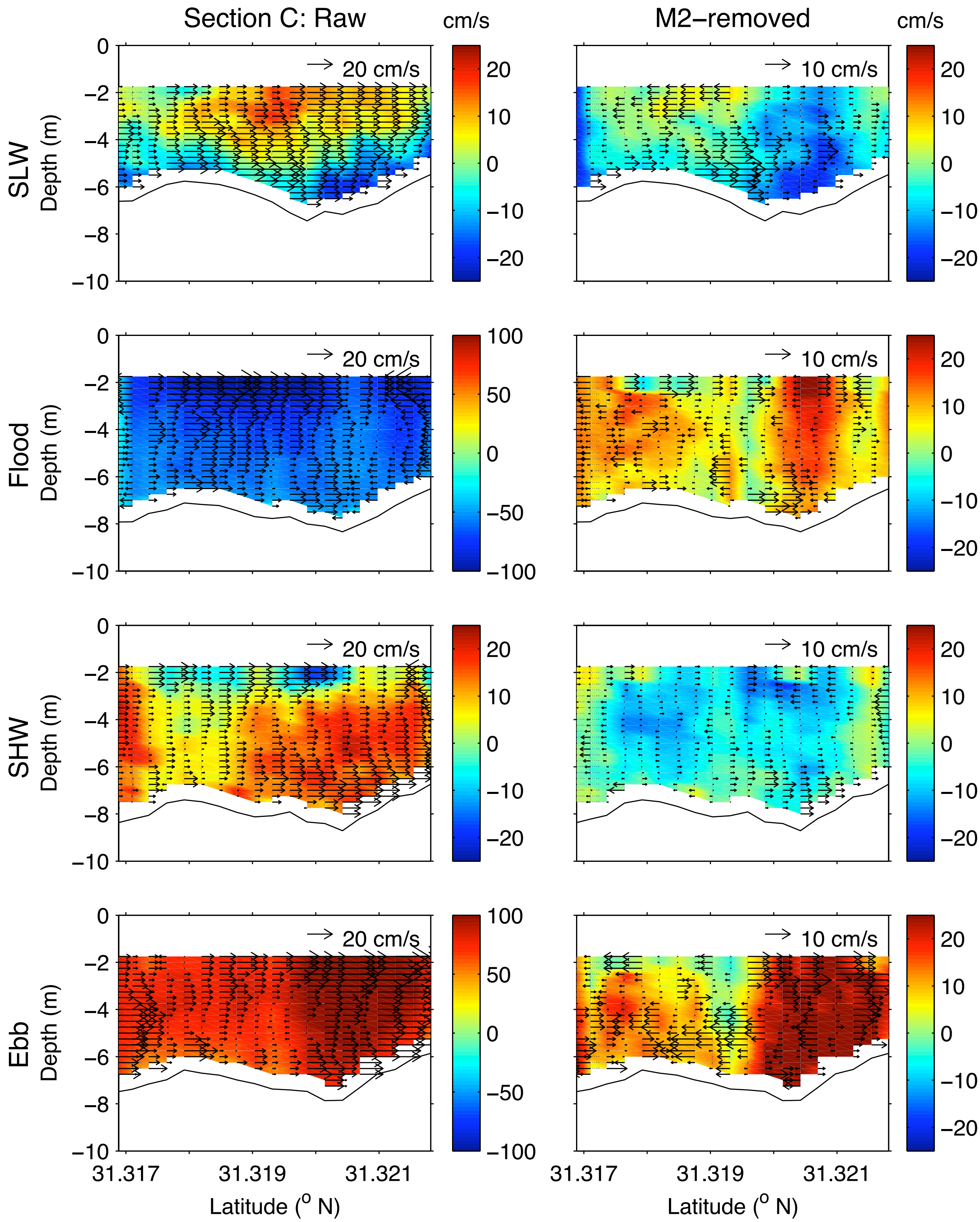

Figure 4.11 continued.

The general flow characteristics in sections B and C remain somewhat similar to that in section A. However, the cross sectional water depth becomes more uniform compared to that in section A. Also, the cross sectional secondary flows become more enhanced.

4.4 Discussion and Conclusion

The estuarine residual circulation and its water volume transport in the Altamaha River Estuary, GA, was described based on 13-hour roving ADCP and CTD profile data sets. The harmonic analysis method was used to separate the tidal and residual components from the depth-averaged flow and depth dependent flow. Net transport by the residual flow was also estimated to see circulation changes over the tidal cycle. The semidiurnal M2 component provided a good fit for the depth-averaged and depth-dependent current data. Tidal amplitude and phase and time variation of the residual flow were presented to show the temporal characteristics with possible connections to turbulence. The water volume transport by residual flow showed that the residual circulation is a result of combined barotropic- and baroclinic-driven flow and has a periodic tidal characteristic.

Tidal forcing is one of the major determining factors in the characteristic of an estuarine circulation system. This is because its magnitude is not only one order of magnitude larger than other forces (for example wind-driven force), but also because it produces several combined effects - i.e. nonlinear friction effect with the bottom, creation of internal waves in the layered sea and periodic stratification. Applying a least squares fit of the semidiurnal principal lunar (M2) component to the depth-averaged flow data, showed that the fitted values explained over 95 percent of the total variance of the depth-averaged flow data. According to the tidal ellipse, the flow was essentially back-and-forth following the coastal channel. The length of the major axis of the ellipse varied from 60 to 90 cm/s and minor axis was 8 to 12 cm/s. The amplitude of the M2 component increased slightly from 45 to 60 cm/s in the landward direction, and most of the sampled area was in phase except toward the shores.

The spatial density gradient is the main source of the baroclinic driven flow and can be a significant contributor to the residual flow especially when the tide-driven barotropic effect is minimal during slack water. The density distribution along the channel showed much variability over the tidal cycle with a larger horizontal gradient at slack low water compared to that at slack high water. Without other external forces, i.e. wind or high river discharge, the baroclinic force can play an important part in controlling flow into the estuary since tide-driven barotropic forcing at slack water is a minimum as the turbulent friction velocity becomes almost zero. As a result, strong landward residual flow appeared during both slack tides because of low flows and hence low turbulence and mixing levels. However, during slack low water when the stratification was greatest, latitudinally averaged levels were much smaller than during slack high water when the water column was well mixed. The residual flow pattern also showed some depth dependence with higher levels in the deeper parts of the channel. This may correspond to the fact that baroclinic flows also increase with increasing depths. During the ebb tide the residual flow was slightly stronger than that for flood with both showing seaward flows with magnitudes approximately 20 cm/s. Thus the time variation of the residual flow had an M4 periodic characteristic.

In the depth-dependent study it was necessary to fit an M2 tidal cycle to flow velocities at each depth since the flow was highly sheared due to bottom friction effects. After removing the M2 tide at each depth it was found that the surface residual flow during flood and ebb tides were similar in magnitude and that the near bottom velocity was stronger during the ebb tide, which led to the different depth-averaged residual flows. The weaker bottom residual flow during the flood tide could be interpreted as resistance to the river flow. This characteristic is evident more along sections B and C where there was little latitudinal depth variations. Along section A the residual flows were concentrated in the deeper parts of the channel with more uniform flow during ebb and highly sheared flow on flood. This flood/ebb asymmetry created the ebb-dominant flow and the seaward residual flow for both flood and ebb tides.

Acknowledgments. This work was supported by the NSF (OCE-9982133) as part of the Georgia Coastal Ecosystems Long Term Ecological Research (GCE-LTER) project (http://gce-lter.marsci.uga.edu/lter/index.htm) and by the University of Georgia Research Foundation, Faculty Research Grant program . The authors would like to thank Captain Raymond Sweatte and the crew of the R/V Savannah for their support during the roving ADCP and CTD surveys over the 13 hour period.

Chapter 5

GENERAL CONCLUSIONS AND RECOMMENDATIONS

Estuarine physical environmental factors such as sea surface waves, turbulent flow, and residual circulation were studied using several observed data sets and modeling approaches in the Altamaha River Estuary, GA. In the surface wave study, the temporal and spatial wave energy variations and deformation by current, bathymetry, and wind were studied over a region spanning the midshelf of the South Atlantic Bight to the Altamaha River Estuary. Turbulent flow characteristics included Reynolds stress, turbulent kinetic energy (TKE), wave-turbulence interaction, shear production (P), dissipation rate (ϵ), buoyancy flux (B), and TKE budget including a numerical simulation using a one-dimensional turbulence model. Estimation of the tidal flow, residual flow and volume transport from a roving acoustic Doppler current profiler data were performed in a circulation study.

In chapter 2, the surface wave energy propagation and deformation were described by analyzing field observation data obtained from bottom mounted pressure and flow sensors together with numerical model runs. What we found from the observed data was that wave heights on the shelf region correlated with wind observations and that the wave heights were attenuated by at least 75 %, possibly because of bottom friction, as they propagated from the midshelf (at 20 m depth) to the inner shelf (at 10 m depth) a distance of 15 km. Most of the wave energy is incident from the easterly direction except for occasional north- and south-easterly propagating waves. The wave energy within the estuary became periodic in time showing high wave energy from the flood to the high water phase of the tide and very low wave energy from ebb to the low water phase.

The periodic modulation of the surface wave energy inside the estuary was a direct result of enhanced depth and current-induced wave breaking that occurred at the ebb shoaling region surrounding the Altamaha River mouth at longitude 81.23 °W. Modeling results with STWAVE showed that depth-induced wave breaking was significantly more important during the low water phase of the tide than current-induced wave breaking during the ebb phase of the tide. During the flood to high water phase, wave energy propagated into the estuary. Temporal and modeled measurements of the significant wave height within the estuary showed a maximum wave height difference of 0.4 m between SHW and SLW. The maximum significant wave height, however was almost always 1- 2 hours before the SHW in both observed and model output data. This kind of flood/ebb asymmetry in the wave field is a direct result of the bar that surrounds the mouth of the Altamaha River. There is no bathymetric channel connecting the Altamaha River to the coastal ocean since it has a high sediment load and the the river is not dredged. Thus it is expected that similar estuaries would produce similar flood/ebb asymmetries in the wave field.

Surface waves in the shallow area can alter the bottom friction felt by the current, since the orbital motions become attenuated with depth and then interact with the bottom boundary layer. According to the bottom boundary layer model results, wave-current interactions can change the hydraulic bottom roughness, which results in an enhanced bottom friction coefficient. With a flat bottom with silt (grain diameter 20 μm) the hydraulic roughness is $z_o = d/30 = 6.7 \times 10^{-7}$m. By including wave-current interaction effects associated with our observations, there is an increase in the apparent bottom roughness up to a maximum value of $z_{o_a} \sim 8.5 \times 10^{-7}$ m during the flooding to high water phase of the tide. This wave-enhanced bottom friction can have a significant damping effect on the circulation in enclosed bays and coastal shorelines and future modeling results recommended below would asses its importance.

In chapter 3, the turbulent flow characteristics during two different river discharge periods were described by comparing several parameters showing the turbulent flow activities, and also by numerical simulation runs. Based on the observed data obtained from maximum and minimum river discharge periods, it was found that variables such as the Reynolds stress, shear production, dissipation rate and buoyancy flux, were deformed by the effects of river discharge, tidal straining of the density field, wind and wave effects. When the river discharge was small there was a long tidal excursion distance (8 km) with a well mixed water column and a horizontal density gradient of 1.5×10^{-3} kg/m^3/m. The current structure showed maximum speeds at the surface that decreased with depth for both the flood and ebb tides. When the river discharge was high, the flow structure and density distribution were very different. The ebb flow became much stronger by the increased river-driven barotropic factor. The net residual outflow was also enhanced. The salinity difference between the surface and bottom layers became maximum on the flood to high water to ebb tide with a 20 psu difference between surface and bottom.

The high river discharge period of 2003 produced a significant buoyancy forcing that retarded the surface inflow during the flooding tide and prolonged the surface outflow during the ebbing tide. Northwesterly winds was also found to play a key role in retarding the surface waters. Comparing the water column stability using the gradient Richardson number distribution for 2001 and 2003, showed a different shape for the two cases. During the low discharge observation (2001) stability was predominantly toward the end of the ebb tide and on into the start of the flooding tide when stratification was greatest. For the high river discharge period strong stratification from flood to ebb tide created very stable conditions.

The Reynolds stress followed the tidal cycle with positive values for the ebb, negative values for the flood, and zero values for slack water. The observed stress ranged from -2.0 to $\sim 1.0 \times 10^{-3}\mathrm{m}^2\mathrm{s}^{-2}$ for 2001 and -2.0 to $\sim 6.0 \times 10^{-3}\mathrm{m}^2\mathrm{s}^{-2}$ for 2003. The Reynolds stress for flood tide in 2001 was always higher and more erratic than those observed for ebb tide even though the mean tidal flow was slightly ebb-dominated. Regarding this asymmetry structure of the stress, two possible mechanisms were suggested: (1) wave-induced bottom roughness change and (2) asymmetry of the pressure gradient by the barotropic and baroclinic force. After correcting for surface waves using a linear filtration method (which gave reductions up to $2 \times 10^{-3}\mathrm{m}^2/\mathrm{s}^2$), the TKE levels became similar in magnitude for ebb and flood tide . The TKE variation follows an M4 periodic pattern. For 2003, the TKE time series at 1.4 mab was always greatest on the ebb tide with maximum values $\sim 2 \times 10^{-2}$ $\mathrm{m}^2\mathrm{s}^{-2}$, which was caused by the increased flow strength and duration time during the ebb tide.

Buoyancy flux estimates for when the water column was essentially homogeneous and dependent on the longitudinal density gradient, showed a common pattern in that the flood tide was an energy source (negative sign) and the ebb was an energy sink (positive sign). This implies that the flood tide was inducing instabilities and the ebb was tending to stabilize. For a vertically stratified layer that varies with time, the inhomogeneous and nonsteady term made a significant contribution to the variation of buoyancy flux structure, showing a magnitude of 4×10^{-5}. The flux Richardson number in general was 0.1 on ebb and 0.03 on flood in 2001. The estimated minimum mixing rate in the near bottom was about 55 cm^2/s on flood, and 15 cm^2/s on ebb for a given stratification of $N^2 = 0.002 s^{-2}$ and energy dissipation of $\epsilon = 1.0 \times 10^{-4}$ W/kg. The buoyancy flux estimate in the Altamaha River is unique in that the longitudinal density gradient is rather high compared to other estuaries and therefore can contribute a modest energy source or sink effect. The TKE budget analysis showed that the TKE production and dissipation are in general not in balance differing by a factor of 2. This implies that transport mechanisms must play a role in the conservation of TKE.

The numerical modeling experiment was used to obtain 2D variability of the Reynolds stress, TKE, shear production and dissipation despite its poor performance in predicting tidal time scale variations in 2001 and phasing of magnitudes for 2003 at a specific depth. The model study, however was used to identify characteristics in the bottom boundary layer that can then be used to address questions about the flow. For example, during high river discharge when the water column is highly stratified does the pycnocline act like an internal boundary? Future experiments outlined below could be carried out to address this effect.

In chapter 4, the estuarine residual circulation and water volume transport were estimated using 13-hour roving ADCP, CTD profile data, and a harmonic analysis method. The semidiurnal M2 component of the tide was fitted to the depth-averaged current data, covering over 95 percent of the variance of the flow data. Tidal motion was aligned with the channel showing 60 to 90 cm/s of the major axis length of the tidal ellipse and 8 to 12 cm/s of the minor axis length. The amplitude of the M2 component increased from 45 to 60 cm/s in the landward direction, and the phase over the area sampled with the roving ADCP was fairly constant except near the shores. The surface flow for the flood and ebb tide along sections B and C was similar in magnitude, however bottom velocities were different showing a stronger ebb tide, which led to flood/ebb asymmetries in the depth-averaged flow. This difference produced the ebb-dominant flow and the seaward residual flow for both flood and ebb tides. The semidiurnal tidal flow and thus net transport in shallow water was also very sensitive to the water depth.

The residual volume transport showed that the residual circulation may be the result of barotropic- and baroclinic-driven flow and had a periodic tidal variation. Tidal excursion distances were approximately 7-8 km. The density distribution along the channel was compressed during the flood to slack high water tide, while it was uncompressed during the ebb and slack low water time. Strong landward residual flow appeared during both slack waters, which was considered to be a baroclinic effect because the velocity hence turbulence becomes minimum or almost zero during these periods. The stronger residual flow was found in the deeper area and the temporal variation had an M4 tidal component. The net volume transport showed seaward movement in all sections with a depth-dependent pattern. What is unique with these measurements is that they are obtained along the channel and therefor spatial variability due to bathymetric effects can be seen and provides an indication for instrument placement in future experiments.

The physical processes of the Altamaha River Estuary are driven by complicated processes such as turbulence, waves, water mass mixing, bottom friction, freshwater input, pressure and density gradient, tidal currents, and irregular boundaries and bathymetry. Whenever a new observation technique comes out in the ocean, some issues have been solved, and new questions have also been developed. Although this research result could not show a complete understanding of the estuarine physical system, it is hoped that the contents in this dissertation would contribute to our knowledge of the estuarine system.

5.1 Future Studies and Recommendations

For future experiments in the Altamaha River estuary some recommendations and suggestions are given that would build on the results of this thesis. Measurements of the small scale fluid motions like waves and turbulence are of interest in shallow coastal areas and estuaries because they have helped understand the physical processes governing second order momentum and energy conservation laws and because of their effects on plankton dynamics including ecological studies. In our study the major objectives were met effectively using point measurements of turbulence data, however, their distribution and variation over the whole water column were not obtained. In order to examine the transport of turbulent kinetic energy and possible relations with stratification, a two-dimensional view is needed which can also be used to compare with model results. At least two horizontally separated stations along the channel would be required with each station having surface and bottom CTD measurements for estimating the horizontal and vertical density gradients and a beam-coordinate sampling strategy for acoustic doppler current profilers having small variations of pitch, roll and heading values. In addition, if a third transducer can be vertically oriented to recover the vertical velocities then the large eddy approach of Gargett (1988) can be used to recover the turbulent kinetic energy dissipation rate. The physical processes governing the turbulent characteristics as a function of time can then be carried out. In addition to turbulence measuring devices, it is recommended that a momentum balance be carried out to quantify and compare the barotropic and baroclinic forces and their competing effects. This would require two tide stations along the Altamaha River.

Regarding wave propagation and energy losses due to bottom friction it is recommended that directional wave measurements be made on the continental inner and mid shelf so that energy levels for waves propagating in the same direction can be compared. Also, it would be very interesting to couple a two dimensional depth-averaged current model to the wave model for further wave-current-bathymetry interaction studies. Even though a uniform current field showed the effects of wave energy deformation by currents, it is possible that the wave energy distribution was under- or over-estimated over the model domain. With the resulting wave field quantified more accurately, parameterizations in terms of an apparent production of energy or in terms of an enhanced bottom friction coefficient could then be implemented into the 2D model for assessing changes in coastal flows.

Another important future study for this highly *compressed* estuarine environment is to investigate the secondary circulation in more detail because our results indicate that there are important cross channel density gradients during certain phases of the tide. In particular, detailed measurements of the cross channel density and velocity structure is necessary over separate spring and neap cycles in order to quantify cross-channel baroclinic effects. In addition to roving data it is necessary to also have simultaneous long term moored instruments.

Bibliography

Agrawal, Y. C. and Aubrey, D. (1992). Velocity observation above a rippled bed using laser Doppler velocimetry. *Journal of Geophysical Research*, 97:20249–20259.

Alber, M. and Sheldon, J. E. (1999). Use of a date-specific method to examine variability in the flushing times of Georgia estuaries. *Estuarine, Coastal and Shelf Science*, 49:469–482.

Atkinson, L. P., Blanton, J. O., and Hains, E. B. (1978). Shelf flushing rates based on the distribution of salinity and freshwater in the Georgia Bight. *Estuarine, Coastal Marine Science*, 7:465–472.

Atkinson, L. P., Lee, T. N., Blanton, J., and Chandler, W. (1983). Climatology of the southeastern United States continental shelf waters. *Journal of Geophysical Research*, 88:4705–4718.

Batchelor, G. K. (1951). *The Theory of Homogeneous Turbulence.* Cambridge Univ. Press, New York.

Battjes, J. and Janssen, J. (1978). Energy loss and set-up due to breaking of random waves. In *Proc. 16th Coast. Eng. Conf., ASCE, 569-587.*

Bendat, J. S. and Piersol, A. G. (1971). *Random Data: Analysis and Measurement Procedures.* Wiley-Interscience, New York.

Bender, L. C. and Wong, K.-C. (1993). The effect of wave-current interaction on tidally forced estuarine circulation. *Journal of Geophysical Research*, 98:16521–16528.

Benilov, A. Y. (1978). Error of the method of linear filteration in the analysis of random field fluctuations of the near-water atmospheric layer and the upper ocean layer. *Oceanology*, 18:17–20.

Blanton, J. O. (1981). Ocean current along a nearshor frontal zone on the continental shelf of the southeastern United States. *Journal of Physical Oceanography*, 11:1627–1637.

Blanton, J. O. and Atkinson, L. P. (1983). Transport and fate of river discharge on the continental shelf of the southeastern United States. *Journal of Geophysical Research*, 88:4730–4738.

Blanton, J. O., Lin, G., and Elston, S. A. (2002). Tidal current asymmetry in shallow estuaries and tidal creeks. *Continental Shelf Research*, 22:1731–1743.

Bowden, K. (1983). *Physical Oceanography of Coastal Waters*. Ellis Horwood Ltd.

Burchard, H. and Baumert, H. (1995). The performance of a mixed-layer model based on the k-ε turbulence closure. *Journal of Geophysical Research*, 100:8523–8540.

Burchard, H., Bolding, K., Rippeth, T. P., and Stips, A. (2002). Microstructure of turbulence in the northern Northern Sea: a comparative study of observation and model simulations. *Journal of Sea Research*, 47:223–238.

Burchard, H., Bolding, K., and Villarreal, M. R. (1999). GOTM-a general ocean turbulence model: Theory, application and test cases. Technical report, Report EUR 18745 EN, European Commission.

Burchard, H., Petersen, O., and Rippeth, T. P. (1998). Comparing the performance of the Mellor-Yamada and the $k-\varepsilon$ two-equation turbulence models. *Journal of Geophysical Research*, 103:10543–10554.

Canuto, V. M., Howard, A., Cheng, Y., and Dubovikov, M. (2001). Ocean turbulence I: One-point closure model-momentum and heat vertical diffusivities. *Journal of Physical Oceanography*, 31:1413–1426.

Chen, C., Zheng, L., and Blanton, J. (1999). Physical processes controlling the formation, evolution, and perturbation of the low-salinity front in the inner shelf off the southeastern United States: A modelling study. *Journal of Geophysical Research*, 104.

Cialone, M. A. and Thompson, E. F. (2003). Wave climate and littoral sediment tranport potential, long beach island, new jersey. Technical report, ERDC/CHL TR-00-21, U.S. Army Engineer Research and Development Center,Vickburg, MS.

Dame, R., Alber, M., Allen, D., Mallin, M., Montague, C., Lewitus, A., Chalmers, A., Gardner, R., Gilman, C., Kjerfve, B., Pinckney, J., and Smith, N. (2000). Estuaries of the South Atlantic coast of North America: Their geographical signatures. *Estuaries*, 23:793–819.

DiIorio, D. and Kang, K. (2003). Some Physical factors that affect turbulent mixng in Altamaha Sound, Georgia. In Hatcher, K. J., editor, *Proceedings of the 2003 Georgia Water Resources Conferences*, pages 735–738. April 23-24, 2003, at the University of Georgia, Athens, GA.

Dyer, K. R. (1997). *Estuaries: A Physical Introduction*. John Wiley and Sons.

Foreman, M. (1979-1996). Manual for Tidal Currents Analysis and Prediction. Technical report, Institute of Ocean Sciences, Patricia Bay Sidney, British Columbia.

Gailani, J. Z., Smith, J. W., Kraus, N. C., McGee, D. D., Hands, E. B., Mayers, C. J., Moritz, H. R., Siipola, M. D., Slocum, D. B., Byrnes, M. R., Li, F., Dibble, T. L., Hollings, W. H., Lund, C., Sollitt, C. K., and Standy, D. (2003). Monitoring dredged material disposal at mouth of Columbia River, Washington/Oregon, USA. Technical report, ERDC/CHL TR-03-05, U.S. Army Engineer Research and Development Center, Vickburg, MS.

Gargett, A. (1988). A large eddy approach to acoustic remote sensing of turbulent kinetic energy dissipation rate. *Atmosphere-Ocean*, 26:483–508.

Gargett, A. (1999). Velcro measurement of turbulent kinetic energy dissipation rate. *Journal of Atmospheric and Oceanic Technology*, 16:1973–1993.

Gaspar, P., Gregoris, Y., and Lefevre, J.-M. (1990). A simple eddy kinetic model for simulations of the oceanic vertical mixing: Test at station papa and long-term upper ocean study site. *Journal of Geophysical Research*, 95:16179–16193.

Gonzalez, F. I. (1984). A case study of wave-current-bathymetry interactions at the Columbia River Entrance. *Journal of Geophysical Research*, 14:1065–1078.

Grant, H., Stewart, R., and Moillet, A. (1962). Turbulence spectra from a tidal channel. *Journal of Fluid Mechanics*, 12:241–268.

Grant, W. D. and Madsen, O. S. (1979). Combined wave and current interaction with a rough bottom. *Journal of Geophysical Research*, 84:1797–1808.

Grant, W. D. and Madsen, O. S. (1986). The continental-shelf bottom boundary layer. *Annual Review of Fluid Mechanics*, 18:265–305.

Green, M. O., Rees, J. M., and Pearson, N. D. (1990). Evidence for the influence of wave-current interaction in a tidal boundary layer. *Journal of Geophysical Research*, 95:9629–9644.

Gregg, M., Peters, H., Wesson, J., Oakey, N., and Shay, T. (1985). Intensive measurements of turbulence and shear in the Equatorial Undercurrent. *Nature*, 318:140–144.

Gutzler, D. S. (2004). An index of interannual precipitation variability in the core of the North American Moonsoon region. *Journal of Climate*, 17:4473–4480.

Guza, R. T. and Thornton, E. B. (1980). Local and shoaled comparisons of sea surface elevation, pressure, and velocities. *Journal of Geophysical Research*, 85:1524–1530.

Hansen, D. V. and Rattray, M. (1965). Gravitational circulation in straits and estuaries. *Journal of Marine Research*, 23:104–122.

Hir, P. L., Roberts, W., O.Cazaillet, Christie, M., Bassoullet, P., and Bacher, C. (2000). Characterization of intertidal flat hydrodynamics. *Continental Shelf Research*, 20:1433–1459.

Hollibaugh, J. T. (1999). 1999 georgia coastal ecosystem LTER proposal. Department of Marine Sciences, University of Georgia.

Horikawa, K. (1978). *Coastal Engineering: An Introduction to Ocean Engineering*. John Wiley & Sons, New York.

Ianniello, J. P. (1977). Tidally induced residual currents in estuaries of constant breadth and depth. *Journal of Marine Research*, 35:755–786.

Ianniello, J. P. (1979). Tidally induced residual currents in estuaries of variable breadth and depth. *Journal of Physical Oceanography*, 9:962–974.

Jay, D. A. (1991). Estuarine salt conservation: A lagrangian approach. *Estuarine, Coastal and Shelf Science*, 32:547–565.

Jay, D. A. and Smith, J. D. (1990). Circulation, density structure and neap-spring transitions in the Columbia River Estuary. *Progress in Oceanography*, 25:81–112.

Kagan, B., Tejedor, L., Alvarez, O., Izquierdo, A., Tejedor, B., and Mananes, R. (2001). Weak wave-tide interaction formulation and its application to Cadiz Bay. *Continental Shelf Research*, 21:697–725.

Kang, K. and DiIorio, D. (2004). Depth- and current-induced effects on wave propagation into the Altamaha River Estuary, Georgia. *Estuarine, Coastal and Shelf Science*. submitted in Dec 2004.

Kelley, J., Davis, C., and Cibik, S. (1998). Conceptual food web model for Cape Cod Bay, with associated environmental interactions. Technical report, Boston: Massachusetts Water Resources Authority, Environmental Quality Department Report ENQUAD 98-04.

Kitaigorodskii, S., Donelan, M. A., Lumley, J., and Terry, E. (1983). Wave-turbulence interaction in the upper ocean. Part II: Statistical characteristics of wave and turbulent components of the random velocity field in the marine surface layer. *Journal of Physical Oceanography*, 13:1978–1999.

Lambrakos, K. F. (1982). Seabed wave boundary layer measurements and analysis. *Journal of Geophysical Research*, 87:4171–4189.

Li, C., Blanton, J., and Chen, C. (2003). Mapping of tide and tidal flow fields along a tidal channel with vessel-based observation. *Journal of Geophysical Research*, 109:C04002.

Li, C. and O'Donnel, J. (1997). Tidally driven residual circulation in shallow estuarines with lateral depth variation. *Journal of Geophysical Research*, 102:27915–27929.

Li, C. and Valle-Levinson, A. (1998). Separating baroclinic flow from tidally induced flow in estuaries. *Journal of Geophysical Research*, 103:10405–10417.

Li, C., Valle-Levinson, A., Atkinson, L. P., and Royer, T. C. (2000). Inference of tidal elevation in shallow water using a vessel-towed acoustic Doppler current profiler. *Journal of Geophysical Research*, 105:26225–26236.

Lu, Y. and Lueck, R. G. (1999a). Using a broad band ADCP in a tidal channel. Part I: Mean flow and shear. *Journal of Atmospheric and Oceanic Technology*, 16:1556–1567.

Lu, Y. and Lueck, R. G. (1999b). Using a broad band ADCP in a tidal channel. Part II: Turbulence. *Journal of Atmospheric and Oceanic Technology*, 16:1568–1579.

Lu, Y., Lueck, R. G., and Huang, D. (2000). Turbulence characteristics in a tidal channel. *Journal of Physical Oceanography*, 30:855–867.

Lueck, R., Wolk, F., and Yamazaki, H. (2002). Oceanic velocity microstructure measurements in the 20^{th} century. *Journal of Oceanography*, 58:153–174.

Lueck, R. G., Huang, D., Newman, D., and Box, J. (1997). Turbulence measurement with a moored instrument. *Journal of Atmospheric and Oceanic Technology*, 14:143–151.

Massel, S. R. (1996). *Ocean Surface Waves: Their Physics and Prediction*. World Scientific Pub. Co.

Mathisen, P. P. and Madsen, O. S. (1996a). Waves and currents over a fixed ripple bed: 1. Bottom roughness experienced by waves in the presence and absence of currents. *Journal of Geophysical Research*, 101:16533–16542.

Mathisen, P. P. and Madsen, O. S. (1996b). Waves and currents over a fixed ripple bed: 2. Bottom and apparent roughness experienced by currents in the presence of waves. *Journal of Geophysical Research*, 101:16543–16550.

Mellor, G. L. (1975). A comparative study of curved flow and density-stratified flow. *Journal of the Atmospheric Sciences*, 32:1278–1282.

Mellor, G. L. (2002). Oscillatory bottom boundary layer. *Journal of Physical Oceanography*, 32:3075–3088.

Miles, J. W. (1961). On the stability of heterogeneous shear flows. *Journal of Fluid Mechanics*, 10:496–508.

Miles, J. W. (1963). On the stability of heterogeneous shear flows. Part 2. *Journal of Fluid Mechanics*, 16:209–227.

Miles, J. W. and Howard, L. N. (1964). Note on a heterogeneous shear flow. *Journal of Fluid Mechanics*, 20:311–313.

Militello, A. and Kraus, N. (2001). Shinnecock Inlet, New York, site investigation report 4: Evaluation of flood and ebb shoal sediment source alternatives for the west of Shinnecock interim project, New York. Technical report, ERDC/CHL TR-98-32, U.S. Army Engineer Research and Development Center,Vickburg, MS.

Moum, J. N., Caldwell, D., Nash, J., and G.D.Gunderson (2002). Observations of boundary mixing over the continental slope. *Journal of Physical Oceanography*, 32:2113–2130.

Nihoul, J. C. J. (1977). *Bottom Turbulence.* Elsevier Scientific Publishing Company.

Nunes-Vaz, R. A., Lennon, G. W., and de Silva Samarasinghe, J. R. (1989). The negative role of turbulence in estuarine mass transport. *Estuarine, Coastal and Shelf Science*, 28:361–377.

Nygaard, E. and Eik, K. J. (2004). Application of STWAVE in Norwegian coastal water. In *Proceedings, 8th International Workshop on Wave Hindcasting and Forecasting.*

Officer, C. B. (1980). *Box models revisited. In P. Hamilton and K.B. McDonald (Eds.), Estuarine ans Wetland Processes with Emphasis Modeling.* Plenum, New York.

Osborn, T. (1996). The role of turbulent diffusion for copepods with feeding currents. *Journal of Plankton Research*, 18:185–195.

Pawlowicz, R., Beardsley, B., and Lentz, S. (2002). Classical tidal harmonic analysis including error estimates in MATLAB using T_TIDE. *Computers and Geosciences*, 28:929–937.

Perlin, A. and Kit, E. (2002). Apparent roughness in wave-current flow: Implication for coastal studies. *Journal of Hydraulic Engineering*, 128 (8):729–741.

Peters, H. (1997). Observations of stratified turbulent mixing in an estuary. Neap to spring variations during high river run-off. *Estuarine, Coastal and Shelf Science*, 45:69–88.

Peters, H. (1999). Spatial and temporal variability of turbulent mixing in an estuary. *Journal of Marine Research*, 57:805–845.

Peters, H. and Bokhorst, R. (2000). Microstructure observations of turbulent mixing in a partially mixed estuary. Part I: Dissipation rate. *Journal of Physical Oceanography*, 30:1232–1244.

Peters, H. and Bokhorst, R. (2001). Microstructure observations of turbulent mixing in a partially mixed estuary. Part II: Salt flux and stress. *Journal of Physical Oceanography*, 31:1105–1119.

Press, W. H., Teukolsky, S. A., Vetterling, W. T., and Flannery, B. P. (1992). *Numerical Recipes (2nd ed.)*. Cambridge University Press, Cambridge.

Pritchard, D. W. (1952). Salinity distribution and circulation in the Chesapeake estuarine system. *Journal of Marine Research*, 11:106–123.

Pritchard, D. W. (1956). The dynamic stucture of a coastal plain estuary. *Journal of Marine Research*, 15:33–42.

Pritchard, D. W. (1967). Observations of circulation in coastal plain estuaries. *Estuaries*, 83:37–44.

Redfield, A. C. (1958). The influence of the continental shelf on the tides of the Atlantic coast of the United States. *Journal of Marine Research*, 17:432–447.

Rippeth, T. P., Fisher, N. R., and Simpson, H. (2001). The cycle of turbulent dissipation in the presence of tidal straining. *Journal of Physical Oceanography*, 31:2458–2471.

Rippeth, T. P., Simpson, J. H., Williams, E., and Inall, M. E. (2003). Measurement of the rate of production and dissipation of turbulent kinetic energy in an energetic tidal flow: Red Wharf Bay revisited. *Journal of Physical Oceanography*, 33:1889–1901.

Roplelewski, C. F. and Halpert, M. S. (1986). North American precipitation and temperture patterns associated with the El Niño/Southern Oscillation (ENSO). *Monthly Weather Review*, 114:2352–2362.

Rothschild, B. J. and Osborn, T. R. (1988). Small-scale turbulence and plankton contact rate. *Journal of Plankton Research*, 10:465–474.

Salmon, R. (1998). *Lectures on Geophysical Fluid Dynamics*. Oxford University Press.

Sanford, T. B. and Lien, R.-C. (1999). Turbulent properties in a homogeneous tidal bottom boudary layer. *Journal of Geophysical Research*, 104:1245–1257.

Schwing, F. B., Blanton, J. O., Knight, L. H., and Baker, C. V. (1985a). Ocean circulation and meteorology off the Georgia coast. Technical report, Technical Report 85-4 Skidaway Institute of Oceanography, Savannah, Georgia, U.S.A.

Schwing, F. B., Blanton, J. O., and Oey, L. Y. (1985b). Frictional response of continental shelf water to local wind forcing. *Journal of Physical Oceanography*, 15:1733–1746.

Schwing, F. B., Kjerfve, B., and Sneed, J. E. (1983). Nearshore coastal current on the South Carolina continental shelf. *Journal of Geophysical Research*, 88:4719–4729.

Seim, H. E., Blanton, J. O., and Gross, T. (2002). Direct stress measurement in a shallow, sinuous estuary. *Continental Shelf Research*, 22:1565–1578.

Seuront, L., Schmitt, F., and Lagadeuc, Y. (2001). Turbulence intermittency, small-scale phytoplankton patchiness and encounter rates in plankton: where do we go from here? *Deep-Sea Research*, 48:1199–1215.

Seymour, R. J. (1989). *Nearshore Sediment Transport*. Plenum Press, New York and London.

Shaw, W. J. and Trowbridge, J. H. (2001). The direct estimation of near-bottom turbulence fluxes in the presence of energetic wave motions. *Journal of Atmospheric and Oceanic Technology*, 18:1540–1557.

Shaw, W. J., Trowbridge, J. H., and Williams III, A. J. (2001). Budgets of turbulent kinetic energy and scalar variance in the continental shelf bottom boundary layer. *Journal of Geophysical Research*, 106:9551–9564.

Signell, R. P. and List, J. (1997). Effect of wave-enhance bottom friction on storm-driven circulation in Massachusetts Bay. *Journal of Waterway, Port, Coastal and Ocean Engineering*, 123:233–239.

Simpson, J. H. (1997). Physical processes in the ROFI regime. *Journal of Marine Systems*, 12:3–15.

Simpson, J. H., Brown, J., Matthews, J., and Allen, G. (1990). Tidal straining, density currents, and stiring in the control of estuarine stratification. *Estuaries*, 13:125–132.

Simpson, J. H., Burchard, H., Fisher, N. R., and Rippeth, T. P. (2002). The semi-diurnal cycle of dissipation in a ROFI: model-measurement comparisons. *Continental Shelf Research*, 22:1615–1628.

Simpson, J. H., Williams, E., Brasseur, L., and Brubaker, J. (2005). The impact of tidal straining on the cycle of turbulence in a partially stratified estuary. *Continental Shelf Research*, 25:51–64.

Smith, J. M. (1999). Wave breaking on an opposing current. Technical report, Coastal Engineering Technical Report CETN IV-7-01-1, U.S. Army Engineer Research and Development Center,Vickburg, MS.

Smith, J. M. and Gravens, M. B. (2002). Incident boundary conditions for wave transformation. In *Proceedings, 7^{th} International Workshop on Wave Hindcasting and Forecasting*, pages 373–383. October 21-25, 2002, Banff, Alberta, Canada.

Smith, J. M. and Resio, D. T. (2004). Improved shallow-water wave modeling. In *Proceedings, 8th International Workshop on Wave Hindcasting and Forecasting*. Nov 14-19, 2004, North Shore, Oahu, Hawaii.

Smith, J. M., Sherlock, A. R., and Resio, D. T. (2001). STWAVE- steady-state spectral wave model user's manual for STWAVE, version 3.0. Technical report, Technical Report

ERDC/CHL SR-01-1, U.S. Army Engineer Research and Development Center,Vickburg, MS.

Smith, J. M. and Smith, S. J. (2002). Grid nesting with STWAVE. Technical report, ERDC/CHL CHETN I-66, U.S. Army Engineer Research and Development Center,Vickburg, MS.

Smith, S. J. and Smith, J. M. (2001). Numerical modeling of waves at Ponce de Leon Inlet, Florida. *Journal of Waterway, Port, Coastal and Ocean Engineering*, 127:176–185.

Stacey, M. T. (1999). Observations of turbulence in a partially stratified estuary. *Journal of Physical Oceanography*, 29:1950–1970.

Stacey, M. T., Burau, J. R., and Monismith, S. G. (2001). Creation of residual flows in a partially stratified estuary. *Journal of Geophysical Research*, 106:17013–17037.

Stacey, M. T., Monismith, S. G., and Burau, J. R. (1999). Measurements of Reynolds stress profiles in unstratified tidal flow. *Journal of Geophysical Research*, 104:10933–110949.

Styles, R. and Glenn, S. (2002a). An optimized combined wave and current algorithm for arbitrary bed roughness. Technical report, Coastal Phys. Oceanogr. Lab, Dep. of Geol. Sci., Univ. of S.C., Columbia.

Styles, R. and Glenn, S. M. (2002b). Modeling bottom roughness in the presence of wave-generated ripples. *Journal of Geophysical Research*, 107:1950–1970.

Suhayda, J. N. and Pettigrew, N. R. (1977). Observations of wave height and wave celerity in the surf zone. *Journal of Geophysical Research*, 82:1419–1424.

Tennekes, H. and Lumley, J. (1999). *A First Course in Turbulence*. MIT Press.

Terray, E., Gordon, R. L., and Brumley, B. (1997). Measuring waves height and direction using upward-looking ADCPs. In *Proc. Oceans 97, IEEE, New York*. 287-290.

Thornton, E. B. (1979). Energetics of breaking waves within the surf zone. *Journal of Geophysical Research*, 84:4931–4938.

Thornton, E. B. and Guza, R. T. (1982). Energy saturation and phase speeds measured on a natural beach. *Journal of Geophysical Research*, 87:9499–9508.

Thornton, E. B. and Guza, R. T. (1983). Transformation of wave height distribution. *Journal of Geophysical Research*, 88:5925–5938.

Trowbridge, J. (1997). On a technique for measurement of turbulent shear stress in the presence of surface waves. *Journal of Atmospheric and Oceanic Technology*, 15:290–298.

Trowbridge, J. and Elgar, S. (2001). Turbulent measuremts in the surf zone. *Journal of Physical Oceanography*, 31:2403–2417.

Trowbridge, J., Geyer, W. R., Bowen, N. M., and Williams III, A. J. (1999). Near bottom turbulence measurement in a partially mixed estuary: Turbulent energy balance, velocity structure, and along-channel momentum balance. *Journal of Physical Oceanography*, 29:3056.

Trowbridge, J. and Madsen, O. S. (1984a). Turbulent wave boundary layer. 1. Model formulation and first-order solution. *Journal of Geophysical Research*, 89:7989–7997.

Trowbridge, J. and Madsen, O. S. (1984b). Turbulent wave boundary layer. 2. Second-order theory and mass transport. *Journal of Geophysical Research*, 89:7999–8007.

Valle-Levinson, A., Reyes, C., and Sanay, R. (2003). Effects of bathymetry, friction, and rotation on estuary-ocean exchange. *Journal of Physical Oceanography*, 33:2375–2393.

Voulgaris, G. and Trowbridge, J. H. (1997). Evaluation of the acoustic Doppler Velocimeter (ADV) for turbulence measurement. *Journal of Atmospheric and Oceanic Technology*, 15:272–289.

Wahl, T. L. (2000). Analyzing ADV Data Using WinADV. 2000 Joint Conference on Water Resources Engineering and Water Resources Planning & Management July30- Aug 2, 2000.

Weber, A. H. and Blanton, J. (1980). Monthly mean wind fields for the South Atlantic Bight. *Journal of Physical Oceanography*, 10:1256–1263.

Wiberg, P. and Smith, J. (1982). A comparison of field data and theoretical model for wave-current interactions at the bed on the continental shelf. *Continental Shelf Research*, 2:147–162.

Wolf, J. (1999). The estimation of shear stresses from near-bed turbulent velocities for combined wave-current flows. *Coastal Engineering*, 37:529–543.

Wong, K.-C. (1994). On the nature of transverse variability in a coastal plain estuary. *Journal of Geophysical Research*, 99:14209–14222.